Evolution of cold gas in active galaxies

Brenda Namumba

April 2015

A project submitted in fulfillment of the requirements for the degree M.Sc.
in the School of Chemistry and Physics
University of KwaZulu-Natal

Supervisors: Dr C.Zunckel and Dr N.Gupta

Abstract

Atomic hydrogen, hereafter referred to as HI, plays a crucial role in the evolution of galaxies and their central super-massive black-holes, fueling the formation of stars and feeding of active galactic nuclei (AGN). By observing HI in host galaxies of compact radio sources, which are believed to be young ($< 10^{4-5}$ years), we can study the early stages of the evolution of active galaxies. In the local Universe, this can be done through HI 21-cm emission observations. Unfortunately, the weakness of HI 21-cm emission line transition means that extremely large telescopes are needed to carry out such studies at even moderate redshifts (z>0.1). HI 21-cm absorption line provides an alternative means to studying the physical conditions of the neutral gas in distant galaxies at high redshifts.

The objective of this thesis is two fold: (1) to study cold atomic gas in radio sources via the 21-cm absorption line and (2) to test the observing mode and performance of Karoo Array Telescope (KAT-7), the engineering testbed for MeerKAT. In this study, we have observed 4 compact radio sources from the literature that have detected 21-cm absorption. In one case, the results from KAT-7 data are used to derive column density and kinematics of the HI gas. For the other three cases, we do not detect the 21-cm line either due to strong radio frequency interference (RFI) or low signal-to-noise ratio. We present the sensitivity and spectral dynamic ranges achieved in these observations and discuss various data analysis related issues that influence the detectability of 21-cm absorption line. The information gathered from this study will allow us to carry out a systematic larger survey of 21-cm absorption line in AGN using KAT-7 in the near future.

Acknowledgements

I would like to express my gratitude to my supervisors Dr.C. Zunckel and Dr.N. Gupta. I would like to thank them for the useful comments, remarks and engagement throughout the learning process of my masters thesis.
My sincere gratitude goes to Dr.S. Geodhart for her invaluable contributions towards my thesis; in helping me with the data observations and in assisting me understand the operations of the KAT-7 telescope, as well as her encouragements and insightful comments towards improving this work.
To Prof.C. Carignan, Dr.S. Passmoor and Dr.D. Lucero, I express my heartfelt gratitude for their insights throughout the process of doing this project as well as writing of the thesis.
I must withal acknowledge the external examiners for their remarks after my first submission. I am certain that the quality of this work was greatly enhanced due to their vital inputs and remarks. I genuinely say thank you to them for their comments.
A special thanks goes to the SKA, SA staff at the KAT-7 office for their joint effort at whatever point I needed their assistance and for permitting me to utilize the equipments during the data reduction and analysis.
I would also like to thank my family. Words cannot express how grateful I am to my mother, father, brothers and sisters for all the sacrifices that you made on my behalf. Your prayers for me were what sustained me this far. I would also like to thank all my friends who supported me in writing and editing my work and encouraged me to strive towards my goal.
I likewise express my gratitude to the University of KwaZulu-Natal, Westville Campus, the Inter-University Centre for Astronomy and Astrophysics (IUCCA), and the National Astrophysics and Space Science Program (NASSP) for their academic support during my masters.
In conclusion, I recognize that this research would not have been possible without the financial assistance from the Square Kilometer Array (SKA).

Plagiarism Declaration

I, Brenda Namumba, know the meaning of plagiarism and declare that all of the work in the document, save for that which is properly acknowledged, is my own.

Contents

List of Figures

List of Tables

Chapter 1

Introduction

The HI 21-cm line has proven to be a powerful tool for tracing neutral HI in galaxies, providing important information on the temperature, distribution, and kinematics of the gas. In this thesis, we present test observations carried out with KAT-7 array to study the HI 21-cm absorption line in four radio sources at low redshifts.

1.1 Thesis Motivation

The HI 21-cm line, observed as absorption against a background radio source, can provide important information on the kinematics, distribution, and temperature of line of sight cold gas. Currently, such studies are hindered by a number of technical factors such as sparse redshift coverage, limited bandwidth/resolution, hostile radio frequency interference (RFI) environment, and limited collecting area etc. In the lead up to the Square Kilometer Array (SKA) project, several next generation radio telescopes are being built around the world. These instruments are equipped with large instantaneous bandwidths and being set-up in RFI free sites in the Republic of South Africa and Australia.

In readiness for the SKA precursor telescope MeerKAT, South Africa has built a seven element engineering test-bed called the Karoo Array Telescope (KAT-7), which started commissioning in December 2010. The KAT-7 is equipped with relatively wide bandwidth and covers a frequency range 1200-1959 MHz. In this thesis, we present the test observations we have carried out to characterize the spectral line capabilities of KAT-7 that are relevant for 21-cm absorption line observations. These observations will allow us to plan and carry out a systematic survey of 21-cm absorption such as the MeerKAT Absorption Line Survey (MALS). MALS is a spectral line survey to be carried out on MeerKAT covering a frequency range 0.58-1.75 GHz. Due to the sensitivity and wide frequency coverage of MeerKAT, this survey is expected to detect both weak and distant HI absorbers. This thesis mainly focuses on three significant objectives which are explained below.

Cold atomic gas in radio sources: Cold neutral gas ultimately provides the fuel for star formation in galaxies and also plays an important role in fueling the most powerful radio sources seen in the universe. The feedback from these radio sources affects their environment and that of host galaxies. In this thesis, we attempt to verify the presence of neutral hydrogen associated with these sources via the 21 cm absorption line using observations taken with KAT-7. For the one detected absorption line, we derive the properties of the associated radio galaxy such as optical depth, line width, and HI column density. These values are later compared with the available literature.

KAT-7 HI observing mode and telescope performance: KAT-7 is in its early stages of operation. It is essential to understand its operation and performance, as these will allow us to identify and fix any observable malfunctions and also aid in the development of software for MeerKAT data analysis. In this thesis, we focus on studying the HI observing mode and the performance of KAT-7 with regards to HI 21-cm absorption line studies. The velocity coverage and resolution provided by this mode are ideal for 21-cm absorption line search. To study the telescope performance, we selected two compact sources for the sample used in this thesis. Compact sources are ideal for studying the telescope performance because of their known visibilities (constant amplitude and zero phase). We deduce the spectral dynamic range and mean root square (rms) noise from the final images. These parameters are important in determining the weakest absorption features that can be detected with the KAT-7. We also look at possible factors that can influence the rms noise achieved for an observation. These values will help in planning for future absorption line studies to be carried out on KAT-7.

Radio interferometry data reduction: Understanding radio interferometric data and calibration process is essential in acquiring good quality scientific results. New software such as the Common Astronomical Software Applications (CASA) are being developed with the main goal of supporting the data post-processing needs of new and upcoming radio astronomical telescopes such as MeerKAT. CASA is a data reduction software that is under development by a consortium of scientists at National Radio Astronomical Observatory (NRAO), the European Southern Observatory (ESO), the National Astronomical Observatory of Japan (NAOJ), the CSIRO Australian Telescope National Facility (CSIRO/ATNF), and the Netherlands Institute for Radio Astronomy (ASTRON) under the guidance of NRAO. CASA is specially designed to support large volumes of data from next generation telescopes. In this thesis, we present detailed analysis of a sample of 4 radio sources observed with KAT-7 using CASA.

1.2 Background

1.2.1 Active Galactic Nuclei

The term *Active Galactic Nuclei* (AGN), refers to the existence of energetic phenomena in the central regions of galaxies that can not be attributed clearly and directly to stars (Tadhunter 2008). AGN are the most luminous persistent sources of electromagnetic radiation (from radio to gamma rays) in the universe, reaching bolometric luminosities of $10^{40} - 10^{48}$ erg s^{-1}. For a long time it has been argued that AGN are powered by the accretion of matter onto a supermassive black hole (SMBH) (with masses between $\sim 10^6 - 10^{10} M_\odot$) (Rees 1984). Because AGN are so luminous, they can be observed out to very high redshifts ($z > 6$) (De Robertis 1999). This makes them excellent probes of the early Universe, and should further our understanding of the evolution of the Universe as a whole. The intergalactic medium can also be well studied by looking at the absorption lines in the spectra of distance quasars.
There is no single observational signature of an AGN. The list below covers some of the historically important basic properties that have allowed systems to be identified as AGN.

- The nuclear luminosity is greater than that of its host galaxy (L_{bol} reaching up to 10^{48} erg s^{-1}).

- Broad band emission from the radio to the gamma ray wavelengths.

- Powerful radio emission ($P_{5\,GHz} > 10^{25}$ WHz^{-1} sr^{-1}) for about 10% of the AGN.

- Strong emission lines in the optical, ultraviolet, and X-rays.

- Fast variability that entails compactness (with radius, $R \sim 10^{12} - 10^{18}$ cm).

The modern picture of an AGN (see Figure 1.1) can be summarized as follows. The central engine is the SMBH of size ($>10^5 M_\odot$) (Weaver 2000), residing at the center of the host galaxy. The SMBH is actively accreting material ranging from a small fraction of a solar mass ($M_\odot$) to several $M_\odot$ per year. The accreted material has formed an accretion disk which gives off continuum emission in the optical to ultraviolet (UV) part of the spectrum. Next we have the Broad line regions (BLR) which consist of photo-ionized materials located within the nucleus of active galaxies, with a typical spatial extent of 10-100 light days (Zhang and Wang 2006). These clouds of ionized gas swirl around the SMBH with velocities ($>$ 2000 km hr^{-1}), giving rise to broad emission lines seen in optical and UV spectra. BLR are seen to be very dense ($N_e \sim 10^9 - 10^{11}$ cm^{-3}). Further from the nucleus are slower-moving, ionized materials that display spatial extents of a few to $\sim$ 100 pc. These regions are known as Narrow line regions (NRL). The density of material within these regions is significantly lower than in BLRs ($N_e \sim 10^3 - 10^6$ cm^{-3}) (De Robertis 1999), and hence allows for emission

of forbidden optical lines. The widths of these lines infer velocities of a few to $\sim$ 100 km s^{-1} (Zhang and Wang 2006). The presence of a neutral absorbing, molecular torus (MT), perhaps formed into a toroidal shape, coincident with the plane of the accretion disk, has been inferred in observations of some objects (De Robertis 1999). The molecular torus helps to explain the varied optical appearance of AGN. The absorbing material will block the broad-line emission coming from the SMBH for sources seen with disk edge on, but not for those oriented with the disk in the plane of the sky, where we can see down into the immediate black hole enviroment (Zhang and Wang 2006). Lastly, in a small fraction of AGN we also observe radio jets that can extend to Mega-parsec scales (Mpc). Synchrotron radio emission from these jets arises from electrons going around the magnetic fields causing the radio emission from these jets(Netzer 2013). Figure 1.1 shows the main components of an AGN in the current paradigm.

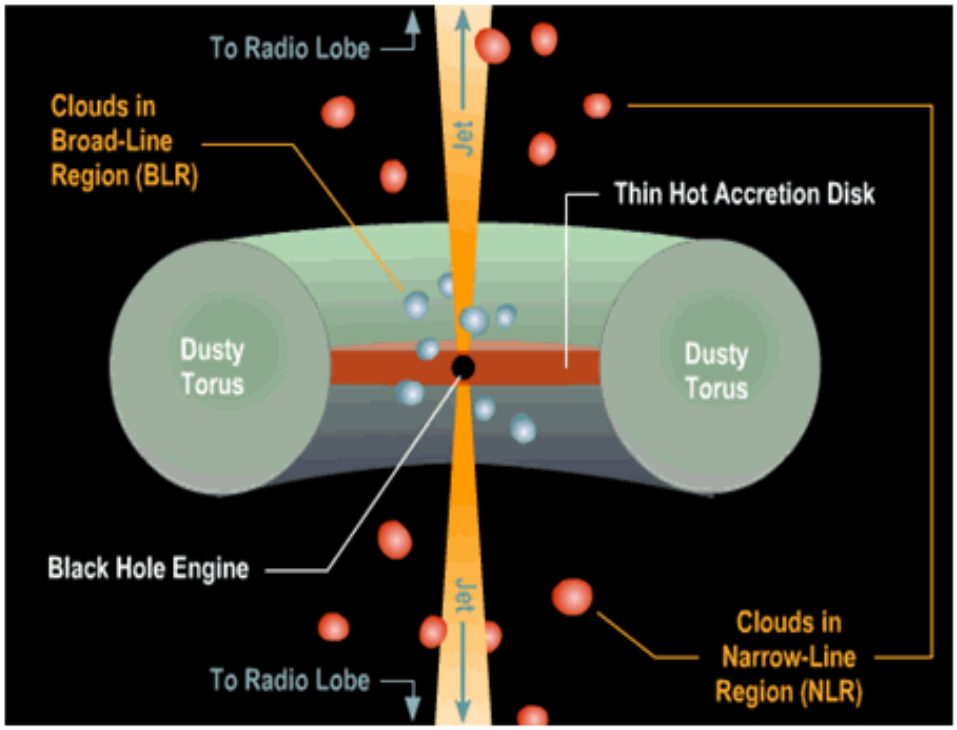

Figure 1.1: Showing the main parts of an AGN [1]

1.2.2 The black hole paradigm for AGN

The fundamental question about AGN are how the energy that is detected as radiation is generated. Essentially the problem is that an AGN produces as much light as up to several trillion stars in a volume significantly smaller than a cubic parsec (De Robertis 1999). A convincing case for a SMBH engine being the source of energy generated in AGN was built

[1] http://astronomyonline.org/Cosmology/Galaxies.asp

from circumstantial and a few particularly convincing pieces of evidence beginning with the work of Salpeter (1964). Salpeter (1964) used information on these exotic sources to elaborate the so-called *SMBH paradigm*. According to this paradigm, the central engine of every AGN is a SMBH accreting matter through an accretion disk around the compact source. The fundamental process in producing the luminosity is via gravitational potential energy (E_g) of an accreting mass m:

$$E_g = G\frac{M_{BH}m}{R_{BH}}, \tag{1.1}$$

where M_{BH} is the mass of the central black hole, G is the gravitational constant, and R_{BH} is the radius of the black hole. From Equation 1.1 it is clear that the large mass and small radius typical of SMBH will release a great deal of energy than accretion onto a less compact object. In reality calculating the efficiency ϵ of the accretion depends on the properties of the black hole and requires a general relativistic treatment. In this case, the energy emission rate (that is, the luminosity) is given by

$$L = dE/dt = \epsilon\dot{M}c^2 \text{ with } \dot{M} = \frac{d}{dt}M_{BH} \tag{1.2}$$

where c is the speed of light, $\dot{M}$ is the accretion rate, and the efficiency (ϵ) of 1 implies all available gravitational potential energy is radiated. The rate of accretion onto the SMBH is one of the likely fundamental parameters of importance in understanding AGN phenomena. A very important scale is set by considering the accretion rate at which the radiation pressure from accreting material balances the gravitational pull on the material. This is called the Eddington limit, and is usually derived under the assumption of a spherically symmetric, steady flow. Further, it is assumed that all inflowing material is ionized hydrogen. The derivation of the limit follows directly from balancing the two opposite forces:

$$L_{Edd} = 1.3 \times 10^{38}(M/\dot{M})ergs^{-1} \tag{1.3}$$

Thus, the Eddington luminosity is dependent only on the SMBH mass. Such enormous powers prompts us to consider highly efficient mechanism of energy production. The most efficient mechanism known is matter-antimatter annihilation but it is not believed that large quantities of anti-matter are present in the universe. The next most efficient mechanism is accretion onto relativistic objects such as neutron stars and black holes. Neutron stars have a maximum mass of $\sim 2M_{\odot}$, so accretion onto neutron stars cannot be the central power in AGN. We are thus led to consider massive black holes (De Robertis 1999).

1.2.3 Taxonomy of AGN

AGN are classified depending on their observation properties. Over the last decades, AGN classification has improved as better telescopes with better resolution have become available. AGN taxonomy, as shown in Figure 1.2, is mainly based on the ratio of radio to optical

emission, defining radio-loudness parameter as $R_L = log(F_{5GHz}/F_B)$. If $R_L \geqslant 10$ the object is classified as radio-loud, otherwise radio-quiet. Figure 1.2 shows the summary of the taxonomy of AGN. Here F_{5GHz} and F_B stands for the flux at some specified radio, $5GHz$, and optical, B, frequencies.

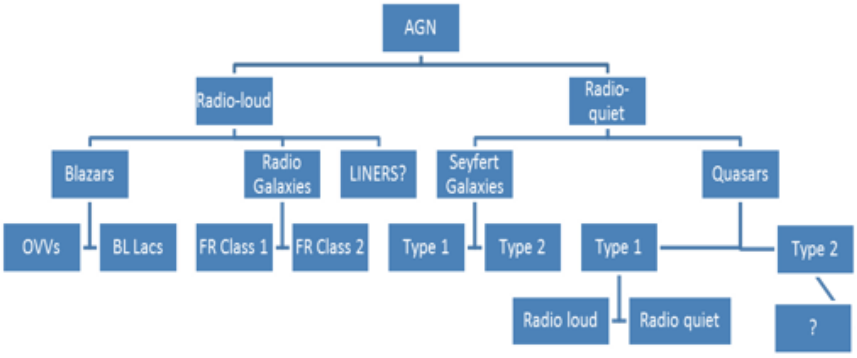

Figure 1.2: Summary of Taxonomy of AGN [2]

- **Radio Quiet AGN**: The first class of radio quiet AGN are classified as faint objects with the absolute magnitude of $M_V > -23$ in the V band and are hosted in early-type spiral galaxies (Osterbrock et al. 1992). These sources are referred to as Seyfert galaxies. Seyferts are further divided based on the relative strength of their optical-ultraviolet narrow and broad emission lines into Type 1 and Type 2. If the optical-ultraviolet spectrum shows only narrow lines, either permitted or forbidden, the AGN are classified as Type 2; instead, if either narrow and broad lines are present, the AGN are classified as Type 1(Osterbrock et al. 1992). An intermediate classification can be considered based on the relative strength of the two sets are now in common usage (Seyfert 1.9 and 1.8)(Osterbrock 1981). Seyfert 2s, which are typically fainter than Seyfert 1s, are those seen with the torus edge-on, so that the obscuring torus blocks the emission from the ionized region close to the SMBH, but not the narrow line emission produced much further out, above and below the torus. Seyfert 1s, on the other hand, are oriented such that we can see unobscured down to the broad line region. The original definition of the class Seyfert was primarily morphological; Seyfert were galaxies with high surface brightness nuclei, and subsequently spectroscopy revealed unusual emission line characteristics. When observed with a large optical telescope, Seyfert galaxies usually look like a normal distant spiral galaxy with a star at the center as shown in Figure 1.3. The modern definition has evolved so that Seyfert galaxies are now associated with the presence of strong, high ionization emission lines, though spectroscopic studies indicate that

[2] https://www.cta-observatory.ac.uk/?page_id = 1194

these nearly always occur in spiral galaxies .

The second type of radio quiet AGN are the radio quiet quasars. Originally quasars

Figure 1.3: The image above shows the Seyfert galaxy NGC 7742. This face-on Seyfert has an unusually bright yellow core relative to its delicate blue spiral arms [3].

were defined by their radio loudness. However, the definition has broadened to cover any very bright AGN of small angular size in the optical. It turns out that 90% of these are radio quiet. Quasars do not have relativistic jets (Shields 1999). In a sense, Seyferts have lower-luminosity quasars in their nuclei. The brightest quasar have spectra dominated by broad emission lines, and as with the Seyferts, these are called type 1(unobscured). However, narrow line quasars also do exist; these are called type 2 (obscured) and are probably seen at a larger inclination to the disk (Shields 1999).

- **Radio loud AGN**: Radio loud AGN can be classified on the basis of their structural and spectral properties at radio wavebands. These sources are known to have relativistic jets pointing very close to our line of sight. Fanaroff and Riley (1974) first noticed that radio luminosity correlated with which part of the jet had vast highest surface brightness, and devised a classification scheme which divides the vast majority of radio galaxies into two classes (FR I and II). The classification of these sources is assumed according to the ratio R, the distance between the two brightest spots, to the total extent of the radio image. Nearly all FR Is indicate $R < 0.5$ while FR IIs are seen to have ($R > 0.5$)(Fanaroff and

[3] http://oneminuteastronomer.com/3626/seyfert-galaxies/

Riley 1974). FR Is are seen to have low luminosity and tend to have jets which are easily visible down to the core, and brightest at the center. FR IIs tend to have highly collimated, often invisible jets which terminate in hot spots and bright lobes as shown in Figure 1.4. In addition to the radio morphological types, FR II radio galaxies are traditionally divided into broad line radio galaxies (BLRGs) and narrow line radio galaxies (NLRG), analogous to the distinction between type 1 and 2 radio quiet AGN, and understood to be the result of orientation differences through the BLR obscuring molecular torus. Broad line objects are more likely to show one sided jets, which fits with the orientation model. However, FR I radio galaxies do not exhibit broad lines, and tend to have weak emission lines overall. Obscuration is generally not seen, or is much less than in FR II radio galaxies.

Another striking class of radio loud AGN are that of compact steep spectrum (CSS)

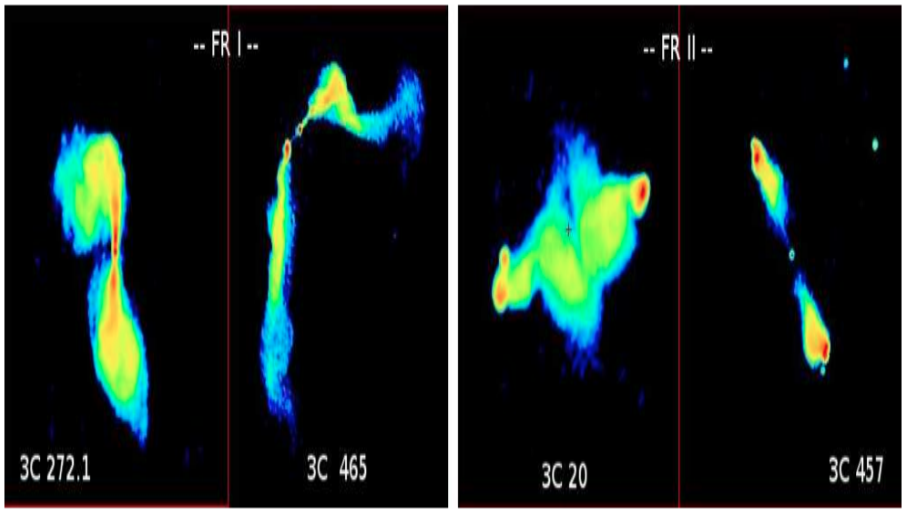

Figure 1.4: Showing the morphological differences between FR I and FR II galaxies [4]

and gigahertz peaked spectrum (GPS) sources. CSSs are defined to be radio sources with projected linear size $\lesssim$ 15 kpc and having a steep high frequency radio spectrum ($\alpha \gtrsim 0.5$, where $S_\nu \propto \nu^\alpha$) (Krawczynski and Treister 2013). GPS on the other hand are classified on the basis of their convex radio spectra peaking at $\sim$ 1 GHz. The most remarkable feature of CSS and GPS sources is their compactness due to the projection effects (Krawczynski and Treister 2013).

Seen at smaller angles to the jets axis than radio galaxies are steep-spectrum radio quasars and flat steep-spectrum sources. These sources are defined depending on their complex structure and low spectral indices ($\alpha \approx 0$), an indicative of self-absorption (Netzer 2013). These type of sources are effectively distinguished by the sample criteria $\alpha \geqslant 0.5$ known as steep-spectrum sources and $\alpha < 0.5$ for flat spectrum sources(Netzer 2013). Flat spectrum sources are usually associated with radio loud type 1 quasars while most steep spectrum sources are associated with galaxies or empty field if galaxies are too distant. We also

[4] http:www.jb.man.ac.uk/atlas/2013

find radio sources with very low spectral index (α <-1.4) (Netzer 2013). These sources are classified as ultra steep spectrum and are identified with a classical FR II radio type morphology.
Finally, blazars are perhaps the most rare and unique of all AGN. A single class of blazars could probably describe what had been several sub-types of radio loud quasars (e.g flat-spectrum sources, high polarization quasars and optically violent variable) as well as the optically featureless but radio core dominated BL Lacerate objects. In general, blazars are core-dominated, high luminous, variable, and show significant polarization in the X-ray. Blazars are subdivided based on the properties of their optical emission lines, being strong and quasar like in the flat spectrum radio quasar, and generally absent or very weak in BL Lacerate.

Unification of AGN

The properties of many of the observationally defined classes of AGN outlined above can be described in a simple manner by the so called 'unified scheme' of AGN. Unified models for AGN propose that different classes of AGN can be explained in terms of one object observed at different observing conditions (Urry and Padovani 1995). The currently favored unified models are 'orientation-based unified models'. This model propose that the difference between the different types of AGN raises due to their orientations with respect to the line of sight (Urry and Padovani 1995). Seyfert galaxies are united at low luminosities. Seyfert Is are thought to arise when the observer has a direct view of the active nucleus while in Seyfert IIs the nucleus is obscured which prevents the detection of broad lines (Wiita 2006). Quasars take up the place of Seyfert Is at high luminosities (Wiita 2006). For radio loud AGN, the unification between FR I and FR II is explained in terms of beaming angle. It has been suggested that when the radio luminosity is low, the opening angle of the obscuration may be so small that it is no wider than the beaming angle for its relativistic jet. Any unobscured view of an FR I nucleus would then show only as a BL Lac object (Wiita 2006). CSS and GPS have their size distribution and orientation properties consistent with the unification scheme for FR II radio sources (Saikia et al. 1995) and it is believed that in due course most of the CSS and GPS will evolve into large FR II sources. Figure 1.5 shows the unification scheme of AGN.

To conclude this section, the torus is the most important element of unification schemes as well as fueling of the AGN. Using absorption line studies can help us understand the distribution and kinematics of gas in and around the tori.

[5] https://www.cta-observatory.ac.uk/?page_id=1196

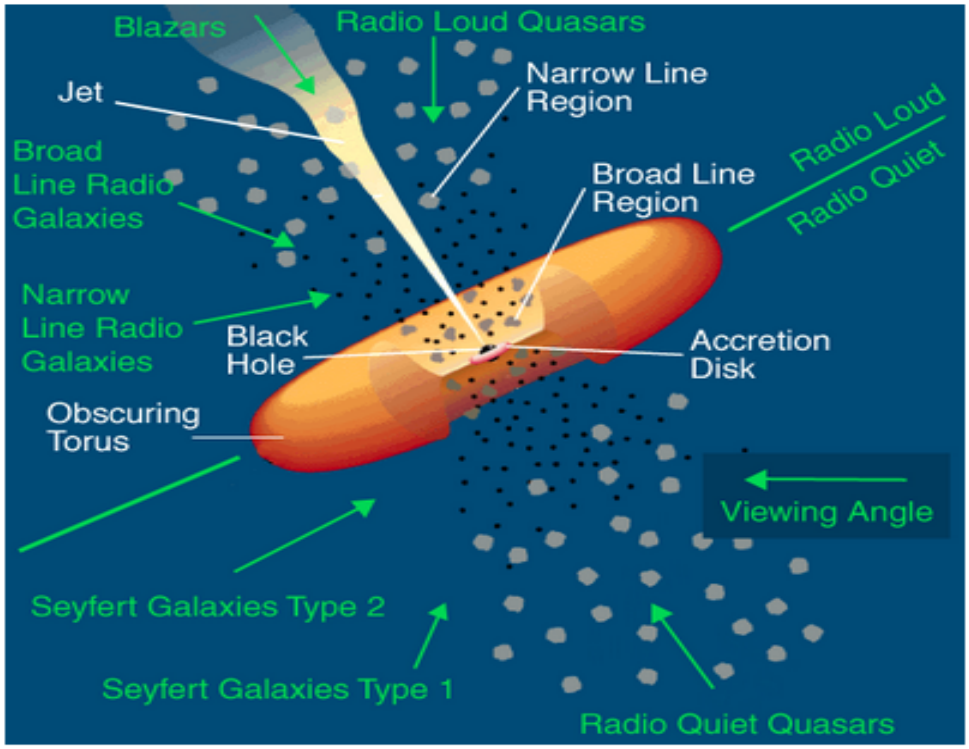

Figure 1.5: Schematic diagram showing the AGN unification scheme. The arrows in green represent the AGN type that is seen from a certain viewing angle [5]

1.2.4 HI 21 cm absorption as a probe of circumnuclear gas

The gas outflows associated with AGN provide energy feedback into the interstellar medium (ISM) that can profoundly affect the evolution of the central engine and the host galaxy (Emonts et al. 2010). Observations of HI gas associated with AGN can provide crucial information about the fueling of AGN and the evolution of the host galaxies. 21-cm absorption studies offer the unique possibility of tracing the kinematics and morphology of neutral gas in radio loud AGN environment, and determining the nature of the accretion or the energetic of the outflow. Circumnuclear tori and disk have often been proposed to produce the HI absorption observed in some radio galaxies (Morganti et al. 2003). The best cases for possible tori (size from pc to tens of Kpc) have been found in small objects CSS and GPS, where the background continuum is more favorable for detecting these structures (van Gorkom et al. 1989). In these sources the HI absorption detection rates has been reported to be as high as 45% with HI column density being anti-correlated with source size (Gupta et al. 2006).

The 21-cm absorption line allows us to measure the column density of the neutral hydrogen in an absorbing system, where the column density is the total amount of material per unit area. The width of the line discloses information about the temperature, global motion, and kinematics of the absorbing system (Wilson et al. 2013). The HI column density as defined

by the 21-cm absorption profile is given by

$$N_{HI} = 1.82 \times 10^{18} \frac{T_s}{f} \int \tau dv \ \mathrm{cm}^{-2} \tag{1.4}$$

where T_s is the spin temperature of the absorbing system (K) and f is the covering factor of the background continuum flux by the absorber, τ is the optical depth and dv is the velocity width of the line profile.

HI absorption line measurement can detect both the circumnuclear gas and large scale gas, including inflows and outflows related to AGN fueling and feedback. The HI absorption spectra exhibit a variety of line profiles, implying significant, sometimes complex gas motions. Previous observations of the 21-cm line associated with AGN exhibit spectral lines with both deep, narrow components $\approx$ 10kms^{-1} and broad wings with width $\approx$ 100kms^{-1} (Morganti et al. 2005). Morganti et al. (2005) detected broad HI components with absorption ranging between 600 kms^{-1} and 2000 kms^{-1}. These broad line profiles are associated with high velocity outflows, providing a probe of feedback between the central radio source and the star forming interstellar medium of its host galaxy. A fraction of HI absorbers tend to be either redshifted or blueshifted with respect to the systematic velocity by hundreds of kms^{-1}. Redshifted 21 cm absorption line is mainly associated to gas infalling towards the AGN while blueshifted absorption features are associated with gas interacting with the jets. van Gorkom et al. (1989) reported redshifted HI absorption spectra in 4 nearby compact radio galaxies with respect to the optical velocity while Gupta et al. (2006) detected blue shifted absorption features in compact radio sources in which 65% were GPS sources. Studies have also shown a complex situation were sources have substantial redshifted and blue shifted HI absorption lines (Vermeulen 2004), suggesting the atomic gas may be flowing out or flowing in, interacting with the jets or rotating around the nucleus.

Although there have been interesting results on the studies of the gas kinematics of nearby AGN in an effort to understand both the fueling of this activity and the relationship between the starburst and the AGN, the redshift coverage of the samples is sparse and mostly limited to z < 1. The next generation of HI 21-cm absorption studies aims at increasing the statistics of available HI absorbers, covering a redshift range of $z \gtrsim 6$ to the present epoch (Kanekar and Briggs 2004), looking at the neutral hydrogen content of fainter population of radio sources and looking for differences in the structure of their central regions and in how these sources are fueled. Such studies will be made possible with the expected high sensitivity and frequency coverage in which the SKA pathfinders and later the SKA are being built.

1.3 Radiative transfer equation

The theory of the radiative transfer provides the means of understanding the observed spectra of sources and also describing the effects of the medium through which the radiation passes on its final way to final detection. The radiative transfer equation describes the change in specific intensity for photons traveling a distance in a specific direction at a given

position. In this section, we describe the theory of 21 cm absorption line formation using the radiative transfer equation. For consistency in notation and easy flow of information, we summarize the most significant formula involved, following the notation used by Kulkarni and Heiles (1988). Detailed information and derivation of the radiative transfer can be obtained from books Wilson et al. (2013) and Rybicki and Lightman (1986).
As radiation passes through a medium, the intensity of the radiation is governed by the equation of radiative transfer,

$$\frac{dI_\nu}{d\tau_\nu} = -I_\nu + S_\nu \tag{1.5}$$

where I_ν is the specific intensity and τ_ν is the optical depth defined by:

$$\tau_\nu = \kappa_\nu ds, \tag{1.6}$$

where ds is the path length through the medium, and S_ν is the source function, defined as

$$S_\nu = \frac{j_\nu}{\kappa_\nu} \tag{1.7}$$

where j_ν is the emissivity of the medium and κ_ν the absorption coefficient at frequency ν. Integrating Equation 1.5 from 0 to τ_ν reduces to ;

$$I_\nu(\tau_\nu) = I_\nu(0)e^{-\tau_\nu} + \int_0^{\tau_\nu} e^{-(\tau_\nu - \tau_\nu')} S_\nu(\tau_\nu') d\tau_\nu', \tag{1.8}$$

which, for the case of a source function which is constant throughout the medium, reduces to

$$I_\nu(\tau_\nu) = I_\nu(0)e^{-\tau} + S_\nu(1 - e^{-\tau_\nu}) \tag{1.9}$$

In an equivalent way, one can define a brightness temperature T_B which corresponds to the temperature which a black body would have at frequency ν if it where to emit the specific intensity $I(\nu) = S(\nu)$, where, $I(\nu) = \frac{2\nu^2 k}{c^2} T_B$. This procedure is generally used in radio astronomy where the Rayleigh-Jeans approximation is valid.

$$\frac{dT_B}{d\tau(\nu)} = T_B - T \tag{1.10}$$

where T is the thermodynamic temperature of the medium. Equation 1.10 can be solved in the case of a homogenous isolated HI cloud embedded in a background radiation field with a brightness temperature of T_{bg}. Employing $e^{-\tau_\nu}$ as an integrating factor one finds the following important relation:

$$T_B(\nu) = T_{bg}(\nu)e^{-\tau(\nu)} + T(1 - e^{-\tau(\nu)}) \tag{1.11}$$

If we are dealing with an optically thick cloud, ($\tau(\nu) \gg 1$), the formula for the brightness temperature simply reduces to $T_B = T$ and $T_B = \tau(\nu)T$ if the cloud is optically thin ($\tau(\nu) \ll 1$).

HI 21-cm absorption line

The 21 cm line is the transition between the two hyperfine structure levels of neutral hydrogen (HI). The energy between the two levels differs slightly due to the interaction of the spin of the nucleus and that of the electron. The frequency of the resulting line has been measured ($t \sim 3.49 \times 10^{14}$)s. The level population in the HI hyperfine levels is given in terms of the Boltzmann factor, where in this case the the excitation temperature for HI is referred to as the spin temperature, T_s. In local thermodynamic equilibrium (LTE), the spin temperature is approximately the kinetic energy of the gas. They are exactly the same thing.

$$\frac{n_1}{n_0} = \frac{g_1}{g_0}\ exp(-\frac{h\nu}{kT_s}), \tag{1.12}$$

where n_1 and n_0 are the number densities of electrons in the upper and lower state of the hyperfine levels respectively and g_0 and g_1 are the statistical weights of the lower and upper spin states respectively. The energy $h\nu$ corresponds to the level separation at 21 cm wavelength defined as:

$$T^* = \frac{h\nu_{10}}{k} = 0.0682K, \tag{1.13}$$

In thermodynamic equilibrium, the transition rate per unit time per unit volume from level 0 to level 1 must equal the transition rate from level 1 to level 0. If the number density of atoms in level 0 is n_0, and that in level 1 is n_1, then using the Einstein coefficients we have;

$$n_1 B_{01} \bar{I} = n_2 A_{10} + n_2 B_{21} \bar{I} \tag{1.14}$$

where B_{01} is the coefficient of absorption, B_{10} is the coefficient of induced emissions and A_{10} is the coefficient of spontaneous emission. $\bar{I}$ represents the mean intensity. Rearranging Equation 1.14 gives;

$$\bar{I} = \frac{A_{10}/B_{10}}{(n_1/n_2)(B_{01}/B_{10}) - 1} \tag{1.15}$$

The Einstein coefficients must satisfy the following Einstein relation for $\bar{I} = B_\nu(T)$;

$$g_0 B_{01} = g_1 B_{10} \tag{1.16}$$

and

$$A_{10} = \frac{2h\nu^3}{c^2} B_{10} \tag{1.17}$$

Each transition will produce a photon of energy $h\nu_0$ which is emitted into 4π steradians of solid angle. If we assume that the frequency dependence of radiation from the spontaneous emission is the same as the profile function $\Phi(\nu)$ governing absorption and that there are n_1 atoms per unit volume, the emission coefficient can then be written as;

$$j_\nu = \frac{h\nu}{4\pi} n_1 A_{10} \Phi(\nu) \tag{1.18}$$

Likewise, we can write the absorption coefficient:

$$\kappa_\nu = \frac{h\nu}{4\pi}(n_0 B_{01} - n_2 B_{10}\Phi(\nu)) \tag{1.19}$$

The absorption coefficient includes the effects of induced emission. Substituting Equation 1.18 and 1.19 into Equation 1.5 and using the Einstein relation in Equation 1.16 and 1.17, the absorption coefficient becomes.

$$\kappa_\nu = \frac{h\nu}{c} n_0 B_{01}(1 - e^{-h\upsilon/kT_s})\Phi(\nu) \tag{1.20}$$

Since Equation 1.20 involves the frequency integrated Einstein B coefficient we have to replace the density in the unexcited hyperfine state F_0 by the column density N_0 required by the integration over s. The optical depth is;

$$\tau_\nu = \frac{h\nu}{c} N_1 B_{01}[1 - e^{-h\nu/kT_s}]\Phi(\nu) \approx \frac{h\nu}{c} N_0 \frac{h\nu}{kT_s} B_{01}\Phi(\nu) = \frac{3hc\lambda}{8\pi kT_s}\frac{N_H}{4} A_{10}\Phi(\nu) \tag{1.21}$$

The traditional way of writing Equation 1.21 in radio astronomy is to recast the distribution of velocities in frequency units;

$$\mathbf{\Phi}(\mathbf{v})dv = \Phi(\nu)d\nu \tag{1.22}$$

The optical depth Equation becomes

$$\tau(\mathbf{v}) = \frac{3hc\lambda^2}{8\pi kT_s}\frac{N_H}{4} A_{10}\mathbf{\Phi}(\mathbf{v}) \tag{1.23}$$

Integrating Equation 1.18 over the line gives

$$\int_{line} \tau(\mathbf{v})d\mathbf{v} = \frac{N_H/T_s}{1.83 \times 10^{18} cm^{-2}K^{-1}} km/s \tag{1.24}$$

$$N_H = 1.83 \times 10^{18} T_s \int_{line} \tau(\mathbf{v})d\mathbf{v}\ \mathrm{cm}^{-2} \tag{1.25}$$

Note that there is $1/T_s$ dependence from the optical depth Equation. The HI absorption line is dependent on both the spin temperature and the optical depth. Precise measurements of T_s for an actual cloud of gas are rather difficult. Limits can be estimated from Equation 1.11: $T_B(\nu) \longrightarrow T_s$ as $\tau(\nu) \longrightarrow \infty$.

The spin temperature $\mathbf{T}_s$

The spin temperature, T_s, as illustrated in Equation 1.12 is merely a shorthand for the relative population of the singlet and triplet. However, one striking question is what determines these populations physically?. Field (1958) used the quasi-static approximation to calculate the spin temperature, T_s, as a weighted average of the brightness temperature of 21-cm radiation, averaged over all directions, T_R; the kinetic temperature of the atoms and electrons, T_K; and the color temperature of certain kinds of light, T_L. Hence, the spin

temperature could be recast as

$$T_s = \frac{T_R + y_c T_K + y_L T_L}{1 + y_c + y_L} \tag{1.26}$$

where y_c and y_L are the normalized probabilities or efficiencies for T_K and T_L respectively. The kinetic coupling term y_c is due to collisional excitation of the 21 cm transition. When one of the efficiencies is very large, T_s takes on the corresponding temperature value.
In the interstellar medium (ISM), the value of T_s is determined by the balance of heating and cooling (Walterbos and Braun 1996). The primary heat sources are cosmic rays and ionizing photons from hot stars. The main coolant in the cool ISM is radiation from the fine structure line of singly ionized carbon, CII, at λ 157.7 μ m. This line is strong only when the temperature is at least

$$kT \approx h\nu = \frac{hc}{\lambda} \tag{1.27}$$

so the cooling rate increases exponentially above

$$T = \frac{hc}{k\lambda} \approx 91K \tag{1.28}$$

The kinetic temperature of HI galaxy can be estimated from the HI line brightness temperature in direction where the line is optically thick and brightness temperature approaches the excitation temperature, which is close to the kinetic temperature in LTE (Walterbos and Braun 1996). Many lines of sight near the galactic plane have brightness temperature as high as 100-150 K, values consistent with the temperature dependent cooling rate. The spin temperature of the HI line is therefore approximately 100 K.

1.4 Thesis Layout

This thesis focuses on verifying the HI 21-cm absorption lines in 4 radio sources with regard to testing the KAT-7 capability in carrying out 21-cm absorption line studies. This is in order to prepare for a larger systematic absorption line study to be carried out on KAT-7 and later on MeerKAT. It is organized as follows. Chapter 2 contains an overview of radio interferometry fundamentals. Fundamentals, outlying the relevant maths and assumptions needed to analyze and image data from radio interferometers. A general process of calibration is described. Chapter 3 begins with an introduction to the KAT-7 array and its ability to perform HI 21-cm observations. Detailed description of selected sample and KAT-7 observational procedure is outlined. Chapter 4 is set for the data reduction used in this thesis. Details outlying each step taken in the reduction process is given. Chapter 5 contains the results and discussion. This chapter begins by describing the types and effects of radio frequency interference observed. For the study sample analyzed, the flux density and the sensitivity achieved in the final image cubes is obtained. These values are then used to calculate the spectral dynamic range. For the source with detected HI 21-cm absorption line, the optical depth, line width and HI column densities are derived. These values are

then compared with the literature. For the undetected HI 21-cm absorption line, we derive the upper limit optical depth $\tau_{3\sigma}$ which is then used to estimate the upper limit HI column density. Some of the effects that may hinder the detection of weak absorption features with the KAT-7 are also discussed in this chapter. In addition to this, we study the bandpass shapes using 3 bandpass calibrators. We identify any ambiguities present in the bandpass shapes and identify the source of these ambiguities. Lastly Chapter 6 gives the conclusion and future work on HI 21-cm absorption line studies with KAT-7.

Chapter 2

Interferometry Fundamentals

The basic requirements for any instrument used to observe astronomical sources at any wavelength are good resolution and sensitivity. The angular resolution of a filled circular aperture telescope of diameter D, at the observation wavelength of λ is given by

$$\theta = 1.22\frac{\lambda}{D} \tag{2.1}$$

At radio wavelengths, large telescope apertures for a single antenna are needed to achieve good angular resolution. The largest single radio telescope in the world is the Arecibo, with a diameter of 305m. At a wavelength of 21 cm, this corresponds to an angular resolution of 173.2 arcseconds. In order to achieve higher angular resolution, radio astronomers have developed a concept of aperture synthesis. By linking small single dishes together, an angular resolution given in Equation 2.1 may be achieved where D is not in this case the diameter of a single dish, but the distance between the most widely separated individual receivers in the array. Such method is advantageous not only in resolution achieved, but also in terms of cost. By using aperture synthesis, angular resolutions of the order of a few milliarcseconds may be achieved. This Chapter attempts to outline the theory of radio interferometry. In doing so, we follow the approach taken in Taylor et al. (1999), Thompson (1989) and Rohlfs and Wilson (2000).

2.1 The van Cittert-Zernike Theorem and spatial coherence

The van Cittert-Theorem, generalized for the case of vector fields gives the degree of coherence of the electromagnetic field. The electric field produced by an incoherent vector source increases on propagation whereas the degree of polarization remains the same. This theorem connects the spatial coherence function to the source intensity distribution of the incoming radiation. Classical electromagnetic theory gives the form of an electric field in a vacuum as

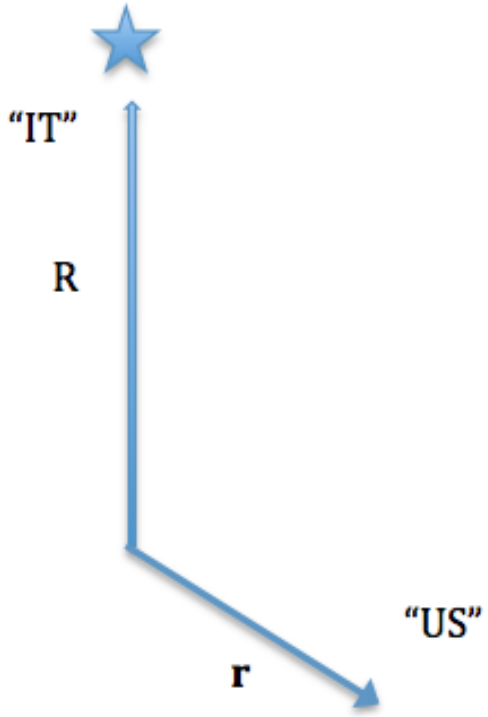

Figure 2.1: Illustration of synthesis imaging. An astronomical source at "IT" emits electric field, $\mathbf{E}(\mathbf{R}, t)$, which is observed at $\mathbf{r}$ by "US".

$$E(t) = \int_0^\infty \mathbf{E}(\nu) e^i [\phi(\nu) - 2\pi\nu t] d\nu \tag{2.2}$$

The electric field coefficient, $\mathbf{E}(\nu)$, has a form which limits the range of frequency to an interval $d\nu$;

$$\frac{\delta\nu}{\bar{\nu}} \ll 1 \tag{2.3}$$

Where if $\delta\nu$ is the mean frequency, then the signal is said to be quasi-monochromatic (Thompson 1989). If we assume that the source radiates only at one particular frequency, we can express the electric field as Fourier series and only take into account the Fourier coefficients, as a representative of the electric field at $\mathbf{R}$, $\mathbf{E}_\nu(\mathbf{R})$.
Since Maxwell′s law is linear, the response at $\mathbf{r}$ is the superposition of all fields at that location, and the measured fields takes the form:

$$\mathbf{E}_\nu(\mathbf{r}) = \int\int\int P_\nu(\mathbf{R}, \mathbf{r}) \mathbf{E}_\nu(\mathbf{R}) dx dy dz \tag{2.4}$$

where the integration in Equation 2.4 takes place over all space and $P_\nu(\mathbf{R}, \mathbf{r})$ is the propagator which indicates how the fields at $\mathbf{r}$ are influenced by the fields at $\mathbf{R}$. If we ignore the fact that the electric field is a vector quantity, assume that the distance to the source precludes all hopes of resolving any depth features, and making an assumption that the space inside the celestial sphere is empty, a third electric field, $\epsilon_\nu(\mathbf{R})$, as the electric field distribution on a giant celestial sphere of radius the absolute magnitude of $\mathbf{R}$ is defined. When we insert these assumptions in Equation 2.4, the form of the observed field at $\mathbf{r}$ becomes

$$E_\nu(\mathbf{r}) = \int \epsilon_\nu(\mathbf{R}) \frac{e^{2\pi i\nu|\mathbf{R}-\mathbf{r}|/c}}{\mathbf{R}-\mathbf{r}}\, dS \tag{2.5}$$

where dS is the surface area on the celestial sphere. This is then the electric field measured by the observer at $\mathbf{r}$ due to all sources of cosmic electromagnetic radiation.
Among the properties of $E_\nu(\mathbf{r})$ is the correlation of the field at two different locations. The correlation is defined as the expectation value of the product of the two electric fields:

$$V_\nu(\mathbf{r_1}, \mathbf{r_2}) =< E_\nu(\mathbf{r}_1 E^*_\nu(\mathbf{r}_2)) > \tag{2.6}$$

where the raised asterisk indicates the complex conjugate. The measured correlations are called visibilities. To simplify Equation 2.5 and introduce names by astronomers for quantities, we define $\mathbf{s} = \mathbf{R}/||\mathbf{R}||$, as the unit vector and $I_\nu(\mathbf{s})$ as the observed intensity and finally $d\Omega$ as the solid angle. Making the assumption that the radiation from two points of the source is uncorrelated, the following expression, the spatial coherence function, is obtained:

$$V_\nu(\mathbf{r_1}, \mathbf{r_2}) \approx \int I_\nu(\mathbf{s}) e^{-2\pi i\nu \mathbf{s}.(\mathbf{r}_1-\mathbf{r}_2)/c} d\Omega \tag{2.7}$$

Equation 2.7 resembles a Fourier transform . Notice that $V_\nu(\mathbf{r_1}, \mathbf{r_2})$ is a function of $\mathbf{r_1} - \mathbf{r_2}$, the vector difference between the locations of the two antennas. Astronomers call the vector difference between two antennas a baseline. Denoting the baseline as $\mathbf{B} = \mathbf{r_1} - \mathbf{r_2}$ and inserting this in Equation 2.7 gives

$$V_\nu(\mathbf{r_1}, \mathbf{r_2}) \approx \int I_\nu(\mathbf{s}) e^{-2\pi i\nu s.(\mathbf{B})/c} d\Omega \tag{2.8}$$

2.2 Two-Element Interferometer

The simplest way to measure the spatial coherence function of the electric field is by using an interferometer array. There are various ways in which interferometers can relate the incoming signals, but the most common practice in modern installations is to cross-correlate the signal amplitudes. In most cases the signals are just integrated within a time T after being multiplied, and this correspond to cross-correlating with zero time lag, but it is also a common practice to introduce many time lags.
If we consider two antennas as shown in Figure 2.2 pointing towards a distant radio source

in a direction indicated by unit vector **s**. **B** is the interferometer baseline, and the wavefront from the source reaches one antenna at time τ_g later than the other. τ_g is called the geometrical delay and is given by

$$\tau_g = \mathbf{B}.\mathbf{s}/c \tag{2.9}$$

where c is the speed of light. Assuming that the incoming waves reaching the antennas are perfectly aligned with the antenna polarization, we can represent the received signals by quasi-monochromatic Fourier components of frequency ν, which has the form $V_1(t) = v_1 cos 2\pi\nu(t - \tau_g)$ and $V_2(t) = v_2 cos 2\pi\nu\tau_g t$. The signals are input to a multiplying device (correlator) followed by a low pass filter such that the output is proportional to

$$R \propto \frac{1}{T}\int_0^T v_1 v_2 cos(2\pi\nu t) cos(2\pi\nu(t - \tau_g) dt \tag{2.10}$$

where T is the integrator time of the correlator and therefore a finite value. The output of the correlator thus varies periodically with τ_g, the delay time.

If we consider the radio brightness distribution be given by $I_\nu(\mathbf{s})$, the power received per

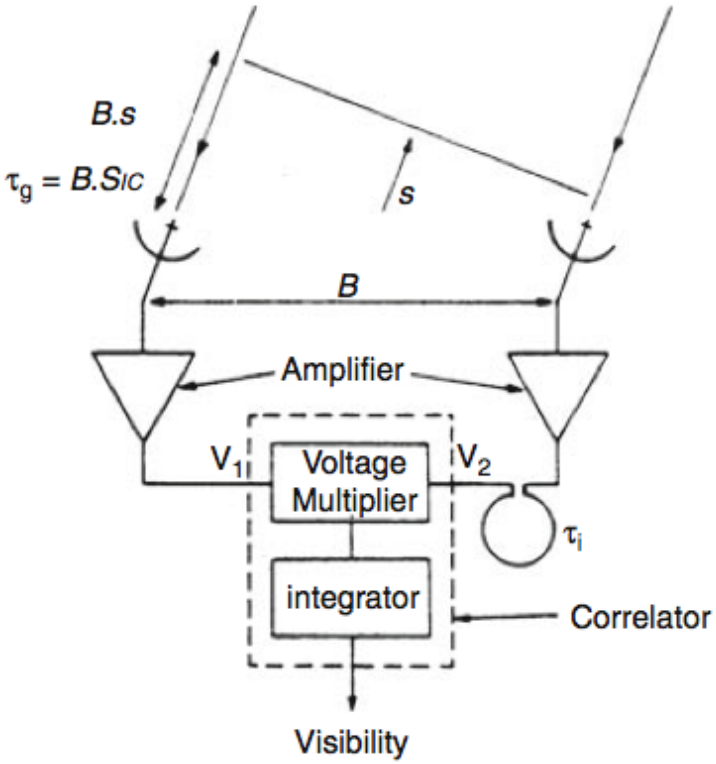

Figure 2.2: A simplied schematic diagram of a two-element interferometer (Taylor et al. 1999)

bandwidth $d\nu$ from the source element $d\Omega$ is $A(\mathbf{s})I_\nu(\mathbf{s})d\Omega d\nu$. $A(\mathbf{s})$ is the effective area in the direction **s**. The correlator output for radiation coming from the direction **s** per bandwidth

$d\nu$ is proportional to the received power and to the cosine fringe term. Omitting constant gain factors, we can represent the correlator output for the signal from solid angle $d\Omega$ by

$$dR = A(\mathbf{s})I(\mathbf{s})\Delta\nu d\Omega cos 2\pi\nu\tau_g \tag{2.11}$$

In terms of baseline and source position vectors we can rewrite Equation 2.11 as

$$R = \Delta\nu \int_S A(\mathbf{s})I(\mathbf{s})cos\frac{2\pi\nu\mathbf{B}.\mathbf{s}}{c}d\Omega \tag{2.12}$$

When taking observations to make an interferometric image of a radio source, it is useful to specify a position on which the synthesized field of view is to the centered as $\mathbf{s_0}$. We can represent this position by a vector such that $\mathbf{s} = \mathbf{s_0} + \boldsymbol{\sigma}$. Substituting this in Equation 2.12 gives

$$\begin{aligned} R \propto \Delta\nu cos(2\pi\nu\frac{\mathbf{B}.\mathbf{s}_0}{c}) \int_{source} A(\boldsymbol{\sigma})I(\boldsymbol{\sigma})cos(2\pi\nu\frac{\mathbf{B}.\boldsymbol{\sigma}}{c})d\Omega \\ - \Delta\nu\ sin(2\pi\nu\frac{\mathbf{B}.\mathbf{s}_0}{c}) \int_{source} A(\boldsymbol{\sigma})I(\boldsymbol{\sigma})sin(2\pi\nu\frac{\mathbf{B}.\boldsymbol{\sigma}}{c})d\Omega \end{aligned} \tag{2.13}$$

where the trigonometric relation $cos(\alpha+\beta) = cos\alpha.cos\beta - sin\alpha.sin\beta$ have been used. It is possible to introduce a complex quantity

$$V \equiv |V|e^{i\Phi v} = \int_S A(\boldsymbol{\sigma})I(\boldsymbol{\sigma})e^{-2\pi i\nu\mathbf{B}.\boldsymbol{\sigma}/c}d\Omega \tag{2.14}$$

where $A(\boldsymbol{\sigma}) \equiv A(\boldsymbol{\sigma})/A_0$ is the normalized antenna reception pattern, A_0 being the response at the beam center. Equation 2.14 represents the measure of the mutual coherence function of the source modified by the antenna power pattern and written in a different coordinate system. The real and imaginary parts of V in 2.14 are

$$A_0|V|cos\phi_V = \int_S A(\boldsymbol{\sigma})I(\boldsymbol{\sigma})cos\frac{2\pi\nu\mathbf{B}.\boldsymbol{\sigma}}{c}d\Omega \tag{2.15}$$

and

$$A_0|V|sin\phi_V = -\int_S A(\boldsymbol{\sigma})I(\boldsymbol{\sigma})sin\frac{2\pi\nu\mathbf{B}.\boldsymbol{\sigma}}{c}d\Omega \tag{2.16}$$

Putting together Equations (2.12, 2.14, and 2.15) and using the same trigonometric function as before, gives the correlator output as

$$\mathbf{R} = A_0\Delta\nu|V|cos(\frac{2\pi\nu\mathbf{B}.\mathbf{s}_0}{c} - \phi_V) \tag{2.17}$$

Equation 2.17 is the measure of the amplitude and phase of the fringe pattern. The visibility function defined in Equation 2.8 shows a measure of the mutual coherence between the wave field received in each of the receivers and gives a proper coordinate system that could be defined so that positions on the sky would be given in respect to the direction cosines of the

source plane measured with respect to the measurement plane. Joining this information to Equation 2.18, the correlator output is proportional to the visibility function. It is finally possible not only to establish the connection between the brightness distribution and the correlator output, but also to do it with the best choice of coordinates just by combining the information provided by Equation 2.8 and 2.17.

2.3 Effect of Bandwidth

The frequency of the cosine fringe term in Equation 2.17 is proportional to the observing frequency ν. Thus observing in finite bandwidth $\Delta\nu$ results in the combination of fringe pattern with a corresponding range of fringe frequencies. For the response with an infinitesimal bandwidth dν, combining together Equation 2.9 and 2.17 and choosing the instrumental delay such a way that $(\mathbf{B}.\mathbf{s}_0)/c - \tau_i = \tau_g$ gives the infinitesimal response as;

$$dR = A_0|V|cos(2\pi\nu\tau_g) - \phi_V)d\nu \tag{2.18}$$

Assuming a continuum source such that the time-averaged amplitude of the signal is constant over the bandpass $\Delta\nu$, that is, considering a rectangular bandpass, the interferometer response is given by integrating over the band as

$$dR = A_0|V| \int_{\nu_0-\Delta\nu/2}^{\nu_0+\Delta\nu/2} cos(2\pi\nu\tau_g - \phi_V d\nu) = A_0|V|\Delta\nu \frac{sin\pi\Delta\nu\tau_g}{\pi\Delta\nu\tau_g} cos(2\pi\nu_0\tau_g - \phi_\nu) \tag{2.19}$$

where ν_0 is the center frequency of the observing bandpass. Thus in the modulation of the signal with a rectangular bandpass, the fringes are modulated by a sinc function envelope, sometimes referred to as the fringe pattern.

2.4 Delay Tracking and Frequency Conversion

Practically all radio astronomy receivers mix the incoming signal at radio frequency, ν_{RF} to some intermediate frequency, ν_{IF}. This technique is known as frequency conversion. Frequency conversion enables the major part of the signal processing to be performed at intermediate frequencies that are most appropriate for amplification, transmission, filtering, delaying, and cross-correlation of the signal. Frequency conversions is performed with the use of a mixer, which corresponds to the upper and lower sidebands. The relationship between the mixer input frequency to the intermediate frequency, ν_{IF} is

$$\nu_{RF} = \nu_{LO} \pm \nu_{IF} \tag{2.20}$$

where ν_{LO} is the local oscillator waveform of frequency. The receivers at antenna i and antenna j must contain filtering for sideband selectivity before the mixers. It is useful to

consider the phase changes ϕ_1 and ϕ_2 imposed on the received signal when analyzing the effects the frequency conversion has on Equation 2.18. These phases are different for the upper and lower sideband cases, because the input signal is an hermitian function. If we consider the upper sidebands, the channel phases of the interferometer can simply be written as;

$$\phi_1 = 2\pi\nu_{RF}\tau_g = 2\pi(\nu_{LO} + \nu_{IF})\tau_g, \tag{2.21}$$

and

$$\phi_2 = 2\pi\nu_{IF}\tau_i + \phi_{LO} \tag{2.22}$$

where ϕ_1 and ϕ_2 are the local oscillator phase differences. The signal at antenna i is delayed by τ_g at the frequency of ν_{RF}, and this causes a phase shift of $2\pi\nu_{RF}\tau_g$. The instrumental delay, τ_i is inserted at the ν_{IF} frequency and this results in a phase delay of $2\pi\nu_{IF}\tau_i$. Inserting Equations (2.21 and 2,22) into Equation 2.18 gives;

$$r_{upper} = A_0\Delta\nu|V|\frac{sin\pi\Delta\nu\Delta\tau}{\pi\Delta\nu\Delta\tau}cos[2\pi(\nu_{LO}\tau_g + \nu_{IF0}\Delta\tau) - \phi_V - \phi_{LO}] \tag{2.23}$$

In the case of lower sideband we have;

$$\phi_1 = -2\pi(\nu_{\nu_{LO}-\nu_{IF}})\tau_g, \tag{2.24}$$

and

$$\phi_2 = 2\pi\nu_{IF}\tau_i - \phi_{LO}, \tag{2.25}$$

where

$$r_{lower} = A_0\Delta\nu|V|\frac{sin\pi\Delta\nu\Delta\tau}{\pi\Delta\nu\Delta\tau}cos[2\pi(\nu_{LO}\tau_g - \nu_{IF_O}\Delta\tau) - \phi_V - \phi_{LO}] \tag{2.26}$$

In case of higher frequencies ($\gtrsim$ 100 GHz), it is difficult to make low noise amplifiers to place ahead of the mixers. To deal with this case, double sideband systems which adds the lower and upper sidebands together are used. The resulting phase response is;

$$r_{double} = 2\Delta\nu A_0|V|\frac{sin(\pi\Delta\nu\Delta\tau}{\pi\Delta\nu\Delta\pi}cos(2\pi\nu_{LO}\tau_g - \phi_V - \phi_{LO})cos(2\pi\nu_{IF_0}\Delta\tau) \tag{2.27}$$

The delay tacking $\Delta\tau$ in Equation 2.27 does not affect the phase of the cosine and fringe as it does in Equation 2.23 and 2.26. This shows that the double sideband system requires more critical adjustment of the instrumental delay to maintain the visibility amplitude than the one sided sideband systems.

2.5 Fringe rotation and complex correlators

The output from the correlator is fed to a computer which performs some form of optimal analysis to determine the amplitudes and phases of the fringe oscillations. The fringe visibility V can then be obtained by calibration of the instrumental parameters. This calibration usually involves observation of one or more sources with known positions, flux densities, and

angular dimensions. To preserve the fringe information, it is necessary to follow the changes in the visibility V, for which values of order one second are likely to be adequate. By inserting varying phase shifts in the local oscillator signals it is possible to slow down the fringe oscillation, and reduce the computation required. If we vary ϕ_V in Equation 2.23, 2.26, and 2.27 and keep $(2\pi\nu_{LO}\tau_g - \phi_{_{LO}})$ constant, the correlator output will vary only as a result of changes in V. This process in which ϕ_{LO} is controlled is referred to as $fringe\ rotation$.
After fringe rotation, the output of the correlator is a slowly varying voltage. To measure the complex fringe amplitude in this case, the following procedure is used; For each antenna pair, a second correlator with $\pi/2$ phase shift in one input is added. The response correlator can be obtained by replacing ϕ_1 in Equations (2.21 and 2.22) and (2.24 and 2,25) by $\phi_1 - \pi/2$. Then the cosine term in Eqautions 2.23, 2.26 and 2.27 containing τ_g becomes a sine, with no change in argument. The two correlator outputs can be regarded as measuring the real and imaginary parts of the complex visibility. Such a scheme is usually referred to as a *complex correlator*

2.6 Coordinate Systems for imaging

There are two possible coordinate systems to cast to Equation 2.8 as a 2D Fourier transform. The first requires that constraining baselines to lie in plane, referred to in astronomical literature as the $u - v$ plane. The second system requires that the angular extent to the image is small. All of the baselines in a plane gives

$$\mathbf{B} = \mathbf{r_1} - \mathbf{r_2} = \lambda(u, v, w = 0) \tag{2.28}$$

$$\mathbf{s} = (l, m, n = \sqrt{(1 - l^2 - m^2)}) \tag{2.29}$$

$$d\Omega = \frac{dldm}{\sqrt{(1 - l^2 - m^2)}} \tag{2.30}$$

In Equation 2.28, λ is the wavelength for the observing frequency ν, and u, v, and w are the vector components of $\mathbf{B}$ measured in wavelength. The w axis points towards the celestial north pole, and the $u - v$ plane is parallel to the earths equator. In Equation 2.29 l, m, and n are the direction cosines of $\mathbf{s}$ for the angles from the u, v, and w axes respectively. This leads to the following expression for Equation 2.29 which is a modified Fourier transform. Substituting Equations 2.28, 2.29, and 2.30 into 2.8 yields

$$V_\nu(u, v) = \int\int I_\nu(l, m) e^{-j2\pi(ul+vm)} \frac{dldm}{\sqrt{(1 - l^2 - m^2)}}, \tag{2.31}$$

The factor of $1/\sqrt{(1 - l^2 - m^2)}$ comes from computing the Jacobian for the transformation from spherical to rectangular coordinates.

2.7 Antenna spacing and (u,v,w) components

An interferometer consists of an array of antennas and each must be assigned a location in a common reference frame. It is convenient to use a Cartesian coordinate system with axes pointing towards hour-angle $h = 0$ and declinations $\delta = 0$ for X-axis, $h = -6^h$ and $\delta = 0$ for the Y-axis, and $\delta = 90°$ toward the Z-axis as shown in Figure 2.3. The interferometer

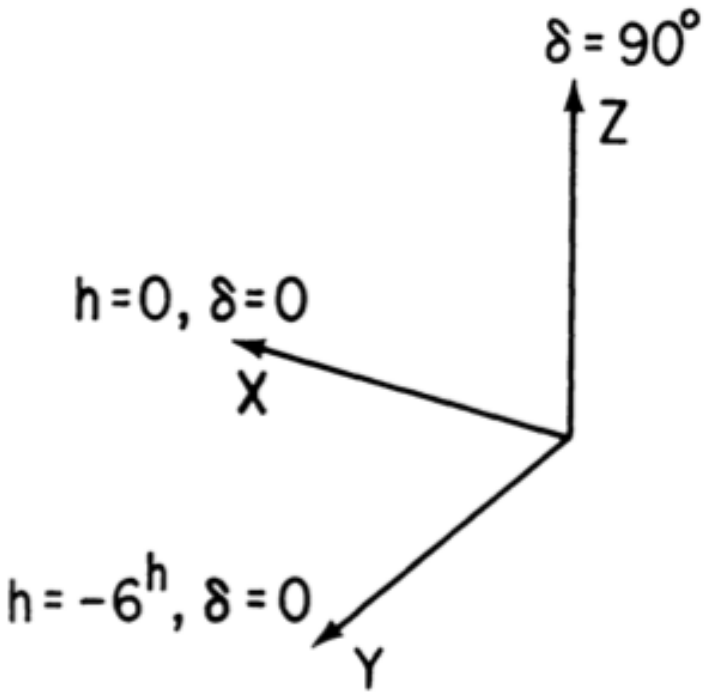

Figure 2.3: Coordinate system for specification of relative position of antennae

is not stationary in space and as the Earth rotates the orientation of the projected baseline changes, sweeping out an ellipse in the $u - v$ plane. The baseline components u, w, v are given by expression 2-30 of Taylor et al. (1999) as .

$$\begin{pmatrix} u \\ v \\ w \end{pmatrix} = \frac{1}{\lambda} \begin{pmatrix} sinH_0 & cosH_0 & 0 \\ -sin\delta_0 cosH_0 & sin\delta_0 sinH_0 & cos\delta_0 \\ cos\delta_0 cosH_0 & -cos\delta_0 sinH_0 & sin\delta_0 \end{pmatrix} \begin{pmatrix} L_X \\ L_Y \\ L_Z \end{pmatrix}$$

Here L_X, L_Y, L_Z are the coordinate differences for two antennas and H_0 and δ_0 are the equatorial coordinates (hour-angle and declination) of the chosen position in the radio

source. By eliminating H_0 from the expression for u and v we obtain the equation

$$u^2 + [\frac{v - (L_Z/\lambda)cos\delta_0}{sin\delta_0}]^2 = \frac{L_X^2 + L_Y^2}{\lambda^2} \tag{2.32}$$

As L_X, L_Y and L_Z are constants for a given pair of antennas. This is the equation of an ellipse in the u,v plane. An array of N antennas will have $N(N-1)/2$ pairs of elliptical loci. This collection of loci are known as the transfer function or sampling function, $S(u, v)$ and is a function of the declination of the celestial radio source, time duration or the observation and antenna spacing.

2.8 The effect of bandwidth in radio images

The receiver passbands and the correlation process result in one or more channel of finite width, $\Delta\nu$. However, the visibility data are treated as if they are measured at a single central frequency of ν. This point actually represents an averaging across the band width, $\Delta\nu$, of the channel. If the degree of averaging is significant then this may lead to visible distortion in the image plane in the form of radial smearing. The effect is a form of chromatic aberration and is commonly referred to by radio astronomers as bandwidth smearing. Bandwidth smearing can be explained as averaging over high frequency variations in the visibilities in the $u - v$ plane in orthogonal directions.
Assuming a square bandpass, with no tapering and a square $u - v$ coverage, the width of the radial distortion of the observed source by bandwidth smearing increases as $\Delta\nu\Theta_0$, whereas the peak of smearing increases with distance from the phase center, Θ_0, of the observation and with the bandwidth , $\Delta\nu$. In general, the smearing process preserves the integrated flux of the source and may be recovered through deconvolution. The source structure, however, cannot be recovered as averaging across the band destroys this information.
The simple strategy of reducing the effect of bandwidth smearing is to correlate data into large numbers of narrow band spectral channels and calculate the $u - v$ locations for each channel separately. This technique, can dramatically reduce the effect of bandwidth smearing and as an added bonus can also be used to increase the overall $u - v$ coverage of an observation.

2.9 The effect of visibility averaging

The averaging of visibility data over time is one cause of image smearing and is referred to as time-averaging smearing. Visibility data output from a correlator are averaged over a specified time, τ_a, and assigned a $u - v$ value that corresponds to the midpoint of the averaging period. However, during this period the baseline vector would not have remained constant. The rotation of the Earth would have caused the vector to rotate through $\omega_E\Delta\tau$, where ω_E is the angular velocity of the earth. Where this rotation is significant, the $u - v$ points are effectively under-sampled. The effect on the image plane is complex and depends

greatly on the location of the source in the Celestial Sphere. However, the general effect is a loss of peak amplitude. Furthermore, the magnitude of this loss increases with τ_a and with the distance of the source from the phase center, Θ_0, and so is also an important effect to consider in imaging.
To correct for the effect of time averaging, the correlator needs to generate visibilities with fine enough temporal resolution i.e small τ_a. Traditional correlators are limited in the temporal resolution in which they can output visibilities and secondly, for each halving of τ_a there is a subsequent doubling in visibility data. Fortunately, the flexibility of software correlators can at least alleviate the first of these issues with their ability to output data at any desired temporal resolution within fundamental limits i.e high time resolution imposes limits on the frequency resolution and vise versa.

2.10 Aperture synthesis and imaging

When a telescopes collects the observed visibilities, we talk of filling in the $u-v$ plane. Filling in the $u-v$ plane becomes possible by using the rotation of the Earth. This is known as aperture synthesis. As the Earth rotates, the source sees the baseline vector rotating, tracing a circle on the sky providing extended coverage of Fourier components by changing the length and orientation as shown in Figure 2.4. Aperture synthesis improves with increasing antennas. The better the $u-v$ plane is filled, the better the image quality achieved in the final image cube. Straight forward method of obtaining an intensity distribution from the

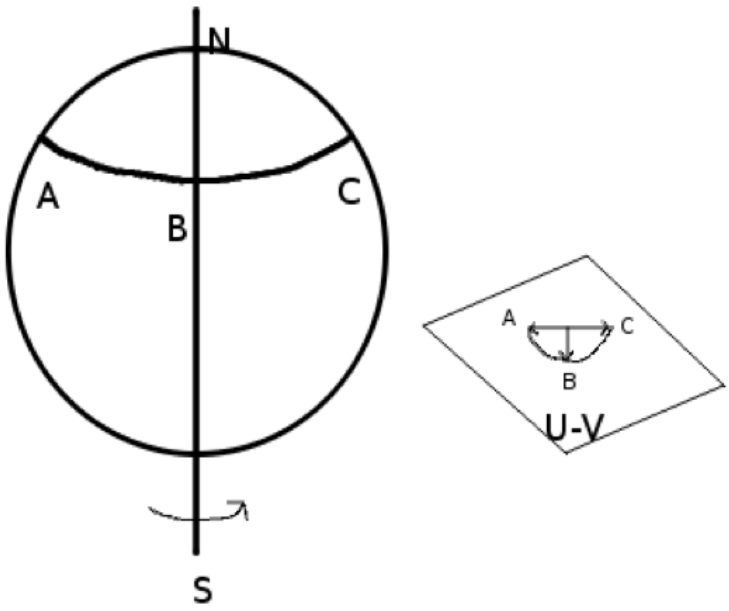

Figure 2.4: Aperture Synthesis illustrated [7]

[7] http: //gmrt.ncra.tifr.res.in/gmrt_hpage/

measured visibility data is by direct Fourier transformation. An inverse Fourier transform may be applied to find the sky brightness modified by the antenna reception. Using Equation 2.9, the inverse Fourier transform is given by

$$A_\nu(l,m)I_\nu(l,m) = \int\int V(u,v)e^{-2\pi i(ul+vm)}dudv \tag{2.33}$$

where A_ν is the primary beam or reception beam pattern. The Fourier transform into the image plane may be accomplished either via a direct Fourier transform, evaluated at every point of an N × N grid, or via a fast Fourier transform (FFT) algorithm. The most commonly used method is the FFT. FFT algorithm requires interpolation of data onto a regular rectangular grid. This requires having information on the cell size (pixel size) and the image size (number of pixels to be imaged). The image size must be a power of 2 to allow for fast Fourier transformation. Knowing the maximum baseline (B_{max}) of the data and the observing wavelength, we can write the beam size in arcseconds as

$$\theta = \frac{3600 \times 180}{\pi B_{\max}}\text{arcsec} \tag{2.34}$$

In order to sample the beam properly, beam size is divided by the value of 4 to get the desired pixel size.
The image size is derived from the primary beam (resolution of the single dish);

$$\text{primary beam} = \frac{1.02 \times c/\nu}{D}\text{radians} \tag{2.35}$$

D is the diameter of a single dish, ν is the observing frequency and c is the speed of light. To check for confusion sources in the field of view and clean them out, the primary beam is multiplied by a factor of 3.

2.11 Calibration

The observed visibilities are generally affected by instrumental malfunctions and RFI. In order to determine the true visibilities from the observed visibilities, the process of editing and calibration is carried out. Editing is the examining and deleting of bad and corrupted data observed in the visibilities. Calibration is the process of correcting the observed visibilities to obtain the true visibilities. For one antenna pair (baseline) i and j, the relationship between the observed visibilities V_{ij}^{obs} and true visibilities V_{ij}(t) is given by

$$V_{ij}^{obs}(t) = G_{ij}(t)V_{ij}(t) + \eta_{ij}(t) \tag{2.36}$$

where t is the time of the observation, $G_{ij}(t)$ is the complex gain associated with a particular baseline, and $\eta_{ij}(t)$ is the offset for that antenna pair. One way of performing calibration is to use observations of a point source of known flux density S and position. The most straight forward use of calibrator observations is called the baseline-based calibration. A

point source calibrator of known flux density S and position is used. The true visibility amplitude will be S Jy, and the phase will be 0. The estimate of the gains will be

$$G_{ij}(t)V_{ij}(t) = \frac{V_{ij}^{obs}(t)}{S} \tag{2.37}$$

The offset term $\eta_{ij}(t)$ is assumed to be negligible after averaging of data in the scan. The antenna-based solution for amplitude and phase is another way of performing calibration. Since data is corrupted before the signals are correlated, it is convenient to write the baseline-based complex gain $G_{ij}(t)$ as

$$G_{ij}(t) = g_i(t)g_j^*(t)g_{ij}(t) \tag{2.38}$$

where $g_i(t)$ is the antenna based complex gain for antenna i and g_{ij}(t) is the residual baseline-based complex gain. These complex numbers can be separated into amplitude and phase:

$$A_{ij}(t) = a_i(t)a_j(t)a_{ij}(t) \tag{2.39}$$

and

$$\phi_{ij}(t) = \phi_i(t) - \phi_j(t) + \phi_{ij}(t) \tag{2.40}$$

Let us write the true and observed visibilities as $V_{ij} = A_{ij}e^{i\varphi_{ij}}$ and $V_{ij}^{obs} = \tilde{A}_{ij}e^{e^{i\tilde{\varphi}_{ij}}}$. Then for a point source the measured amplitude and phase are

$$\tilde{A}_{ij} = a_i a_j a_{ij} S \tag{2.41}$$

and

$$\tilde{\phi_{ij}} = \phi_i - \phi_j + \phi_{ij} \tag{2.42}$$

which can be solved for a_i and ϕ_i for all N antennas, provided g_{ij} is close to unity. This terms is commonly called the closure error. Using a least squares method (using logarithms for the amplitude terms) the error terms can then be checked to show if there is any problem. These errors are acceptable when $\tilde{A_{ij}}$ is within 1% of 1.00 and $\tilde{\phi}_{ij} < 1$ degree.
The advantages of antenna-based solutions over bandpass based calibrations is that firstly, antenna based solutions can be obtained even without all the baselines. This is especially important for partially resolved or confused calibrators. In this case one simply applies the solution on baseline that meet the criteria so that the source is a good point source and secondly, most variations in the instrument are related to particular antennas, whether they arise from the medium above the antenna or the electronic components. The errors due to a well designed correlator are always smaller.
Calibration methods depend on the detailed design of the array, the severity of the problem etc. Calibration methods can be divided into three basic categories.

Direct Calibrations The engineering knowledge of the system is important and requires frequent characterization of equipment stability with time, or model of variation with time.

Where instabilities and variations cannot be avoided, special feedback circuitry and the monitoring of critical parameters within the array system and the enviroment around the array can be used to correct for these changes as observations progress (Fomalont and Perley 1999).

Astronomical Calibrations This involves the use of calibrator sources whose visibility can be accurately predicted and modeled. To calibrate varying components will require frequent observation of a close calibrator source. Since an interferometer measures phase differences, there is no absolute phase reference. For any given observation, we wish to reference the visibility phases to the phase tracking center, which is generally the same position as the center of the primary beam (Fomalont and Perley 1999). To determine antenna phase offsets, observation of the sky calibrator are required. Further, if the array is not completely phase or gain stable, periodic observations of calibrators are used to monitor these changes. Finally, the atmosphere will cause time variable phase changes to occur in the data, and observations of a calibrator source are often in attempt to remove this effect (Fomalont and Perley 1999).

Self Calibration The initial calibration of the visibilities transfers the gains of the calibrators to the target source. The observations of the calibrator and target are separated in distance and are observed at different times. Since the atmosphere varies in time and has non uniform structure, these gains are unlikely to be correct for the observations of the target source. Self calibration uses a model of the target source itself to solve for improved values of the complex antenna gains. The gains are thus iteratively derived for the correct time and direction, and the solution is fairly robust as long as there are many baselines. However, the results do depend upon the assumed model. An incorrect model will incorporate errors into the derived gains and produce incorrect images.
In order to solve for the gains, a least square solution us used to minimize the difference S between the model visibilities $\hat{V}$ and the observed visibilities V^{obs}.

$$S = \sum_k \sum_{i,j} = w_{ij}(t_k)|V_{ij}^{obs}(t_k) - g_i(t_k)g_j^*(t_k)\hat{V}_{ij}(t_k)|^2, \tag{2.43}$$

where w_{ij} are the weights for baselines i and j at time t_k. An initial model is typically either a point source or and initial image of the source. The image is then divided by the model visibilities to produce a pseudo-point source

$$S = \sum_k \sum_{i,j} w_{ij}(t_k)|\hat{V}_{ij}(t_k)|^2|X_{ij}(t_k) - g_i(t_k)g_j^*(k)|^2 \tag{2.44}$$

where X_{ij} is the ratio of observed to model visibilities,

$$X_{ij}(t) = \frac{V_{ij}^{obs}(t)}{\hat{V}_{ij}(t)} \tag{2.45}$$

If the model is correct, X_{ij} will be independent of u and v and proportional to the antenna gains, so its values will simulate the response to a calibrator source, allowing determination of the gains. Since the initial model is only approximate, an iterative procedure is used to obtain the best result. It is thus important to exclude any features of the model due to the calibration errors themselves, or they will never be removed. Typically, all CLEAN components after the first negative one in each model image are neglected.
Self calibration will fail if the signal to noise ratio (SNR) is too low, or if the source structure is too complex for the model. In the former case, the visibilities should be averaged over a finite time interval to increase the SNR. However, if the time taken for the noise per antenna to equal the source flux density is greater than the timescale for gain variations, self calibration will not be possible.
Initially, the model visibilities may represent the true phases well but the amplitude poorly. Correcting the amplitude using such a model could result in severe errors in later iterations. Hence it is customary to self calibrate only the phase. We have no knowledge of absolute phase and hence self calibration requires defining a reference antenna to have zero phase, taken as the same antenna used in the initial calibration. This results in the loss of positional information about the source. If amplitude errors remain after phase calibration, an amplitude and phase self calibration can then be used. In this case, unless the image was of a point source model, it is necessary to have a good previous image to use as a model.

2.12 Weighting the visibility data

The observed visibilities are not fully sampled in the $u-v$ plane. The incomplete sampling of the $u-v$ plane means that there is missing information about the sky brightness. The convolution with the synthesized beam implies that a point source in the sky will produce the point source spread function (PSF) in the dirty image. The detailed shape of the point spread function can be controlled by weighting function denoted by w_k. In aperture synthesis, if the data were obtained with an uniform array of antennas and receivers all with the same average time, then the variances should all be the same and maximum signal to noise ratio would be obtained by including all measurements with the same weight. This is known as *natural weighting*. *Natural weighting* gives the best signal to noise ratio. When data contains a Gaussian noise (σ_k), then the *natural weighting* is inversely proportional to the square of the noise.

$$w_k = 1/\sigma_k^2 \tag{2.46}$$

In practice, this may not give the optimum beam shape, since real interferometers tend to sample the inner regions of the $u-v$ plane more fully than the outer parts. This leads to higher weights to lower spatial frequencies, and results in a beam with a broad, low level plateau from short spacing data. To improve the resolution, uniform weighting may be used, which weights the points inversely as their density in the $u-v$ plane.

$$w_k = 1/\rho(u,v) \tag{2.47}$$

where $\rho(u,v)dudv$ is the density of the sample in the $u-v$ plane.
Uniform weighting is best for maximizing the resolution of an image, whereas natural weighting maximizes the signal to noise ratio (good for detecting weak sources). Once the desired weighting function has been used to perform the Fourier transform into the image plane, it is necessary to deconvolve the PSF from the dirty image to obtain the true sky brightness distribution $I_\nu(l,m)$. A hybrid form of *uniform* and *natural weighting* called *robust weighting* has been recently been introduced, which arises from a minimization of the summed side lobe power and thermal noise.
Another important factor to take into account when dealing with data sampling in radio interferometers is aliasing. Aliasing is a phenomenon which occurs when a Fourier sum is made over data which are regularly spaced. In this case, there is no way to discriminate between a phase changes of 0, $2\pi, 4\pi$,.....per cell. When data is sampled, we generate a regularity which enables emission from outside the image to appear in it. From a Fourier series point of view, the transform of a regularly gridded function is itself a regularly gridded function, in the case, the image is itself replicated indefinitely in all directions. Aliasing can be managed by making the image bigger so that all real emission lies within the transformed area.

2.13 Deconvolution

Synthesis images are mainly limited by limited distribution of spatial frequencies in $u-v$ plane and the errors in the measurements. Since the Fourier transform of a convolution is equal to the product of the Fourier transform of the components, deconvolution might be achieved by dividing the Fourier transform of the dirty image in the $u-v$ plane of the beam. Unfortunately, since the $u-v$ plane is not sampled everywhere, the beam contains areas with empty visibilities. Including this and Fourier inverting the visibility measurement by interferometer gives

$$I_\nu^D(u,v) = \int\int V_\nu(l,m)S(l,m)e^{-2\pi i(ul+vm)}dldm \tag{2.48}$$

The set of Fourier inverted visibilities $I_\nu^D(u,v)$ is referred to as the dirty image and $S(l,m)$ is the sampling function. To obtain the true set of intensity values $I_\nu(u,v)$, the synthesized beam B corresponding to the sampling function must be deconvolved from the true intensity distribution

$$I_\nu^D(u,v) = I_\nu * B \tag{2.49}$$

where B is the synthesized beam or point source spread function, related to the sampling function by

$$B(u,v) = \int\int S(l,m)e^{-2\pi i(ul+vm)}dldm \tag{2.50}$$

Deconvolution is generally carried out using the $CLEAN$ algorithm. The Högbom algorithm is the most commonly used for deconvolution. This is basically a numerical deconvolution

process applied on the major cycle, the original visibilities ($u-v$ domain). The procedure is to break down the intensity distribution into point source responses, and then replace each one with the corresponding response to a clean beam, that is, beam free of sidelobes. For the H*ögbom* algorithm deconvolution, the $CLEAN$ proceeds as follows:

I Compute the map and the response to a point source by Fourier transformation of the visibilities and the weighted transfer function, that is compute, the synthesized intensity and the synthesized beam. It is essential that the spacing between the sample points in the $u-v$ plane do not exceed one-third of the synthesized beam-width.

II Find the maximum peak and its position in the dirty image. This correspond to the greatest intensity in the dirty image.

III Subtract the peak position from the dirty image. The amplitude of the peak position is the combination of the of the signal with the damping factor $0 < \gamma < 1$. γ is referred to as a loop gain, by analogy with feedback in electrical systems. The subtracted peak is then added to a model that will become a CLEANed map.

IV The rms is used to stop the iterative search of CLEAN. Until the defined stopping criteria is not satisfied steps II and III should be repeated. If the stopping criteria is satisfied proceed to step V.

V Convolve the accumulated point sources with an idealized beam, usually with reduced or with zero sidelobes and add the residuals of the dirty image to the clean image.
Apart from there $CLEAN$ algorithm, we also have the maximum entropy method (MEM) which tries to produce a map that agrees with the measured visibilities to within the noise level, while constraining the result in order to minimize some measure of the quality of the image. Thus, as the name indicates, in MEM a function $F(I')$ is defined and referred to as the entropy of the distribution and $I'(l,m)$ is the intensity distribution derived by the maximum entropy method. In constructing the map $F(I')$ is maximized within the constraint that the Fourier transform of I' should fit the measured visibilities, so MEM is all about choosing $F(I')$ so that maximization of both allows to introduce some prior information and, at the same time, let the unmeasured visibilities to assume values that minimize the detail introduced. One possible definition of entropy is given by

$$F(I') = -\sum I'_i[In[(I'_i/M_i) - 1], \tag{2.51}$$

where $I'_i(l,m) = I$, and M_i is the reference image incorporating all prior knowledge, that is, a model image and the sum is taken over all pixels in the map. The main feature of maps derived using MEM or related methods is that point source response varies with the position, so that angular resolution is not constant over the map and experience shows that MEM is able to provide some increase in resolution over other mapping techniques.

Chapter 3

Sample Selection and Observation

We selected four radio sources from the literature to test the capability of 25-MHz observing mode at KAT-7 in carrying out HI 21-cm absorption line studies. All the four radio sources have HI 21-cm absorption line detections reported in the literature are observable with KAT-7 on the basis of (i) source declination, and (ii) redshifted 21-cm line frequency. In this chapter we describe the Karoo Array Telescope (KAT-7) and present the known parameters of each source in our sample. The known properties for each source are compiled from the literature and NASA/IPAC Extragalactic Database (NED).

3.1 Karoo Telescope Array

KAT-7 is a sensitive aperture synthesis radio telescope array operating at frequency range of 1200-1959 MHz. The array was built as an engineering testbed for the MeerKAT, which is the South African pathfinder for the Square Kilometer Array (SKA). The array is situated in the Northern Cape Karoo desert. The site coordinate are latitude -30:43:17.34 and longitude 21:24:38.46 at an elevation of 1038 m. Construction of KAT-7 started in early 2008 and was completed in December 2010. KAT-7 consists of 7 antennas each of diameter 12 m. The array is very compact with baselines ranging from 26 m to 185 m and is built at low frequency making it suitable for observing diffused extended structures. KAT-7 dishes have a prime-focus altitude-azimuth (alt-az), designed with a focal length (f) to telescope diameter (D) ratio of $f/D = 0.38$, optimized for a single-pixel L-band feed. The digital backend of the system is a Field Programmed Gate Array (FPGA)-based, flexible packetised correlator using the Reconfigurable Open Architecture Computing Hardware (ROACH), which is a flexible and scalable system

enabling spectral line modes covering a wide range of resolutions (Lucero et al. 2014). Currently KAT-7 is operating using 4 correlator modes *viz*: c16n2M4k with the total usable bandwidth of 1.5625 MHz, c16n7M4k with total usable bandwidth 6.25 MHz, c16n25M4k with the total usable bandwidth 25 MHz, and finally c16n400M4k with total usable bandwidth of 256 MHz. Figure 3.1 shows the KAT-7 array telescope, while Tables 3.1 and 3.2 summarize the important parameters of the array.

Figure 3.1: KAT-7 Array configuration (Lucero et al. 2014).

Table 3.1: KAT-7 parameters (Lucero et al. 2014).

Parameter	Value
Number of antennas	7
Dish Diamter	12 m
Minimum baseline	26 m
Maximum baseline	185 m
Frequency Range	1200-1959 MHz
Maximum instataneous bandwidth	256 MHz
T_{sys}	30K
Aperature efficiency	0.65
System Eqivalent Flux Density	1100Jy
Latitude	-30:43:17:34
Longitude	21:24:38:46
Elevation	1038 m
Digital back-end	ROACH boards

Table 3.2: KAT-7 correlator mode (Lucero et al. 2014).

Mode	Total usable bandwidth(MHz)	Number of channel	Channel bandwidth(kHz)
c16n2M4k	1.5625	4096	0.381
c16n7M4k	6.25	4096	1.526
c16n25M4k	25	4096	6.104
c16n400M4k	256	1024	390.625

3.1.1 KAT-7 resolution, sensitivity and spectral dynamic range

• **Resolution** One key function of a radio telescope is the ability to resolve distant objects clearly. This is referred to as telescope resolution. The better the resolution, the more detail about the object we can retrieve from the observation. The resolution of an interferometer like KAT-7, as defined in Equation 2.1 is given by

$$\theta = 1.22\frac{\lambda}{B}\text{radians} \tag{3.1}$$

where B is the maximum baseline and λ is the wavelength of observation. For KAT-7 with frequency coverage of 1200 MHz to 1959 MHz, and maximum baseline of 185m, the resolution range is 3.3 to 5.5 arcmin. KAT-7 resolution is suitable for observing extended structures.

• **Sensitivity** Sensitivity is the measure of the weakest source signal that can be detected by a telescope. Sensitivity is critical in preparing a technically sound observing proposal to obtain reasonable results. When observing a weak source, the image sensitivity will be the combined sensitivity of all the interferometer combinations integrated over the time and bandwidth on target. This noise limit will determine the weakest feature that can be detected in the absence of other imaging limitations, such as dynamic range (Wrobel and Walker 1999). The sensitivity of a single polarization image formed with an inhomogenous array of N identical antennas is given by

$$\Delta I_m = \frac{1}{\eta_s}\frac{SEFD}{\sqrt{(N(N-1)\Delta\nu t_{int})}} \tag{3.2}$$

where t_{int} is the total integration time, $\Delta\nu$ is the total observing bandwidth, η_s is the system efficiency, which accounts for various losses in the electronics and digital equipment, and SEFD is the System Equivalent Flux Density and is calculated using

$$SEFD = \frac{T_{sys}}{K} \tag{3.3}$$

T_{sys} is the system temperature and K is given by

$$K = \frac{\eta_a A}{2k_B} \tag{3.4}$$

k_B is the Boltzmann constant, A is the area of the antenna, and η_a is the antenna efficiency. The factor of 2 accounts for the fact that single channel receiver is only able to accept half of the total radiation from an unpolarized source.
If dual polarization data are available, then the sensitivity of an angle of stokes parameter I,Q,U, or V will obey Gaussian statistics characterized by a zero mean and a standard deviation

$$\Delta I = \Delta Q = \Delta U = \Delta V = \frac{\Delta I_m}{\sqrt{2}} \tag{3.5}$$

For KAT-7, the System Equivalent Flux Density (SEFD) is around 1100 Jy and the system efficiency ($\eta_s = 60\%$). For a total integration time of 1 hr, total bandwidth of 18 MHz, the expected sensitivity for dual polarization is ≈ 0.1 mJy/beam (using natural weighting in CLEAN). This means that in order to detect weak sources, we need to increase the total integration time.

- **Spectral dynamic range(SDR)** When carrying out spectral line observations using an interferometer, one quality of a spectral line cube is the spectral dynamic range. SDR is an excellent diagnostic of instrumental performance and calibration methods and is defined as a ratio of the peak continuum signal to the root mean squared (rms) noise in the continuum subtracted image;

$$\text{SDR} = \frac{\text{peak continuum signal (Jy)}}{\text{rms in continuum subtracted image(Jy)}} \tag{3.6}$$

High dynamic range is usually affected by gaps in the spatial frequency ($u-v$ coverage) and instability of bandpass as a function of time. Dynamic range is vital for detecting faint lines superimposed on a strong continuum source. This is because the separation between the line and the continuum is very small and requires careful measures when subtracting the spectrum from the continuum. For an observation that is well calibrated and unaffected by instrumental problems, a spectral dynamic range of the order 10^4:1 or more can be achieved for interferometers like the Australian Telescope Compact Array(ATCA) (Wilson et al. 2011).

3.2 Observed sample

This section gives a summary of what is known about all the sources used in this thesis. A justification of the choice of this set of sources as our sample for this study is provided. The summary of some of the source parameters are presented in Table 3.3 .

- **PKS1318-43** is a radio source identified with the elliptical galaxy NGC5090. The source is believed to be part of an interacting system together with a nearby spectral galaxy NGC5091 (Lloyd et al. 1996). It is a typical FR I radio galaxy, identified with a symmetric arcsecond scale jet. PKS1318-43 is located at RA 13:18:20 and DEC -43:26:00, a distance of $z = 0.0114$ (Tadhunter et al. 1993).
At 4.796 GHz, the source has a total extension of 17 arcmin (Lloyd et al. 1996). The source has a strong core component from which a bright jet originates. The most prominent feature of the arc second scale jets is their strong S bend shape, from the region closest to the core out to the end of the jets. The source has a flux density of 5.92 Jy at 1414 MHz and the surface brightness appears to be symmetric about the core. HI 21-cm absorption has been detected (Morganti et al. 2001) using the Australia Telescope Compact Array (ATCA) telescope. The detected HI profile is reported to be double peaked with the HI systematic velocity derived as an arithmetic mean of the velocities at 3435 kms^{-1}. The absorption profile has a line width of W_{20} is 150kms^{-1}, optical depth of ≈ 0.29 and line depth Δ S ≈ 0.008 Jy. Using the radiometer equation as defined in Equation 3.2,

$$\Delta I_m = \frac{1}{\sqrt{2}} \frac{1}{\eta_s} \frac{SEFD}{\sqrt{(N(N-1)ChanWid\ t_{int})}} \tag{3.7}$$

the total integration time required to detect the absorption feature in PKS1318-43 of flux density 0.008 Jy was calculated to be 17 hours, given the channel width of ($ChanWid$ = 6.104 kHz), total number of working antenna as, ($N = 7$), KAT-7 System Equivalent Flux Density ($SEFD \sim 1100$ Jy), and the KAT-7 system efficiency of $\eta_s = 60\%$. Due to the long integration time required to observe PKS1318-43, the source was chosen to be ideal for studying the telescope performance over long integration periods.

- **PKS1549-79** is identified as a compact flat spectrum source located at RA 15:56:58 and DEC -79:14:04 at a redshift of $z = 0.1522$ (Tadhunter et al. 1993). At optical wavelength, the source image reveals tidal features indicating the presence of recent merger interactions (Tadhunter et al. 2001).
At radio wavelength observations, the source structure reveals a one sided jet structure emanating from an unresolved core source, with the unresolved core dominating the flux at 2.3 GHz. The jet has a distorted structure bending through an angle of 60 ° on the North-East (NE) side of the nucleus, whereas the unresolved radio core has a relatively flat spectrum. The total extent of the radio source in the Very Long Baseline Interferometry (VLBI) map is 150 mas (Tadhunter et al. 2001). HI 21-cm absorption line has been detected towards the source (Morganti et al. 2001) using the Australian Telescope Compact Array (ATCA) telescope. The HI absorption line detected peaks at a systematic velocity $\approx$ 45580 kms^{-1} with a line width W_{20} = 100kms^{-1}, optical depth of ≈ 0.25, and line depth of 0.120 Jy.
Due to the angular size of PKS1549-79, the source is unresolved when observed at

KAT-7 angular resolutions and because of its compactness, the source is identified as a potential calibrator for KAT-7. The source is also listed among the calibrator sources for the Australian Telescope Compact Array (ATCA) by the Australian Telescope National Facility [8]. Calibrator sources such as PKS1549-79 are ideal for studying the calibration strategies and telescope performance because of their known visibilities (constant amplitude and zero phase).

- **PKS1717-00** is the fourth brightest extragalactic radio source in the 3C catalog located at RA 17:20:19 and DEC -00:58:24. The source has been identified with an elliptical galaxy at a redshift of $z = 0.0304$ (Veron-Cetty and Veron 1998). PKS1717-00 is a strong FR II radio galaxy with absolute radio power of 4.5×10^{25} WHz^{-1}, just above the range where the transition from edge darkened FR I to edge brightened FR II morphology occurs in radio galaxies.
At radio observations, PKS1717-00 has a complex large scale radio structure elongated perpendicular to the dust lane. The source is resolved with angular size of 4.8 arcmin and strength 57 Jy at 1.4 GHz (Bridle and Williamson 1989). The radio image of PKS1717-00 shows a well collimated jets and counter jets. The radio core of PKS1717-00 has the flux of 0.15 Jy and angular size of 15 mas (Fomalont et al. 2000). At the position of the radio core, a broad, shallow HI absorption line with depth 0.010 Jy was previously detected (Morganti et al. 2001) using the Very Large Array (VLA). The absorption profile was reported at a systematic velocity 1920 kms^{-1} ($z \approx 0.0304$) with an optical depth τ of ≈ 0.11 and line width $W_{20} \approx 300 kms^{-1}$.
The HI profile in PKS1717-00 is shallow and broad detected in the presence of a strong continuum source. This means that a good spectral dynamic range is required to detect such a spectral feature. For this reason, PKS1717-00 is best suited for examining the spectral dynamic range achieved during observation and for determining telescope performance in detecting weak spectral features.

- **PKS1814-63** is defined as a rare powerful FR II radio source. The source coordinates are RA 18:19:43 and DEC -63:45:48 observed at a redshift of z=0.0646 (Holt et al. 2008). PKS1814-63 has a radio power of $P_{5GHz} = 4.1\times10^{25} WHz^{-1}$ which falls well above the radio power boundary between FR I and FR II radio sources ($P_{5GHz} \approx 10^{25} WHz^{-1}$) (Morganti et al. 2011). At optical wavelength, the morphology of this source is dominated by a strong disk component and its properties are mostly associated with Seyfert galaxies than they do with radio galaxies.
At radio wavelengths, PKS1814-63 is identified as a compact steep spectrum (CSS) with an overall extent of 0.41 arcsec (Morganti et al. 2001). The source has a continuum flux density of 12.3 Jy at 1414 MHz as recorded by NASA/IPAC Extragalactic Database (NED) [9]. HI absorption with high optical depth has been detected in PKS1814-63 by

[8] http://www.narrabri.atnf.csiro.au/calibrators/
[9] https://ned.ipac.caltech.edu/

Morganti et al. (2001) and Véron-Cetty et al. (2000). The profile was detected at a systematic velocity of 19180 kms^{-1} (corresponding to z $\approx$ 0.0639). The reported line profile had a narrow line width $W_{20} \approx 75 kms^{-1}$, peak optical depth $\tau \approx 0.21$ and line depth ΔS of 2.28 Jy.

PKS1814-63 is unresolved at KAT-7 angular resolution and because of its a compactness, it has been identified as a calibrator for KAT-7. The source is also listed among the calibrator sources for the Australian Telescope Compact Array (ATCA) by the Australian Telescope National Facility [8]. Figure 3.2 shows the continuum image of PKS1814-63 at 1334 MHz observed with the KAT-7. The source is seen to be unresolved with the total integration flux density of 13.03 Jy $\pm$ 0.021 Jy and the peak flux of 12.97 Jy/beam $\pm$ 0.021 Jy/beam, giving the ratio of the flux density to peak brightness of 0.99.

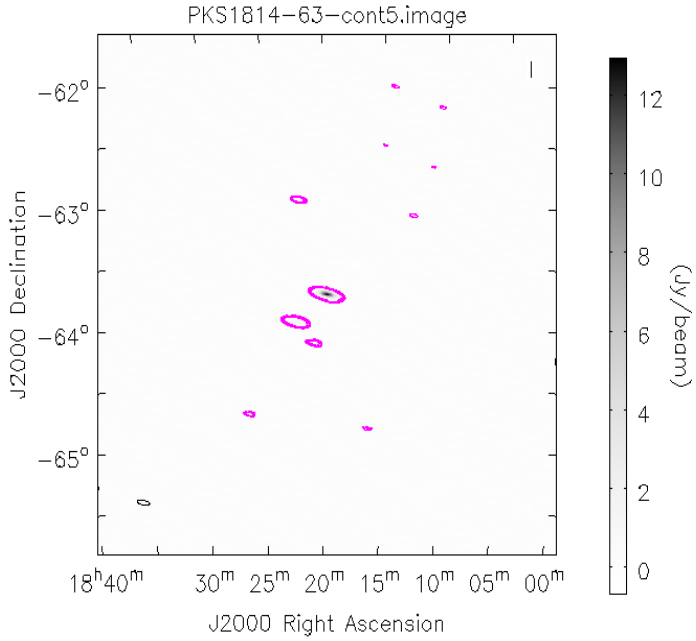

Figure 3.2: KAT-7 1.33 GHz radio image of PKS1814-63. The image has a peak brightness of 12.97 Jy/beam $\pm$ 0.021 Jy/beam with integrated flux density of 13.03 Jy $\pm$ 0.021 Jy. The off-source noise level in the image is 2 mJy/beam. The contours are drawn at [-3,3,6,12,20,24] $\times$ 2 mJy/beam. The synthesized beam is 424.9$''\times$ 137.2$''$ at a position of 79.4°.

- **PKS1934-638** is a gigahertz peaked spectrum source located at RA 19:34:47 and DEC -63:49:38, at a redshift of $z = 0.1850$. The source has been identified to have a known, bright, and stable flux density (Tzioumis et al. 2010). Due to its brightness and less variability in flux density over long periods of time, the source is a preferred flux density and bandpass calibrator for ATCA at frequencies from 1 GHz to 25 GHz [8]. The plot of amplitude vs time (Figure 3.3) at different frequencies reveals the source constant flux density. For example, at 2100 GHz, the flux densities measured between 2007 and 2015 had almost equal magnitudes of $\sim$ 12.5 Jy. Similarly, at 5500 GHz, the flux densities measured between 2004 to 2015 show almost constant magnitude of $\sim$ 5mJy making it a good choice for flux density calibration. The continuum image of

Figure 3.3: The plot of flux density vs time for PKS1934-63 from ATCA database at frequencies of 2100 MHz (red points) and 5500 MHz (light magenta points)[8] .

PKS1934-638 obtained with the KAT-7 at 1.37 GHz shows that the source is a point source with the integrated flux density of 14.8 Jy $\pm$ 0.00044 Jy and peak brightness of 14.8 Jy/beam $\pm$ 0.0044 Jy/beam giving the ratio of 1. It is also seen from the figure that there are no other brighter sources in the KAT-7 field of view, the source is isolated. The properties of the sources listed above justifies the use of PKS1934-638 as a flux density and bandpass calibrator for our observations.

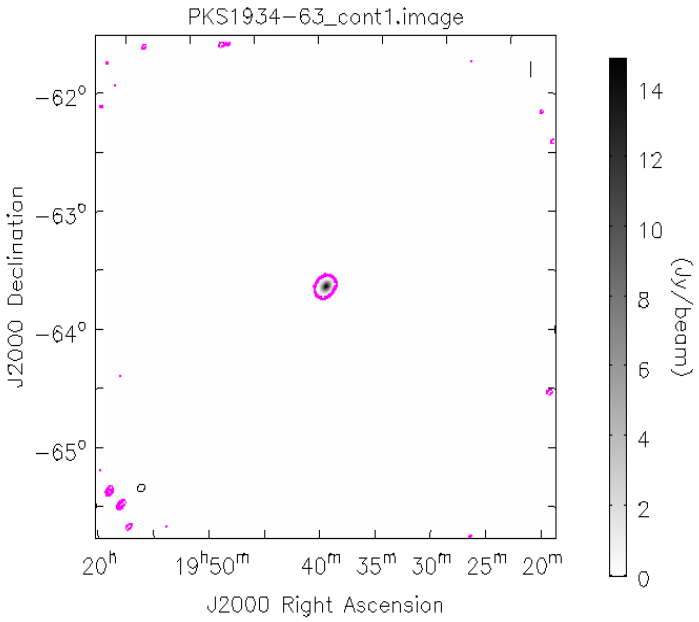

Figure 3.4: KAT-7 1.37 GHz radio image of PKS1934-63. The image has a peak brightness of 14.8 Jy/beam± 0.0044 Jy/beam with integrated flux density of 14.8 Jy ± 0.0044 Jy. The off source noise level in the image is 1.0 mJy/beam. The contours are drawn at [-3,3,6,12,20,24] × 1.0 mJy/beam. The synthesized beam is 270.6″× 211.9″ at a position of -46.8° as shown in the left bottom ellipse

- **PKS1421-490** is identified as a bright, flat spectrum radio source located at RA 14:24:32 and DEC -49:13:49, at a redshift of (z = 0.6631) (Ekers 1969). Very Long Baseline Interferometry (VLBI) revealed a 10 milli-arcsecond scale structure within the brightest component of this source (Preston et al. 1989). Studies at the Australian Telescope Compact Array (ATCA) later revealed significant radio emission on arc second scales extending south-west from the brightest component (Lovell 1997). For this reason, PKS1421-490 was included in a Chandra survey of flat spectrum radio quasars with arc second scale radio jets. The Australia Telescope National Facility has listed PKS1421-490 as one of the ATCA calibrators [8]. As shown in Figure 3.5, the source flux density shows a slight variation at 2100 MHz (red points) observed from 2008 to 2014 and almost constant flux density recorded 5500 MHz from 2004 to 2014 (light magenta points). To correct for the time varying part of the gains, PKS1421-490 was chosen as a phase calibrator for the target source PKS1318-43. The phase calibrator needs to be partially resolved and close to the target source. This is because when the gap between the phase calibrator and the target source is small, preferable $\geqslant 15°$, the phase perturbation caused by the atmosphere will be minimized significantly (Rohlfs and Wilson 2000). To check for the angular distance between PKS1421-490 and PKS1318-43, the following formulae was used,

$$cos(AD) = cos(d1) \times cos(d2) \times cos(ra1 - ra2) + sin(d1) \times (d2) \tag{3.8}$$

where $d1$ and $d2$ are the declination of the phase and the target source respectively and $ra1$ and $ra2$ are the right ascension of the phase and target source respectively. The angular distance between PKS1314-43 and PKS1421-490 was calculated to be 11.9 °. This shows that the distance between the two sources is considered acceptable for PKS1421-490 to be used as a phase calibrator source. The continuum image of

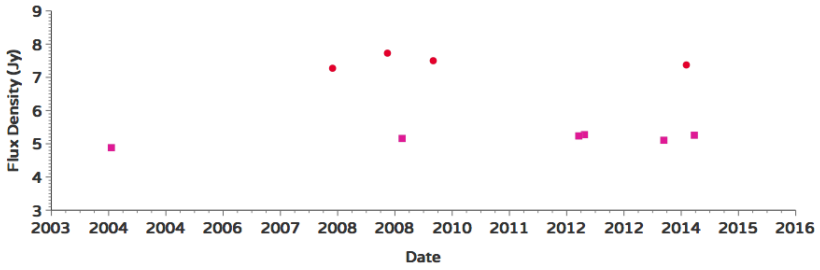

Figure 3.5: The plot of flux density vs time for PKS1421-490 from ATCA database at frequencies of 2100 MHz (red points) and 5500 MHz (light magenta points)[8]

PKS1421-490 obtained from the KAT-7 at a frequency of 1.40 GHz reveals that the source is unresolved with the integrated flux of 8.48 Jy ± 0.0063 Jy with peak brightness of 8.48 Jy/beam ± 0.0063 Jy/beam giving the ratio of 1.

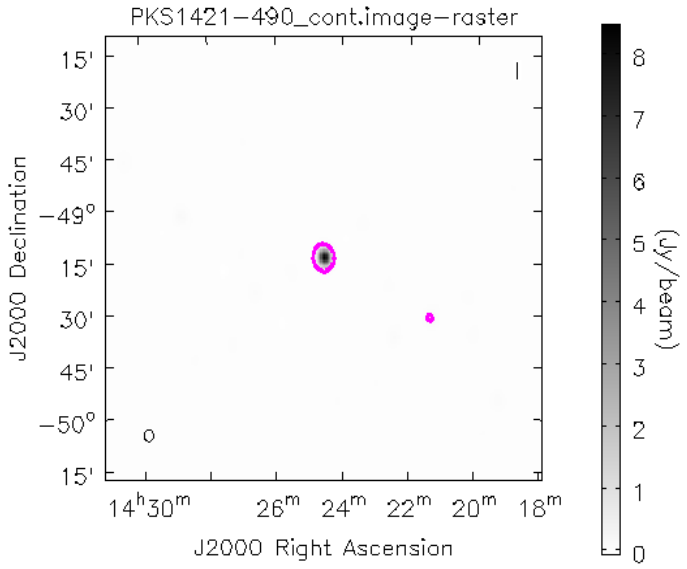

Figure 3.6: KAT-7 1.40 GHz radio image of PKS1421-490. The image has a peak brightness of 8.48Jy/beam ± 0.0063 Jy/beam with integrated flux density of 8.48 Jy ± 0.0063 Jy. The off source noise level in the image is 0.015 Jy/beam. The contours are drawn at [-3,3,6,12,20,24] × 0.015 Jy/beam. The synthesized beam is 209.0″× 159.5″ at a position of -175.7.4° as shown in the left bottom ellipse

- **PKS1730-13** has been identified as a low frequency quasi-stellar object (QSO) at a redshift of $z = 0.9020$ (Feng et al. 2006). The source coordinates are RA 17:33:02 and DEC -13:04:49. PKS1730-130 is variable at radio wavelength and is dominated by a compact core of 8.8 Jy at 8.387 GHz (Marscher and Broderick 1981). The source is listed as a ATCA calibrator [8]. As can be observed from Figure 3.6, its flux density measured at 2100 MHz (red points) slightly changed from $\sim$ 2.5 Jy in 2012 to 2.6 Jy in 2014. Regarding the flux densities measured at 5500 MHz between 2004 to 2014, there was a significant variation in flux density seen in light magenta points. Using Equation 3.8, the angular distance between PKS1717-00 and PKS1730-13 was calculated to be 11.9 °. This shows that the distance between the two source is considered acceptable for PKS1730-13 to be used as a phase calibrator for PKS1717-00. The KAT-7 continuum image of PKS1730-130, Figure 3.7 shows that the image is unresolved with the peak brightness of 4.51Jy/beam ± 0.0010 Jy/beam with integrated flux density of 4.51 Jy ± 0.0010 Jy/beam giving the flux to brightness ratio of of 1 at 1.37 GHz.

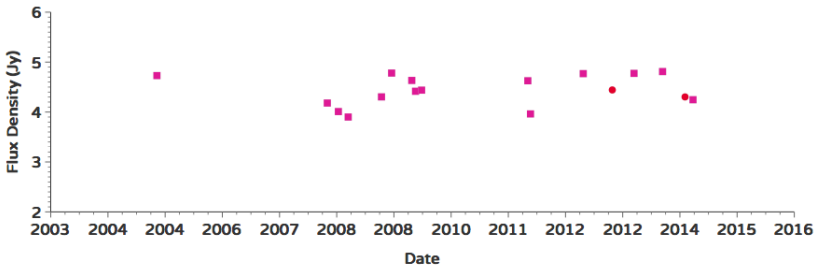

Figure 3.7: The plot of flux density vs time for PKS1730-130 from ATCA database at frequencies of 2100 MHz (red points) and 5500 MHz (light magenta points) [8]

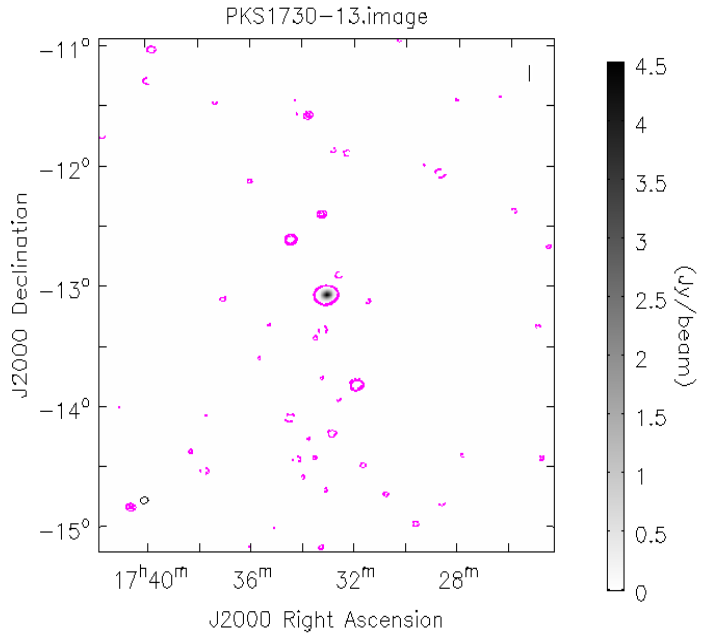

Figure 3.8: KAT-7 1.37 GHz radio image of PKS1730-13. The image has a peak brightness of 4.51 Jy/beam ± 0.0010 Jy/beam with integrated flux density of 4.51 Jy ± 0.0010 Jy. The off source noise level in the image is 0.6 mJy/beam. The contours are drawn at [-3,3,6,12,20,24] × 0.6 mJy/beam. The synthesized beam is 270.0″× 190″ at a position of 83° as shown in the left bottom ellipse

3.3 Observation

KAT-7 was used to observe the 4 radio sources for this study. Observations for each target were carried out separately. c16n25M4K correlator mode was used to observe all the sources. The observations were carried out using the total bandwidth of 25MHz, divided in 4096 channels each of channel width 6.104KHz, giving a velocity resolution of 1kms^{-1}. The correlator integration time was 10s. The correlator broad bandwidth provides a large velocity coverage with sufficient spectral resolution on both sides of the absorption features, this is important to obtain good subtraction of the continuum. The number of working antenna used was 7 with elevation of $>10^o$(anything below this elevation was discarded). This is because data taken at elevations below 10° are dominated by ground radiation (where radiation from the ground comes through the antenna sidelobes). In all our observations, except for PKS1549-79 and PKS1814-63, the phase calibrator was observed every 10 minutes. The receivers were tuned to the approximate redshifted wavelength of the HI 21-cm line ($z = (\nu_0 - \nu)/\nu$). Where z is the redshift of the source, ν_0 is the rest frequency of 21 cm HI line (1420.405752 MHz), and ν is the redshifted frequency of the absorption line. Details outlining observations carried out for each source are given below. Table 3.3 gives the summary of the observations for 4 radio sources observed with KAT-7.

PKS1318-43 The source was observed from 5 November 2013 to 23 November 2013 divided into 3 observation runs. The total time on the target ($T_{time} \approx 17$ hours). The bandpass/flux calibrator (B_{cal}) PKS1934-63 was observed at the beginning and end of the observation with the scan time ≈ 4.50min. The phase calibrator (G_{cal}) used was PKS1421-490 observed in between the source for the scan time ($G_{time} \approx 0.5$min). The center frequency (ν) for this observation was 1404.4 MHz.

PKS1549-79 The source was observed on 19 October 2013 from 09:38:31.6 to 11:16:31.2 universal time. PKS1934-63 was used for the flux density as well as bandpass calibration (B_{cal}). The bandpass calibrator was observed in between the target source for the scan time of ≈ 5 min using 6 scans. The target source was observed for ($T_{time} \approx 10$ min) scan time using the total of 6 scans. The center frequency (ν) for the observation was 1233.0 MHz.

PKS1717-00 The source was observed from 13 May 2014 to 20 May 2014 divided into 4 observing runs. The total time on target ($T_{time} \approx 17$ hrs). The flux/bandpass calibrator (B_{cal}) PKS1934-638 was observed at the beginning and end of the observation for ≈ 4.50 min each scan. The phase calibrator (G_{cal}) used was PKS1730-130, observed in between the target for the scan time ($G_{time} \approx 0.5$min). The center frequency (ν) was 1378.5 MHz.

PKS1814-63 The source was observed on 19th October 2013 from 08:31:38.6 to 09:38:26.6 universal time. The bandpass and flux calibrator, PKS1934-63 (B_{cal}) was observed in between the target observations. PKS1934-63 was observed for the scan duration of 5 min using 5 scans. The scan time on the target source ($T_{time} \approx 10$ min) observed for 4 scans. The center frequency for this observation was (ν) = 1334.1 MHz.

Table 3.3: Summary of observing parameters used to observe the sample used in this thesis.

Source	RA(J2000)	Dec1(J2000)	S(Jy)	dS(mJy)	z	centerν(MHz)	Observing time(hrs)	G_{cal}	B_{cal}
PKS1318-63	13:18:20	-43:26:00	0.27	8	0.0114	1404.4	17:00	PKS1421-490	PKS1934-63
PKS1549-79	15:56:58	-79:14:04	4.73	120	0.1522	1233.0	0.66	-	PKS1934-63
PKS1717-00	17:20:19	-00:58:24	0.09	10	0.0304	1378.5	17.00	PKS1730-130	PKS1934-63
PKS1814-63	18:19:34	-63:45:48	11.90	2280	0.0647	1334.1	0.66	-	PKS1934-63

Chapter 4

The KAT-7 Radio Data Reduction

The output of the correlated signal from each pair of antennas is a complex number called the *observed visibility*. This gives information of the amplitude and phase of the signal received. However, the observed visibilities will differ from the true visibilities due to multiple reasons such as phase irregularities in the wavefront of incoming radio waves caused by irregularities in the ionosphere and phase distortion during signal processing. Estimating these effects and correcting the observed visibilities to obtain the true visibilities is called *calibration*. Editing or flagging refers to the process of excluding data that is severely corrupted. This can be due to instrumental problem, bad weather, interference from man-made sources etc. Generally all radio interferometric observations will require some flagging. The process of *editing* and *calibrating* the visibilities is known as *data reduction*. The data reduction process in this thesis was exclusively carried out using Common Astronomy Software Application (CASA) version 4.1.0. In this chapter, we outline the general data reduction process used for the observations presented in this thesis.

4.1 Data Format

The raw data from the KAT-7 are initially stored and tabulated in Hierarchical Data Format (HDF5) archive file by in-house software. The HDF5 archive file is then converted to a Measurement Set (MS) using a python script *H5toms*. The measurement set defines the format in which visibilities are stored and readable in CASA. The measurement set holds necessary information about the sources, polarization, antennas, frequency of observation, and others.

4.2 Data editing and flagging

Before calibration can begin, it is necessary to remove any data which is badly corrupted such that including it in any calibration or analysis would do nothing but degrade the final result. The data may be bad due to radio frequency interference (RFI), poor atmospheric conditions, instrumental malfunctions etc. Such data will hinder the determination of the true antenna gains, and will prevent accurate calibration and scientific results. In CASA, the process of identifying and deleting corrupted data is known as *editing* and $flagging$. In general, the flux calibrator, phase calibrator and target where each examined separately for bad antenna, baselines and time ranges. In particular, the CASA task $flagdata$ was used to remove bad data. The manual mode for this task allowed us to flag bad data by frequency, time period, polarization, or antenna. To begin with, data at elevations lower than 10° were flagged out. Such data is mostly considered to be noisy and unreliable due to ground radiation entering the sidelobes. At this stage, bad data caused by shadowing were also flagged out. Shadowing happens when radiation entering one antenna is blocked by another nearby antenna (mostly common on short baselines). Data affected by shadowing were deleted by specifying the input ($mode = shadowing$) in $flagdata$.

To further identify bad visibilities, we used the *plotms* graphical user interface (GUI) in CASA. Data for all 21 baselines, both polarizations (XX,YY) for the bandpass/flux calibrator were examined. Combination of inputs such as colorize and plot-axis (channel or time) allowed for easy and thorough searches for corrupted data in CASA which are usually identified by their highly scattered amplitudes in the sampled data and unexpected phase variations. Using the display-colorize feature, *plotms* was able to display a third dimension of the data on a 2D plot. For example, Figure 4.1 shows the plot of amplitude versus channel for the phase calibrator PKS1730-13, baselines antenna 4 and antenna 6, and using the input colorize to represent two polarizations XX and YY. It is clear from Figure 4.1 that there was significant RFI between channel 800$\sim$ 1300. RFI is this region was identified by the unusual high amplitudes in the visibilities reaching up to 1. Having this information, the channels with RFI were flagged out in manual mode using $flagdata$.

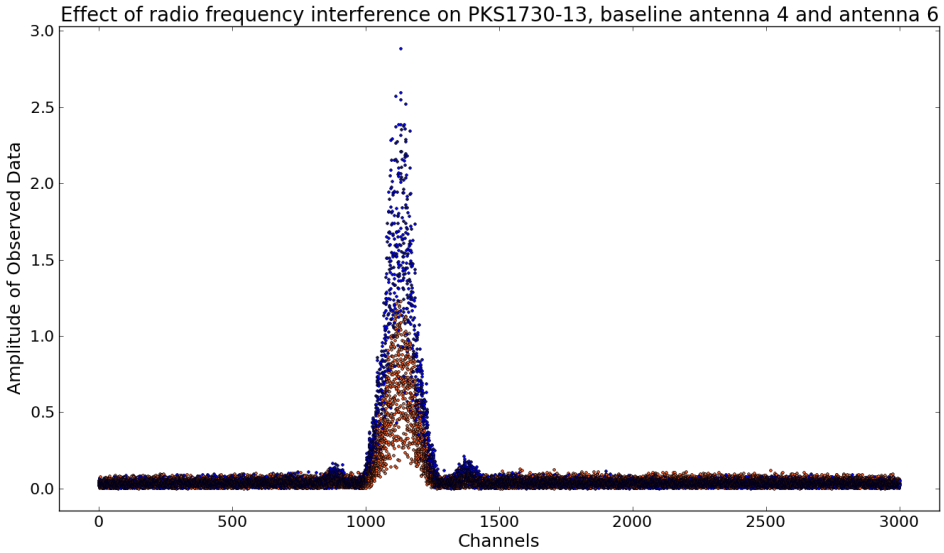

Figure 4.1: Sample display of uncalibrated and unedited data using *plotms* GUI application in CASA. Shown is the visibility amplitude as a function of channel for PKS1730-13, baseline antenna 4 and antenna 6 during 12-13 May 2014 observation. The different colours in the plot represent the two polarizations (XX,YY). The RFI in this baseline is identified as high amplitude visibilities between channel 800 $\sim$ 1300.

4.3 Delay calibration

At the start of each observation, the antenna configuration results in geometrical and instrumental delays which causes the signal from the source to arrive at different times for different baselines. This delay is usually corrected by inserting an equivalent delay in the system which requires knowing the accurate position of the antennas. Uncertainties in determining the accurate position of each antenna causes a delay which puts a phase ramp versus frequency channel in the data. These delays were corrected using *delay calibration*. To carry out delay calibration, a point source of at least moderate brightness ($S \geqslant 1Jy$) is required. This is so, in order that the correlator can accurately determine the phase slope with frequency as the accuracy improves with signal to noise. In this case, the flux calibrator PKS1934-638 was used for delay calibration. This is because PKS1934-638 was one of the strongest source observed for all our observations. For KAT-7, the delay between the received signals should be less than 5.12 ns. Using the CASA task *gaincal*, the delays were solved by using ($gaintype = K$) as the input parameter in *gaincal* and setting antenna 5 as a reference antenna. Figure 4.4 shows the solutions for the delay calibration for one of the observations used in this thesis, for the YY correlation. The delays for the XX correlation were also solved.

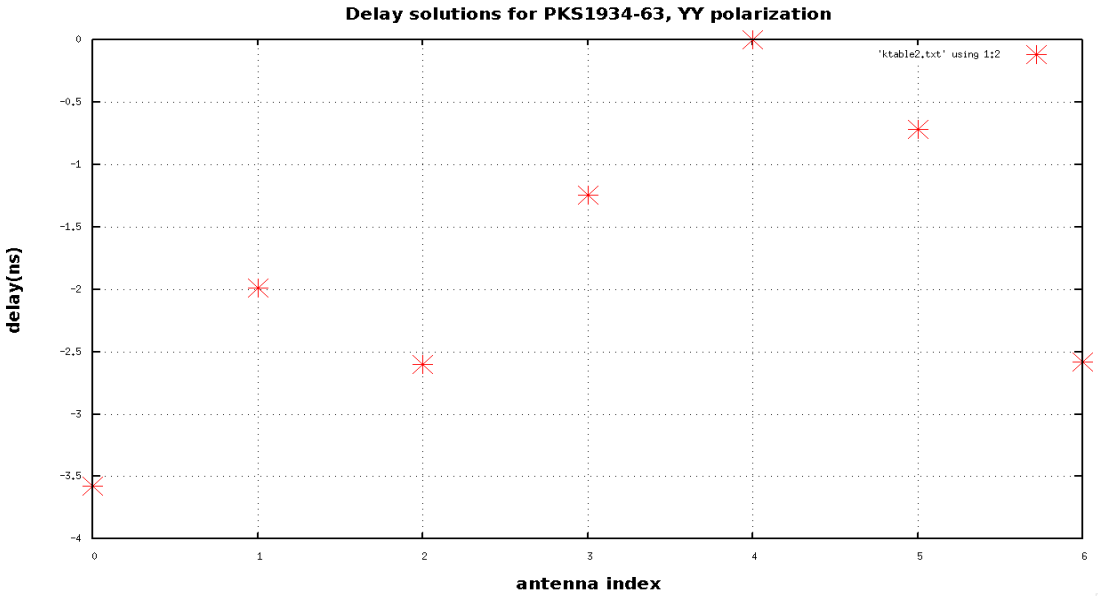

Figure 4.2: The delay calibration for PKS1934-638 for the 19-May 2014 observation, YY correlation. The y-axis represents the time delay(ns) for each antenna while the x-axis represents the antenna index, where 0 represents antenna 1, 1 represents antenna 2 and so on. Using antenna 5 as the reference antenna, the delays of $\sim$ 3.5 ns occured for antenna 1, $\sim$ 1.9 ns for antenna 2, $\sim$ 0.7 ns for antenna 6 and $\sim$ 2.5 ns for antenna 7.

4.4 Flux density Scale

After correcting for the delays, the next step was to set the proper flux density of the flux calibrator which is initially set to 1 in the measurement set. This was done using the CASA task *setjy*. The *setjy* task places the model visibilities amplitudes and phase associated with a specified clean components image into the model column of the data set at a specified observing frequency. For all the observations used in this thesis, PKS1934-638 was used for flux calibration. As explained in chapter 3, the flux density of PKS1934-638 has been observed to be less variable and the source is easily observable in the southern hemisphere making it a suitable choose for flux calibration. Important input parameters in *setjy* included the $field$, specifying the flux calibrator and $standard = Perley-Taylor$ 99, to set the flux density model used to derive the flux density. Using the *setjy*, the flux density of PKS1934-638 at 1334 MHz was found to be 15.01 Jy. To compare the flux density derived from the model in CASA to the expected flux density of the source at the observing frequency, we used the polynomial relation between flux density of the source at a specific observing frequency (Sault 2003). The polynomial relation used is based on measurements between 408 MHz and 8640 MHz obtained from Sault (2003)

$$log_{10}(S) = -30.7667 + 26.4308x - 7.0977x^2 + 0.605334x^3 \tag{4.1}$$

where $x = log_{10}(\nu)$ and ν is the observing frequency in MHz. Using Equation 4.1 the expected flux density of PKS1934-638 at 1334 MHz was found to be 14.99 Jy which gives an error of 0.13 % at the observing frequency.

4.5 Bandpass calibration

The antenna based complex gains vary across the passband due to the antenna band shape. These variations in the complex gains must be corrected before the visibilities from individual channels are averaged. To correct for the variations in the passband, we used *bandpass calibration*. Bandpass calibration requires the use of a calibrator point source that is strong ($S > 1Jy$), with line free continuum in order to find bandpass characteristics for each antenna receiver combination. In all the observations in this thesis, the flux calibrator PKS1934-638 also served as the bandpass calibrator. This is because the source is strong (∼16.4 Jy at 21 cm [9]) and has been observed to have a fairly stable flat spectrum [8]. While amplitude variations have very little effect on the data, it is important to first solve for any phase variations with time to ensure that decorrelation does not occur when it is time to average the data while computing the bandpass solutions. To correct for the phase variations, we carried out a temporal phase calibration using the CASA task *gaincal* on a small portion of the band. In this case we used the channels in the middle of the band from 1000 to 2000 which were free from RFI. Although we obtained solutions only for a few channels, these solutions were applicable to the entire band.
Using the bandpass calibrator, bandpass solutions were obtained using the CASA task *bandpass*. The task *bandpass* builds a table with the amplitude and phase as a function of frequency for the spectral window. The solutions from the initial phase calibration were used as input in the task *bandpass*. Typically, solutions were near unity for the central channels and decreased near the edges as shown in Figure 4.3. Figure 4.3 shows that the gain amplitudes of each antenna vary less than 10% across the channels and such variations are acceptable.

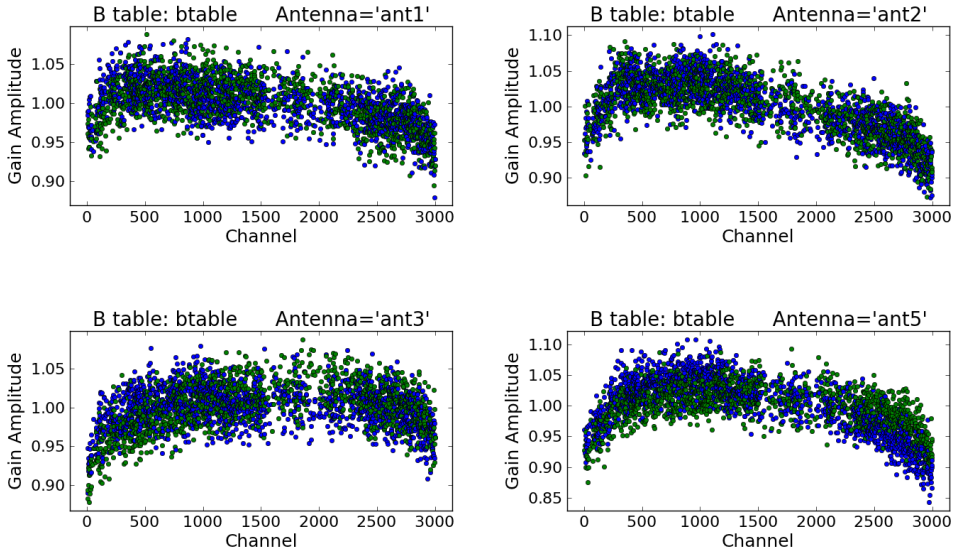

Figure 4.3: Bandpass solution for PKS1934-638 obtained from the observation carried out on 19/05/14 for antennas 1,2,3 and 5. The variations in the gain amplitude for each antenna are seen to be less than 10% which is an acceptable range. Different colours present different correlations(XX,YY).

4.6 Gain calibration

Once we had accounted for the possible variations in gain between different scans of the bandpass calibrator, it was necessary to solve for any corrections to the phase and amplitude gain variations between antennas, these are the complex antenna gains ($G(t)$). To correct for the phase and amplitude gains, we took into consideration a phase calibrator that was very close to the target to help minimize differences in the atmosphere between the lines of sight of the phase calibrator and the target sources. Using CASA task *gaincal*, we determined the gain amplitudes and phases for each antenna with reference to the predetermined reference antenna for which the phase is defined to be zero. The reference antenna is usually chosen to be one at the center of the configuration, in this case antenna 5 was used. The gains were obtained for a specified solution interval by specifying the input parameters $solint = inf$, to describe the solution interval from arbitrary value up to the scan boundary, $gaintype = G$, describing the time-dependent gain and $calmode = ap$, indicating the solutions for amplitude and phase.

4.7 Fluxscale

After running *gaincal* on standard flux density calibrator and phase calibrator, the CASA task $fluxscale$ was used to determine the phase calibrator flux density. The task

fluxscale applies the constraint that the net system gain was, in fact, independent of field, on average, and that field dependent gains in the input tables are a result of the unknown flux densities of the calibrators. The average ratio of the gains of the flux and phase calibrator over all antennas and polarizations yields a correction factor that was applied to the secondary calibrator (phase calibrator) to set the flux density of the phase calibrator. After running *fluxscale*, the flux density of 4.51 +/- 0.008 Jy was derived for PKS1730-130 at 1378 MHz. To confirm if the obtained flux density was consistent with the expected flux density of the source at the observing frequency (1378 MHz), the following formula was used.

$$S_2 = S_1(\frac{\nu_2}{\nu_1})^{\alpha} \tag{4.2}$$

where S_2 is the expected flux density at 1378 MHz, S_1 is the flux density at 1465 MHz (4.45 Jy) and α is the corresponding spectral index of the source at 1465 MHz($\alpha = -0.13$). The values of α and the flux density at 1465 MHz were obtained from the astronomical catalogues and large surveys VizieR [11]. Using Equation 4.2, the expected flux density of PKS1730-13 at 1378 MHz was found to be 4.48 Jy which gives the percentage difference of 1.3% compared to the value derived from *fluxscale*.

4.8 Applycal

Once the calibration was completed, the corrected amplitude and phase solutions were applied to the target source. However, to check if the calibration was properly carried out, we first applied the solutions to the calibrator source itself. For point source calibrators, the amplitude of the calibrated visibilities are expected to be equal to the flux density of the source, (Jy) and the corrected phase solutions are expected to be at the phase center, zero. Figure 4.4 shows a plot of corrected visibilities of amplitude vs phase for one of the observation for the flux/bandpass calibrator where the data lies at the phase center with the amplitude corresponding the the source flux density (Jy). This procedure was checked for all other observations before applying the solutions to the science source. After checking the calibration solutions and successfully applying them to the target source, the next step was to split the corrected data for the target sources to a different measurement set in order to analyze them separately. This was done using the CASA task *split* and specifying the file name in the input parameters under *outputvis*.

[11] http://vizier.u-strasbg.fr/viz-bin/VizieR

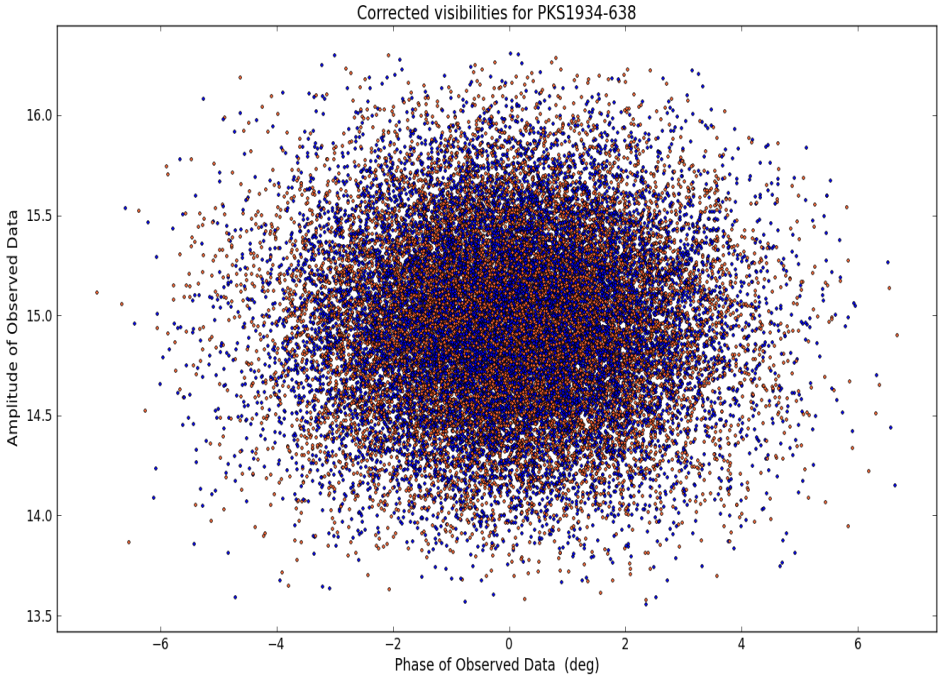

Figure 4.4: Corrected amplitude and phase solutions of the bandpass/flux calibrator, PKS1934-638 observed on 13 May 2014. The phase solutions are seen to be at the phase center with the amplitude corresponding to the flux of the source at 1378 MHz.

Doppler correction Spectral line observations provide information about kinematics of the gas/objects observed. It is therefore essential to correct for the reference frames being used in the observation in order to obtain correct velocities for the spectral lines being studied. KAT-7 does not use doppler tracking meaning that we had to manually correct for this before imaging the data. The first step was to open the $SPECTRAL\ WINDOW\ TABLE$ in the measurement set and change the reference frequency to 1420.405752 MHz (since we are looking at HI 21-cm line). The task *cvel* was then used to obtain a doppler corrected measurement set. This was done by specifying the new reference frequency and setting the output frame to optical, baryocentric in the *cvel* input parameters. The next step after Doppler correction was to image the sources.

4.9 Initial imaging

Corrected visibilities represent the intensity distribution convolved with the point spread function. This represents the true image convolved with unwanted responses in the data such as sidelobes. In order to obtain the true image from the visibilities, two processes were carried out: Fourier transform of the visibilities and then deconvolution. These processes are explained in details in Section 2.10. Using the $CLEAN$ algorithm developed by Högbom, which assumes that the radio sky can be represented by a small number of points sources in an otherwise empty field of view, the continuum images were produced using line free channels. Some parameters used in *clean* include : $mode = mfs$, which produces one images from all the selected channels, the cell size and image size were derived using Equation 2.34 and 2.35 given the observing frequency for each source, the diameter of each telescope, and the total maximum baseline used for each observations, in this case all the images where obtained by using the image size of 512 $\times$ 512 with the cell size of 30 $\times$ 30 arcsec. The cleaning threshold was set to 3 times the expected root mean square (rms) noise. The expected noise for each source was derived from the radiometer equation as defined in section 3, Equation 3.7. For PKS1814-63, the expected rms noise of 0.5mJy was derived from the total integration time of 40 minutes, total bandwidth of 18.3 MHz, and the total number of 7 antennas used for the observation. All the images were cleaned using 5000 iterations by setting $niter = 5000$ as input in *clean*. To obtain images with reduced rms and improved dynamic range, each source was imaged by using the *natural* weighting by setting the parameter $weighting = natural$ in *clean*. The *natural* weighting reduces the noise level in the cube, thereby improving the dynamic range of the image. Details on weighting is given in Section 2.12. After running *clean*, the image rms and flux density were derived for each source.

4.10 Self calibration

After the initial imaging of the continuum sources, the rms in the images were higher than expected and the flux densities of the sources were lower than the expected values. To correct for this, we carried out self calibration. Details on self calibration are given in Section 2. Self calibration uses the target model to improve on the complex gains which were not corrected during the initial calibration. This was done by using the model image and passing it to the next calibration cycle on the target data until the desired imaged is produced. For each round of self calibration, the rms was expected to reduce while the flux density of the source was expected to increase. Self calibration was stopped when the rms in the images stabilized. To carry out self calibration a CASA task *gaincal* was used. Parameters in *gaincal* included: $calmode = p$, specifying the solution type(in this case phase only), $solint = 5$ min, which gives the solution intervals for phase solutions, $gaintype = G$, which gives the time dependent gains. The minimum signal to noise was set to 3. For each round of self calibration, the phase solutions were examined. Figure 4.6 and 4.7 shows the time dependent gains for PKS1717-00 derived from the first and second round of self calibration. From the two figures, it is observed that the phase solutions improved in the second round of self calibration as they are seen to be at the phase center. After self calibration, the continuum was then subtracted from the visibilities data using the CASA task *uvcontsub*. This task estimates the continuum by fitting a polynomial to real and imaginary parts of the channel selected by $fitspw$. The fit represents a model of the continuum in all channels. For continuum subtraction, we used a polynomial fit of 1 by setting the input parameter $fitorder = 1$ in *uvcontsub*. Two different measurement sets were obtained after *uvcontsub*, one containing the continuum data and the other containing the spectral line data.

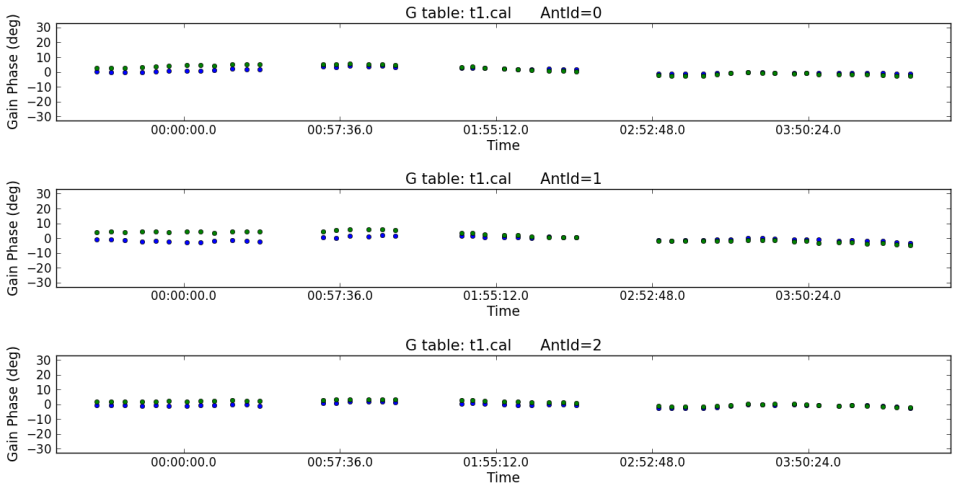

Figure 4.5: Phase solutions for PKS1717-00 after the first round of self calibration for antenna 1, antenna 2 and antenna 3. The x-axis represents the time and the y-axis represents the phases. The different colors in the figure represent the different polarization (XX,YY). The phase solutions for other antennas where also investigated before being applied to the visibilities.

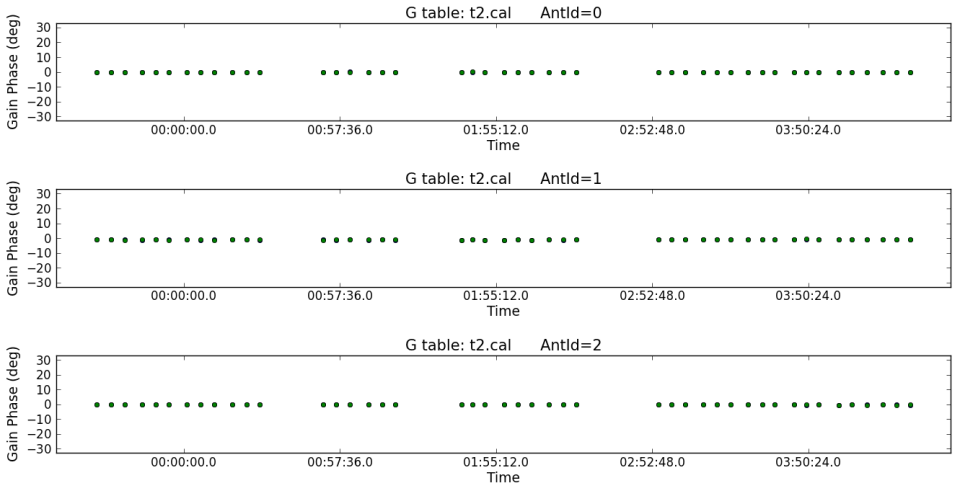

Figure 4.6: Phase solutions for PKS1717-00 after second round of self calibration for antenna 1, antenna 2 and antenna 3. The solutions, as expected for the corrected phases are seen to lie at the phase center, zero for all the antennas. The phase solutions for other antennas where also investigated before being applied to the visibilities.

4.11 concat

The last section in the data reduction process was to combine the measurement set for sources with more than one observing run. This was done using the CASA task *concat*. The *concat* task takes multiple measurement set inputs and combines them into one data set. Parameters in *concat* included: *concatvis*, specifying the output of the combined dataset, *visweightscale*, this provides the scaling factors to be added to the individual measurement sets. The task *visweightscale* is used because each data set has a slightly different flux density derived after calibration. For example, PKS1717-00 was observed for 3 observation runs and after the final round of self calibration, the source flux densities for each measurement set were measured to be 54.7 Jy, 55.0 Jy, and 55.6 Jy. To obtain the correct scaling factors, the flux densities were each divided by 54.7 Jy giving the scaling of $visweightscale = [1, 1.005, 1.016]$. Using the combined dataset, the final spectral and continuum images were imaged. For continuum imaging, we implemented the same parameters used in the initial imaging while for spectral line imaging, we used $mode = channel$ in *clean*.

Chapter 5

Results and discussion

In this section, we present the analysis of the reduced data and discuss the results for each of the sources in our sample. For the 2 sources where the observations were affected by RFI, we conduct tests to confirm the RFI sources. For the remaining 2 sources, we calculate the flux density from the continuum images and compare it with the expected flux density of the source at the observing frequency. For the detected 21-cm absorption line, we measure the optical depth, column density and the equivalent line width and compare the results with the literature. In the case where the line was not detected we measure the upper optical depth limit ($\tau_{3\sigma}$) and use it to derive the HI column density upper limit. We then go on to measure the sensitivity and spectral dynamic range achieved in each observation. Sensitivity determines the faintest signal the telescope can detect. When observing a point source, the image sensitivity will be the combined sensitivity of all interferometer combinations integrated over the full time on target. This will determine the weakest feature that can be detected in the image. Spectral dynamic range is defined as the ratio of the peak continuum flux to the rms in the continuum subtracted cube. Spectral dynamic range is vital for detecting faint lines superimposed on a strong continuum source. This is because the separation between the line and the continuum is very small and requires careful measures when subtracting the spectrum from the continuum. All measures collected and used for the analysis in this section are summarized in Table 5.2.

5.1 PKS1318-43

The observations for PKS1318-43 were divided into 3 observation runs in order to obtain a total integration time of 17 hours. However, only one file with a total observing time of 4 hours was not affected by solar interference. It was therefore not possible to reduce and analyze the source further because the observation of 4 hours does not produce the sufficient signal to noise required to detect the expected 21-cm absorption line in

PKS1318-43. The effect of solar interference is usually observed as ripples in the data due to the phase difference in the received signal from the sun and that of the source being observed. To verify the effect of solar interference on PKS1318-43, we have used data for the phase calibrator PKS1421-490. Figure 5.1 to 5.3 show some of the baselines for different scans affected by solar interference.

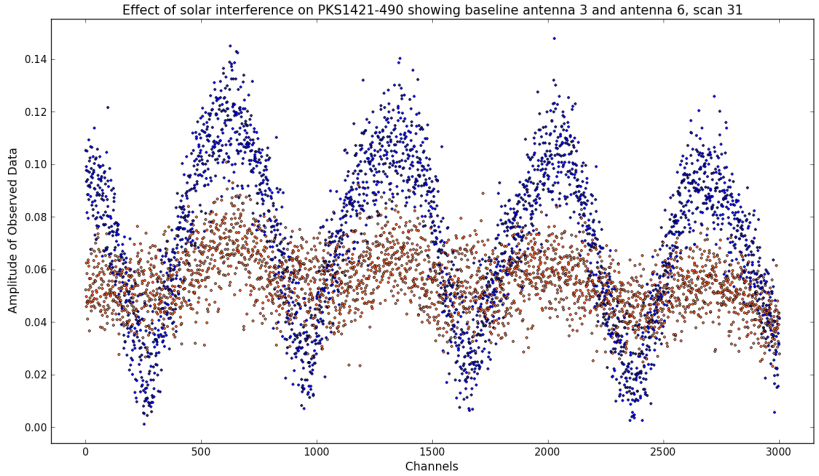

Figure 5.1: Effect of solar interference on PKS1421-490 baseline antenna 3 and antenna 6, scan 31. The different colours in the plot represent different polarizations

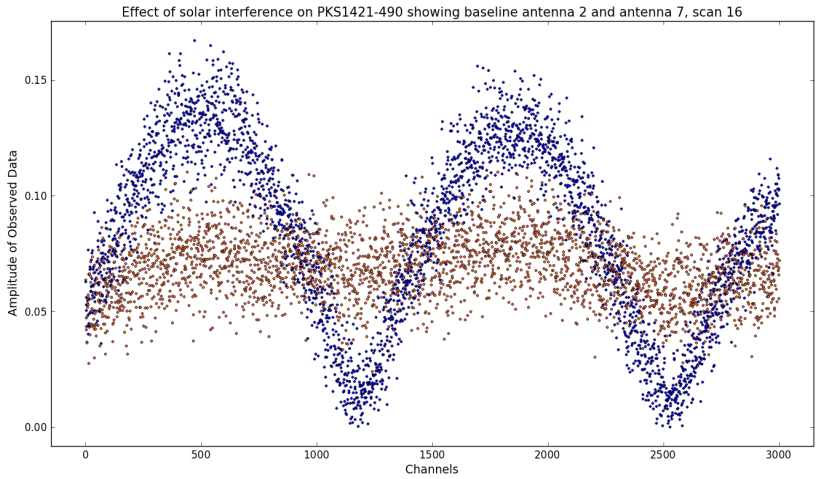

Figure 5.2: Effect of solar interference on PKS1421-490 baseline antenna 2 and antenna 7, scan 16. The different colours in the plot represent different polarizations

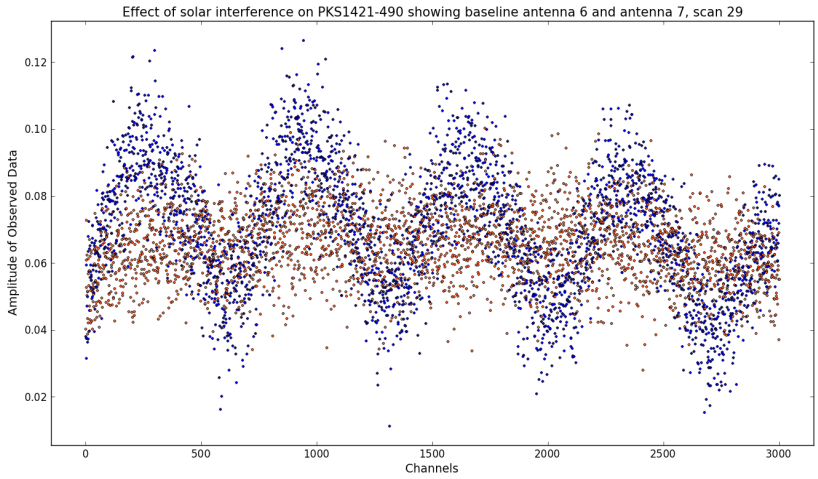

Figure 5.3: Effect of solar interference on PKS1421-490 baseline antenna 6 and antenna 7, scan 29. The different colours in the plot represent different polarizations

The ripples shown in Figures 5.1 to 5.3 tend to be more prominent in one polarization. This is because KAT-7 has two different dipoles which receive power differently. KAT-7 operates with one vertical and one horizontal linearly polarized dipoles. The other reason we see ripples in one polarization is because the effect of solar interference is coming from the sidelobes and not the central beam. The central beam is usually symmetric and the radiation received from both polarization is almost the same. However, the sidelobes tend to be highly polarized resulting in a difference in radiation patterns received by the two polarizations. In order to establish that the ripples observed are indeed due to solar interference, data was presented in terms of waterfall plots as shown in Figure 5.4. The ripples in Figure 5.4 are visibly seen in most baselines. The next step was to compare the observed ripples in each baseline with the calculated solar ripples at that time. The expected solar ripples are plotted as contours on the observed ripples. For data affected by solar interference, we expect the calculated ripples and the observed ripples to vary in the same way as a function of both time and frequency. Figures 5.5-5.8 show some of the examples of the observed amplitudes and phase with the corresponding calculated solar ripples at that time. The Figures show that the variations in the observed amplitudes and phases are the same as the expected solar ripples. This verifies the presence of solar interference in this dataset.

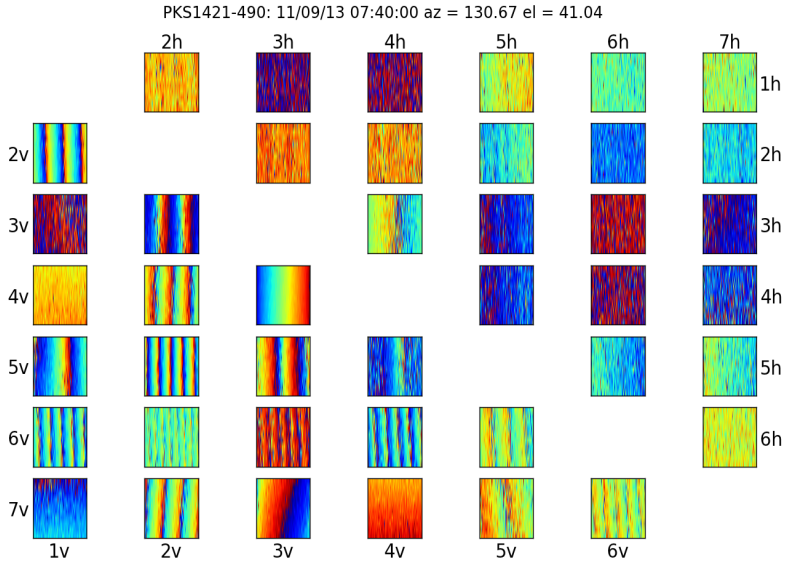

Figure 5.4: Waterfall plots showing the ripples in PKS1421-490. The plot represents one scan with all baselines. The different letters represent different polarizations while the square boxes represent different different baselines.

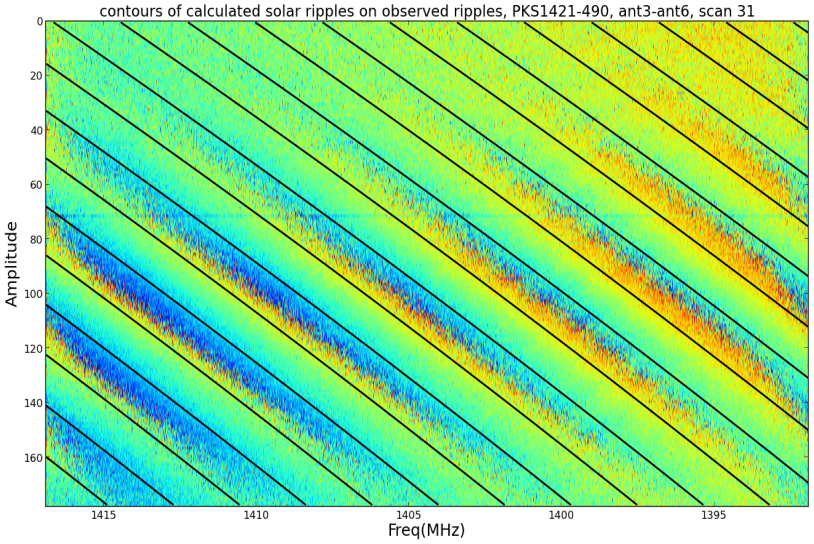

Figure 5.5: A plot of observed ripples and calculated solar ripples for PKS1421-490, antenna 3-antenna 6, scan 31. The calculated ripples are plotted as contours on the observed ripples. The x-axis represents the frequency in MHz while the y-axis represents the amplitude. The observed and calculated ripples compare favourably.

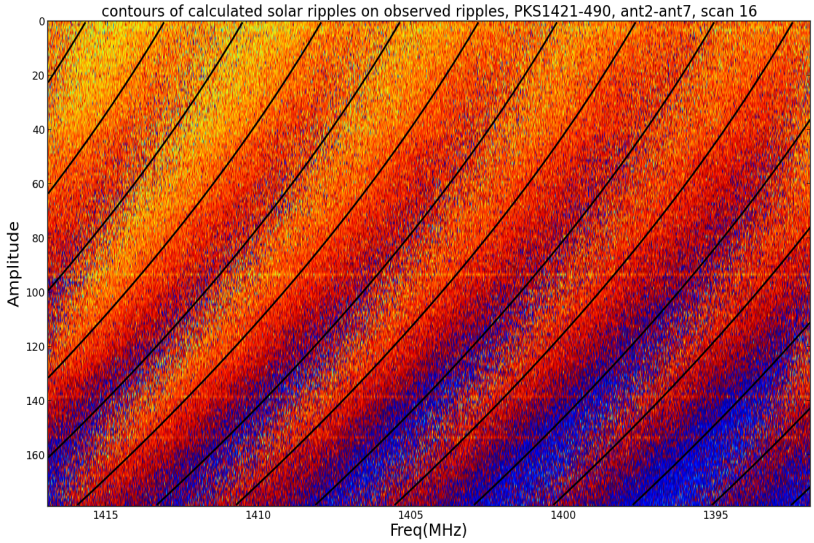

Figure 5.6: A plot of observed ripples and calculated solar ripples for PKS1421-490, antenna 2-antenna 7, scan 16. The calculated ripples are plotted as contours on the observed ripples. The x-axis represents the frequency in MHz while the y-axis represents the amplitude. The observed and calculated ripples compare favourably.

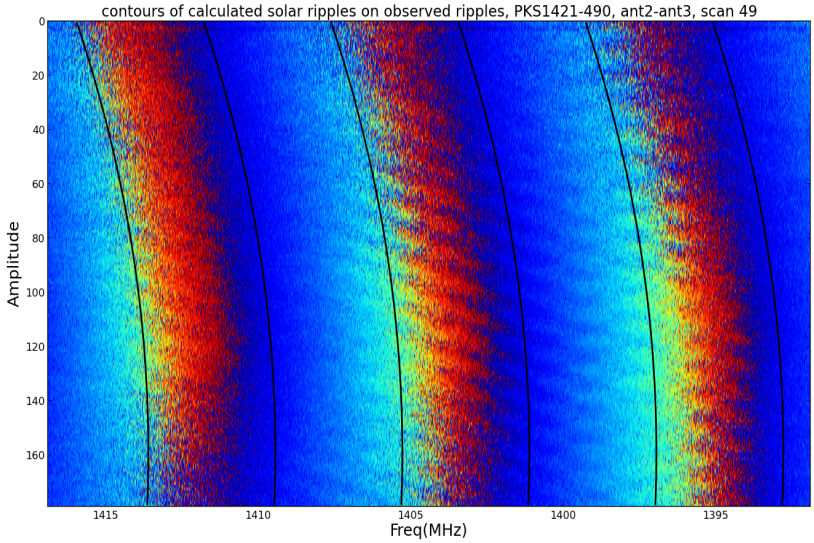

Figure 5.7: A plot of observed ripples and calculated solar ripples for PKS1421-490, antenna 2-antenna 3, scan 49. The calculated ripples are plotted as contours on the observed ripples.The x-axis represents the frequency in MHz while the y-axis represents the amplitude. The observed and calculated ripples compare favourably, however, there appears to be a secondary effect in this scan. This appears as a high frequency ripple with a different delay.

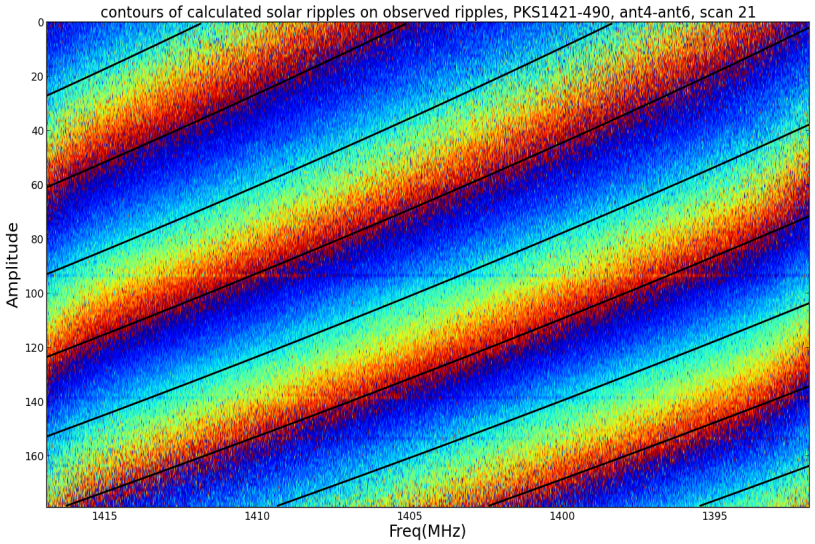

Figure 5.8: A plot of observed ripples and calculated solar ripples for PKS1421-490, antenna 4-antenna 6, scan 21. The calculated ripples are plotted as contours on the observed ripples. The x-axis represents frequency in MHz and the y-axis represents the amplitude. The observed and calculated ripples compare favourably.

5.2 PKS1549-79

The source was observed in the frequency band 1225-1245 MHz. From figure 5.9 it is evident that there is a large feature at around 1227 MHz. This corresponds to the L_2 band in which GPS satellites broadcast continuously [12]. This strong signal induces artifacts in the bandpass, such as ringing and gain compression, which destroys the signal from the source. This means that we were unfortunately not able to use this dataset.

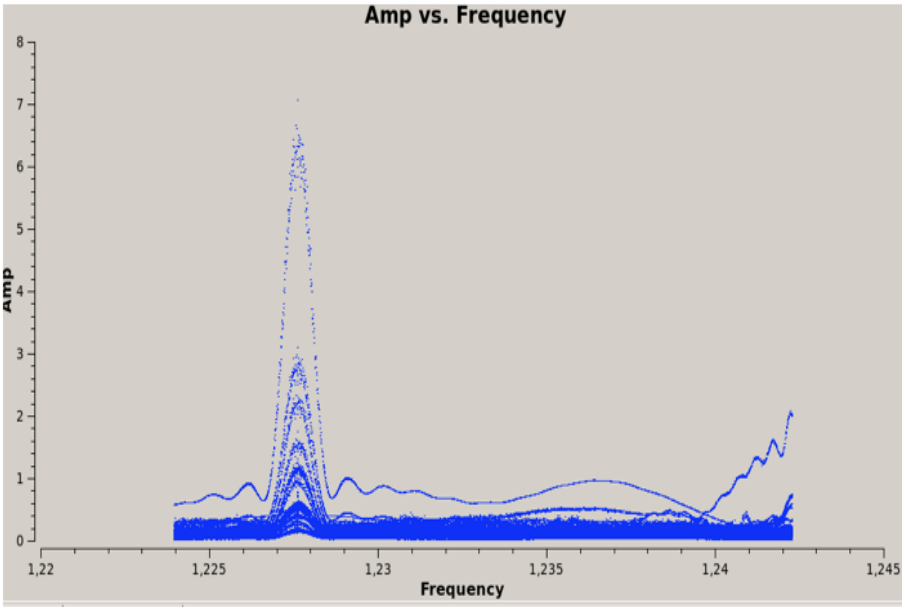

Figure 5.9: Effects of satellite interference on PKS1549-79, XX correlation. The y-axis represents the amplitude and the x-axis represents the frequency in MHz. Satellite interference is seen around 1227.6 MHz, which is the L_2 band in which all GPS systems transmit.

5.3 PKS1814-63

The aim of the first part of the analysis was to determine the flux density of the source from the continuum image. The flux density of the source was derived from the image obtained after self calibration, imaged with line free channels. The continuum image of PKS1814-63 is shown in Figure 5.10. The flux density was derived using the CASA task $imfit$. The $imfit$ task is used to fit one or more gaussians to the source in an image. The input parameters for $imfit$ include; $imagename$, which specifies the image to be fitted, box, which specifies the region of the image to be fitted. After running $imfit$, the integrated flux density, S of the source was found to be 13.03 Jy $\pm$ 0.021 Jy with the peak brightness (S_{peak}) of 12.97 Jy/beam $\pm$ 0.021 Jy/beam. The values of the

[12] http://www.mio.com/technology-gps-signal.htm

integrated flux density and peak brightness show that the source is compact, unresolved at KAT-7 angular resolution. The ratio between the peak brightness and flux density is calculated to be ~ 1. To compare the derived flux density of the source with the

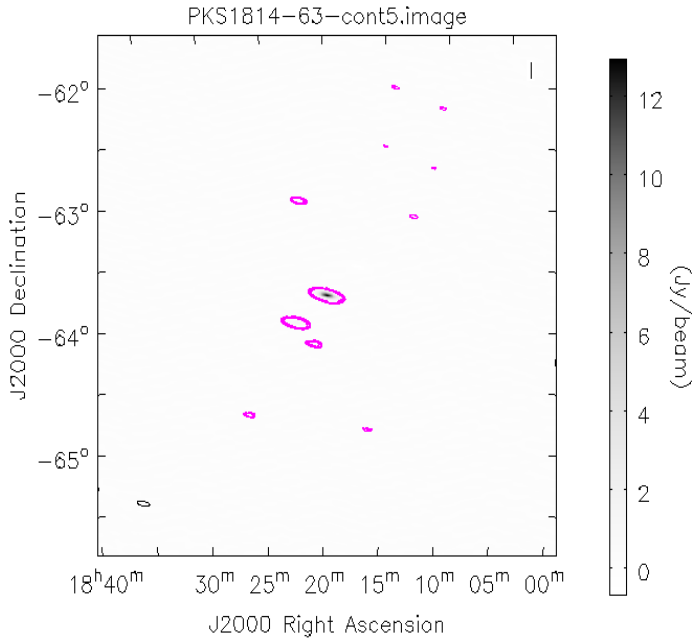

Figure 5.10: KAT-7 1.33 GHz radio image of PKS1814-63. The image has a peak brightness of 12.97 Jy/beam ± 0.021 Jy/beam with integrated flux density of 13.03 Jy ± 0.021 Jy. The off-source noise level in the image is 2 mJy/beam. The contours are drawn at [-3,3,6,12,20,24] × 2 mJy/beam. The synthesized beam is 424.9″× 137.2″ at a position of 79.4°

expected flux density at the observing frequency 1334 MHz, the following formula was used

$$S_2 = S_1(\frac{\nu_2}{\nu_1})^{\alpha} \tag{5.1}$$

where S_2 is the expected flux density of PKS1814-63 at 1334 MHz, S_1 is the flux density of the source at a particular frequency ν_1. The values of S_1 and ν_1 were selected on the basis that there was a corresponding spectral index α available at ν_1. These values were obtained from the astronomical catalogues and large surveys, VizieR database [11]. At 2700 MHz, the flux density of PKS1814-63 is 7.4 Jy and has the spectral index of -0.85, substituting these values in Equation 5.1, the expected flux density of PKS1814-63 at 1334 MHz is 13.4 Jy. The expected value differs from the flux density derived from $imfit$ by

$$\% = |S_{\text{measured}} - S_{\text{expected}}|/S_{\text{expected}} \tag{5.2}$$

[11] http://vizier.u-strasbg.fr/viz-bin/VizieR

The % difference of 0.7 is obtained.

Using the continuum subtracted spectral line cube, the spectral line profile was extracted at the pixel corresponding to the source location. We detected HI 21-cm absorption line towards PKS1814-63 using the KAT-7 telescope as shown in Figure 5.11. The line profile was detected at a systematic velocity of 19178 kms^{-1} corresponding to the redshift of 0.063. The HI 21-cm absorption line in this source was previously detected by Véron-Cetty et al. (2000) and Morganti et al. (2011). As shown in Figure 5.11, the absorption profile is deep, with the line depth of $\Delta S = 2.53$ Jy/beam. The absorption

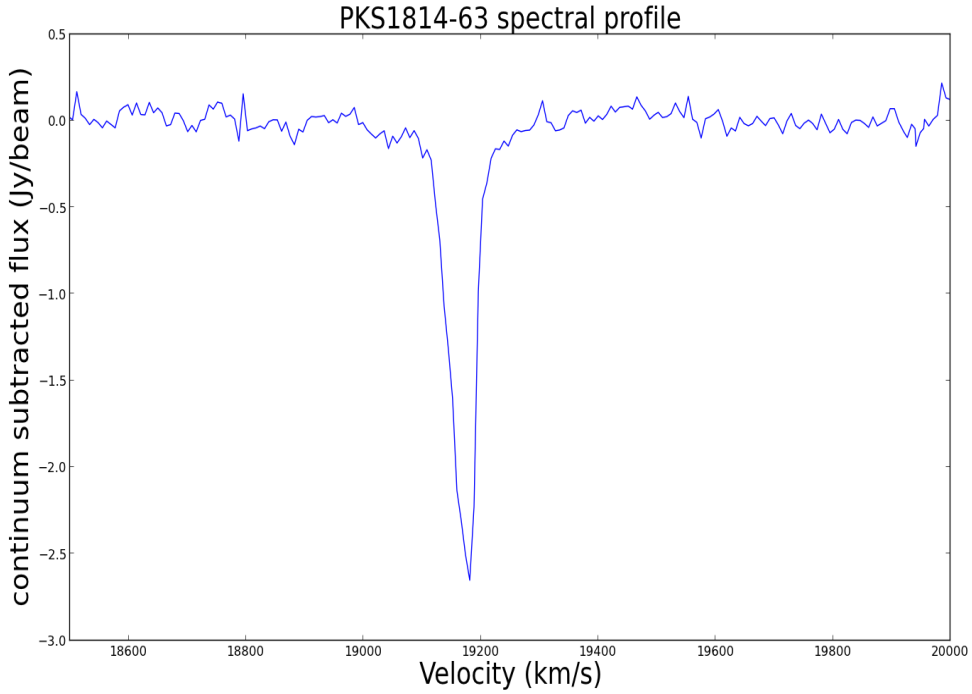

Figure 5.11: KAT-7 spectra of detected HI 21-cm line in PKS1814-63. The line profile is detected at a systematic velocity of 19178 kms^{-1}. The x-axis represents the velocity in kms^{-1} and the y-axis represents the continuum subtracted flux (Jy). The spectral line is derived from the pixel corresponding to the source location. The rms in the line profile is 50mJy

profile is relatively narrow, with the equivalent line width of $W_{20} = 75.9$ kms^{-1}. The equivalent line width is obtained by considering the rectangular width between the continuum and the background with the same area as the line. The high peak optical depth (τ_{obs}) and the HI column density were derived using

$$\tau_{obs} = -\ln[1 - \Delta S/S_{peak}] \tag{5.3}$$

where ΔS is the depth of the absorption line and S_{peak} is the peak brightness of the underlying radio continuum ($S_{peak} = 12.97$ Jy/beam). An optical depth of 0.21 (21%)

was derived. subsequently, the HI column density (N_{HI}) is given by,

$$N_{HI} = 1.83 \times 10^{18} \frac{T_s}{f} \int \tau_{obs}\, dv \tag{5.4}$$

where T_s is the spin temperature, estimated to be 100 K [6] and dv is the velocity line width. To derive the integrated optical depth $\int \tau_{obs} dv$,

$$\int \tau_{obs} dv = \int (1 - \text{continuum subtracted flux})\, dv \tag{5.5}$$

The advantage of using the integrated optical depth to derive the HI column density is that the integrated observables are independent of spectral resolution and therefore no information is lost when deriving the HI column density. The integrated optical depth, obtained using a in-house python code was 14.2 kms^{-1}. Assuming the covering factor of 1, the HI column density of 2.59 $\times 10^{21}$ cm^{-2} was calculated. The derived parameters for PKS1814-63 using KAT-7 are consistent with the parameters of the source obtained using the ATCA telescope, see Table 5.1 for the comparison of the results with the literature.

To determine the root mean square (rms) noise in the final images, the CASA task *imstat* was used. The task *imstat* displays statistical information from the image or selected region. The rms was determined by selecting a region outside the source and determining the noise level in that region. The selected region was set as input parameter in *imstat*. The values of the continuum rms and spectral rms derived from the final images were 2 mJy/beam and 50 mJy/beam respectively. The spectral dynamic range was calculated using the formulae;

$$\text{Spectral dynamic range} = \frac{\text{peak continuum flux (Jy/beam)}}{\text{rms of continuum subtracted cube (Jy/beam)}} \tag{5.6}$$

Using the peak continuum flux of 12.97 Jy/beam and the rms of the continuum subtracted cube 0.050Jy/beam, the spectral dynamic range of 259 (24 dB) was derived.

Table 5.1: PKS1814-63 parameters derived from the HI absorption line profile using observations from ATCA and KAT-7.

Observation	S(Jy)	Δ S(Jy)	τ_{obs}	W(kms^{-1})	N$_{HI}$cm^2	rms(Jy/beam)
KAT-7	13.03	2.53	0.21	75.9	2.5$\times 10^{21}$	0.050
ATCA	13.50	2.28	0.21	75.0	2.0$\times 10^{21}$	0.005

column 1 represents the telescope used for the observations, column 2 gives the flux density derived from the images, column 3 shows the depth of the absorption feature, the optical depth is shown in column 4, column 5 is the line width, column 6 and 7 gives the column density and spectral rms values respectively.

5.4 PKS1717-00

Some of the parameters derived for PKS1717-00 are obtained using the same procedure as stated in section 5.3. This means that we will refer to section 5.3 and only explain in details sections where the analysis procedure was different between the two sources. Using the CASA task *imfit*, the integrated flux density, S of 58.5 Jy $\pm$ 0.11 Jy and the peak brightness, S_{peak} of 41.8 Jy/beam $\pm$ 0.0083 Jy/beam were derived from the continuum image shown in Figure 5.12. The values of the flux density and peak bright-

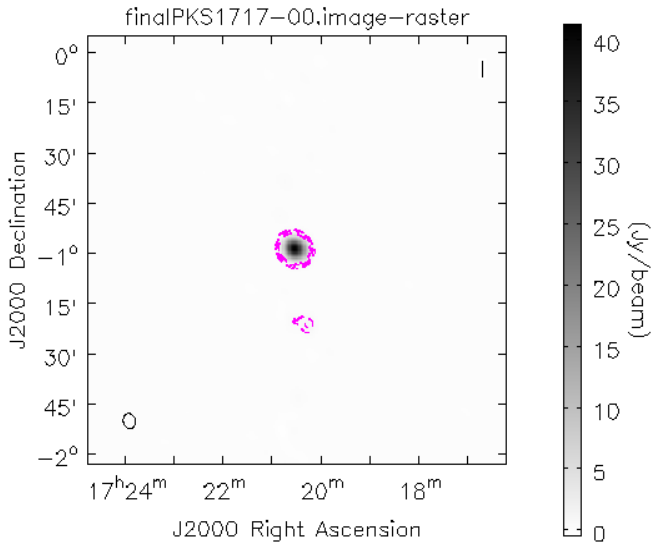

Figure 5.12: KAT-7 1378 MHz radio image of PKS1717-00. The image has a peak brightness of 41.8 Jy/beam $\pm$ 0.0083 Jy/beam with integrated flux density of 58.5 Jy $\pm$ 0.11 Jy. The off source noise level in the image is 20 mJy/beam. The contours are drawn at [-3,3,6,12,20,24] $\times$ 20 mJy/beam. The synthesized beam is 275.6″$\times$ 220.3″ at a position of 14.2° as shown in the left bottom ellipse.

ness derived from the continuum shows that the source is resolved at KAT-7 angular resolutions. In order to compare the derived flux density of the source with the expected flux density at the observing frequency 1378 MHz, the following equation was used

$$S_2 = S_1(\frac{\nu_2}{\nu_1})^{\alpha} \tag{5.7}$$

where S_2 is the expected flux density of PKS1717-00 at 1378 MHz (ν_2). S_1 and α is the flux density and spectral index of the source at frequency ν_1. At 2700 MHz, the flux density of PKS1717-00 is 36.3 Jy and has the spectral index of -0.78 [11]. Substituting

these values in Equation 5.7 gives the flux density of PKS1717-00 at 1378 MHz to be 61.3 Jy. The difference between the derived flux density and the expected flux density of PKS1717-00 is

$$\% = |S_{\text{measured}} - S_{\text{expected}}|/S_{\text{expected}} \tag{5.8}$$

which gives the % difference of 4.5.

Using the continuum subtracted spectral line cube, the spectral line obtained across the core at the pixel corresponding to the source location did not reveal any HI 21-cm absorption line. The spectral line obtained is shown in Figure 5.13. The spectrum is smoothed to 30kms^{-1}. The value of 30kms^{-1} was chosen by having information of the width of the expected absorption line in order to avoid smearing of the spectrum. The peak to peak variations in the spectrum is almost 100 mJy, making it impossible to detect an expected line with line depth 10 mJy. HI absorption was previously detected

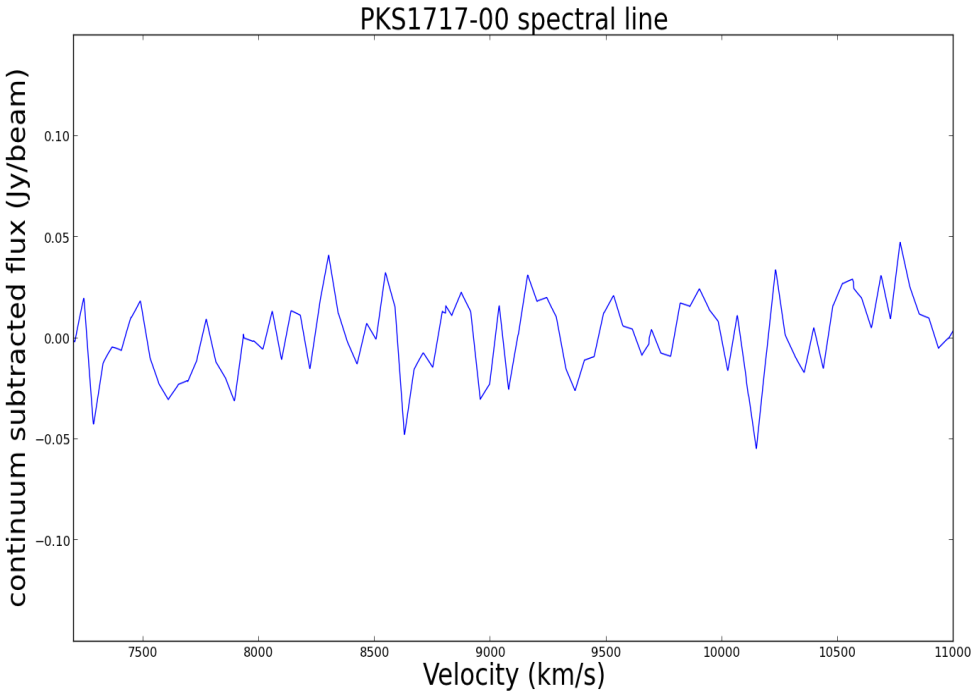

Figure 5.13: Spectrum for PKS1717-00 with no detectable 21-cm HI absorption. The y-axis represents the continuum subtracted flux (Jy) while the x-axis represents the velocity in kms^{-1}. The rms per channels was 21 mJy/beam. This is not sufficient to detect a line of magnitude 10 mJy. The spectrum is smoothed to 30kms^{-1}. The fitted restoration beam was 241.4 × 202.8 arc sec at position -40.5 degrees.

in this source at a position towards the radio core (Morganti et al. 2011)using data obtained with the Very Large Array (VLA) telescope. The detected absorption profile was reported to be broad and shallow with a depth of ΔS = 10 mJy and equivalent line width W_{20} = 300 kms^{-1}. The absorption profile was detected at a systematic velocity

of 9120 kms^{-1} with high HI column density of 4.2 $\times 10^{19}$ kms^{-1}

For non detection of the HI absorption line in PKS1717-00, we assume a gaussian absorption profile and derive the upper optical depth limit using 3σ (were σ represents the measured mean root square) in the image. This value is then used to estimate the upper HI column density limit. The upper optical depth limit $\tau_{3\sigma}$ was derived using

$$\tau_{3\sigma} = -\ln(1 - 3\Delta F/F_p) \tag{5.9}$$

where ΔF is the measured spectral rms and F_p represents the peak continuum flux. However, since the HI 21-cm absorption line in PKS1717-00 has been reported as being detected at the core, F_p represents the peak core flux. Using the measured rms value derived from the spectral line (21 mJy), and the peak core flux of 0.094 Jy obtained from (Morganti et al. 2011), the optical depth limit of $\tau_{3\sigma} = 0.38$ was derived. Subsequently, the HI column density was derived using,

$$N_{HI} = 1.83 \times 10^{18} \frac{T_{spin}}{f} \int \tau_{3\sigma} dv \tag{5.10}$$

To calculate the upper limit HI column density, we assume T_{spin} = 100K, covering factor $f = 1$, and the line width of $dv = 100 kms^{-1}$. The spin temperature, covering factor, and the line width were estimated considering values that are most common within known 21-cm absorbing sources. The value of 7$\times 10^{21}$ cm^{-2} was derived for the upper limit HI column density. The higher column density limit is consistent with the non detection in our spectrum.

Using the CASA task *imstat*, the channel rms was found to be 21 mJy/beam while the continuum rms was 12 mJy/beam. The channel rms was obtained from the spectral cube imaged with velocity resolution of 30kms^{-1}. The spectral dynamic range was derived using Equation 5.6. Given the peak flux of 41.8 Jy/beam with the spectral rms of 0.021 Jy/beam, the spectral dynamic range of 1990 (32 dB) was achieved. The expected spectral rms value for PKS1717-00 was 1.3 mJy. This value was obtained using Equation 3.7 given the channel bandwidth of 0.183 MHz (obtained after smoothing the spectrum to 30kms^{-1}), 7 working antennas, approximate dish diameter of 113.09 m^2, and the system temperature of 30.0 K. The spectral rms value obtained from the spectral cube is much larger compared to the expected spectral rms in the cube.

Table 5.2: Summary of the parameters derived from the observations. From left, the first column gives the source name, the second column is the measured flux density, the third column gives the peak brightness measured from the continuum, the expected flux density is given in column 4, column 5 gives the optical depth observed as well as the optical depth upper limit, column 6 and 7 gives the rms expected for continuum and spectral line respectively, column 8 and 9 has the rms for measured for both continuum and spectral line. column 10 gives the HI column density and the upper limit HI column density and finally the spectral dynamic range is given in column 11. The lower case e represents expected values and lowercase m represents the measured values. The continuum and spectral values are represented by *cont* and *spec* respectively.

Source	S_m(Jy)	S_{peak}(Jy)	S_e(Jy)	$\tau_{obs}/\tau_{3\sigma}$	$rms_{cont\ e}(Jy)$	$rms_{spec\ e}$(Jy)	$rms_{m\ cont}$(Jy)	$rms_{m\ spec}$(Jy)	$N_{HI}/N_{HI(3\sigma}cm^{-2}$)	SDR(dB)
PKS1717-00	58.50	41.80	61.3	0.38	0.0001	0.001	0.020	0.021	7.0×10^{21}	36
PKS1814-63	13.03	12.97	13.4	0.21	0.0005	0.032	0.002	0.050	2.5×10^{21}	24

5.5 On going work

In this section, we want to investigate some of the factors which could have lead to the high rms values in PKS1717-00. All the sources selected for this study are known to be strong isolated sources, therefore we expect to have constant visibilities as a function of frequency if delay tracking is on as shown in Figure 5.14. However, for some scans, ripples were observed in the visibilities of PKS1717-00 as shown in Figure 5.15. These may have affected the bandpass stability which may be the reason for the elevated noise levels.

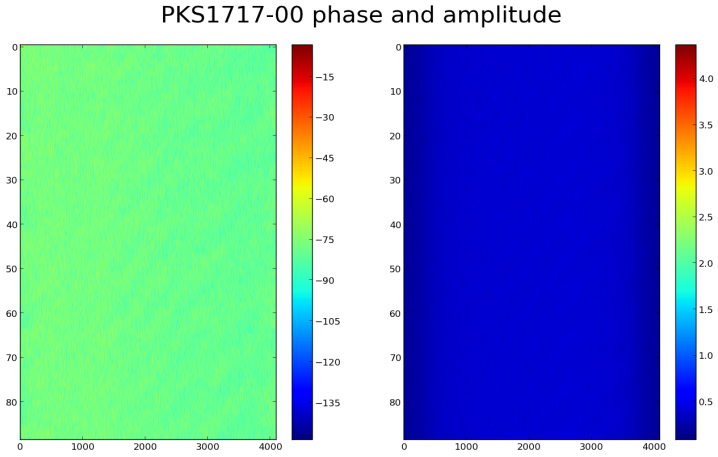

Figure 5.14: Waterfall plots showing phase (left) and amplitude (right) for PKS1717-00, scan 6. As seen in the Figure 6.1 both the phase and amplitudes are not affected by ripples.

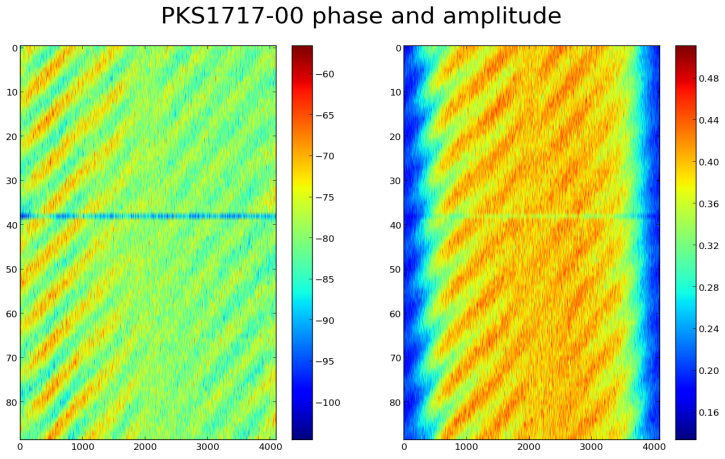

Figure 5.15: Waterfall plots of PKS1717-00 showing phase(left) and amplitude(right) for scan 20. Both the phase and amplitudes are seen to be affected by ripples. There is also a dropout for the single integration across the entire band on the amplitudes.

To further investigate this, we select a set of 3 flux calibrators from Perley-Taylor as bandpass calibrators and examine their bandpass shapes. The selected sources have a well characterized spectra that are known to be stable over a period of time. The observation where taken at different azimuth, elevation and time. Each bandpass calibrator was observed with 10 minutes duration per scan using KAT-7 25 MHz observing mode. Table 5.3 gives a summary of the observation times for the bandpass calibrators.

Table 5.3: Observation times of the bandpass calibrators.

File list	Date	Duration	Mode	Sources
1403523065.ms	23-06-2014	02:35:03	c16n25M4k	3C138/1934- 638/3C286
1403663209.ms	25-06-2014	05:58:17	c16n25M4k	3C138/1934- 638/3C286
1404271700.ms	02-07-2014	03:57:54	c16n25M4k	3C138/1934- 638/3C286
1404685242.ms	06-07-2014	11:30:02	c16n425Mk	3C138/1934- 638/3C286

Reduction The bandpass calibration was carried out to correct for the amplitude and phase as a function of frequency. Firstly, an initial phase calibration was applied over a small channel range, in this case we choose (1200 to 1500). This channel range was chosen after inspection of the data as it shows only small variations in the bandpass. The bandpass solutions were obtained using the task *bandpass*.

Results To check for the bandpass shapes in 3 bandpass calibrators, firstly, the bandpass solutions were presented in terms of amplitude/phase as a function of frequency. For each antenna, solutions per scan were produced. Figure 5.16 shows the bandpass solutions obtained for PKS1934-63 observed on 23-06-2014. Solutions for antenna 7 are given showing the 2 scans (scan 1 and scan 8). Colours in the bandpass solutions represent the different polarizations. Secondly, the raw data was presented in terms of waterfall plots of phase and amplitude for each source. Figure 5.17 shows the waterfall plots for 3C138 observed on 25-06-14. The plots were presented in terms of baselines per scan. The baselines are presented as square boxes identified with a number followed by a letter. The different letters represent different polarizations.

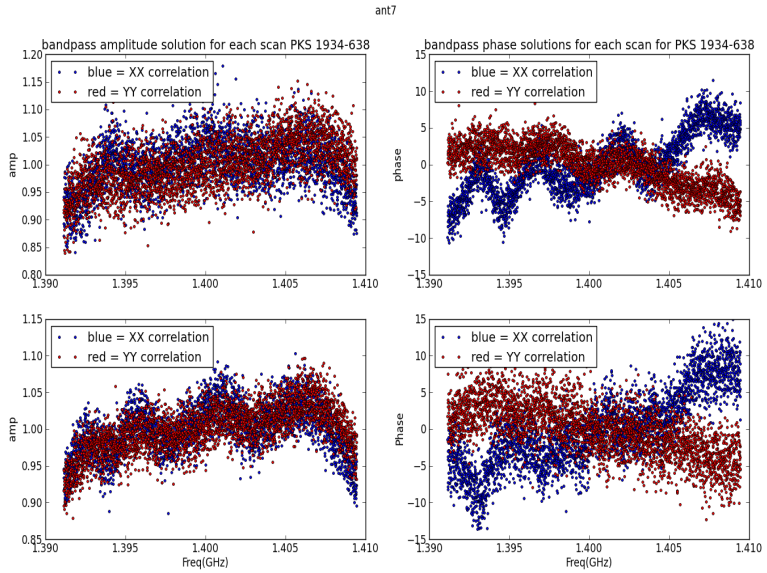

Figure 5.16: Bandpass solutions for PKS1934-63 observed on 23-06-2014. The plot represent solutions for antenna 7 and the different colours represent different polarizations. As seen from Figure 5.12, the presence of ripples are clearly seen in both scans. The top amplitude and phase represents bandpass solutions for scan 2 while the bottom amplitude and phase represents solutions for scan 8.

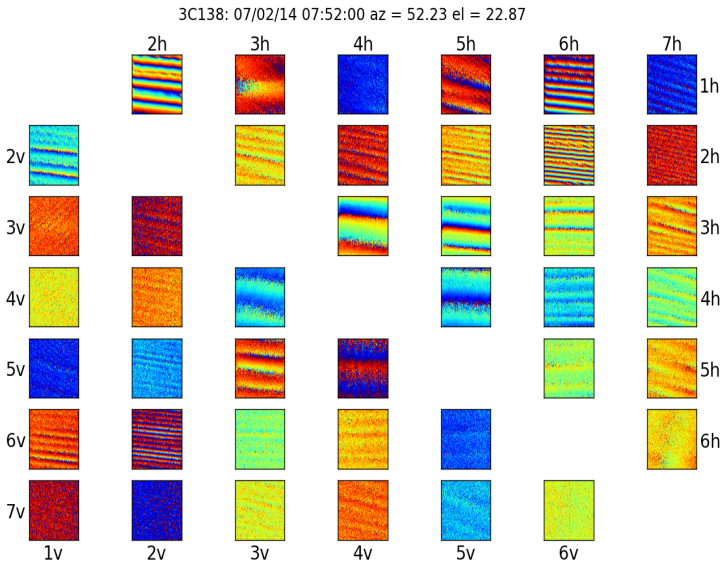

Figure 5.17: Waterfall plots showing the ripples in 3C138. The plot represents one scan with all baselines. The different letters represent different polarizations while the square boxes represent different different baselines.

as shown in Figure 5.16 and 5.17, ripples are observed in some scans. In the absence of ripples, we would expect the visibilities to be constant as a function of frequency. The observed ripples also differ in amplitudes and appearance which shows that there are different factors contributing to the observed ripple structures. We make two observations based on the results: firstly, certain ripples are only present when the Sun is up during observation period. Secondly, certain ripples are present regardless of the time of the day when the observation were taken. This suggests that there are two sources related to be observed ripples: solar interference and second stationary sources which produces RFI at all time. To identify the source of ripples in the bandpass calibrators, we plot the observed ripples for different scans together with the calculated solar or stationary ripples. The calculated ripples are plotted as contours on top of the observed ripples. For the observed ripples to correspond the the calculated ripples, the phase variations between the two are expected to show the same behavior as a function of frequency and time. In Figure 5.18 we show an example of the observed ripples which are consistent with the predicted solar ripples. The slope of the observed and predicted solar ripples show the same trend in both time and frequency. Next, Figure

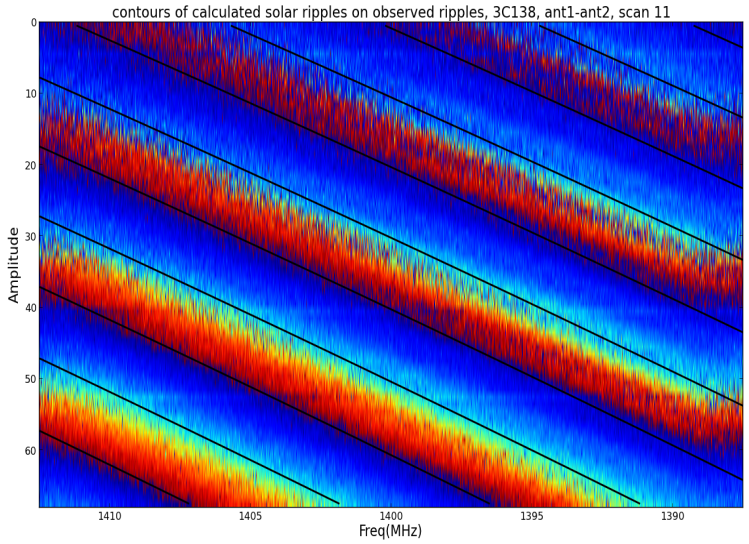

Figure 5.18: A plot of observed ripples and calculated solar ripples for 3C138, baseline antenna 1 and antenna 2, scan 11. The calculated ripples are plotted as contours on the observed ripples. The observed and calculated ripples compare favourably.

5.19 represents an example of the observed ripples which correspond to the predicted stationary ripples. The observations in this scan were taken at an elevation of 6°. This means that the observed stationary ripples could be associated with radiation coming from the ground (ground pickup).

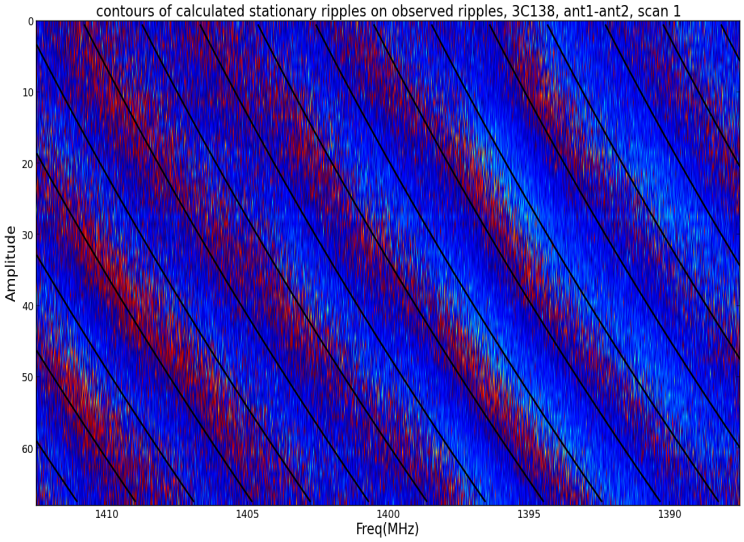

Figure 5.19: A plot of observed ripples and calculated stationary ripples for 3C138, baseline antenna 1 and antenna 2, scan 1. The calculated ripples are plotted as contours on the observed ripples. The observed ripples and calculated ripples compare favourably.

Interestingly, we also observe ripples which do not correspond to either solar or stationary ripples. In this case, the ripples could be associated to standing waves, where one antenna is pointing directly into the back of another. To illustrate this, the observed ripples in baseline antenna 1 and antenna 4, scan 9 were presented in two plots; one with the predicted solar contours and the other with the predicted stationary contours. In both cases, the phase variations as a function of time and frequency were different. The distance between antenna 1 and antenna 4 is $\sim$ 58.1 m, which is considerably short and the ripples could be associated to shadowing. Looking at the elevation and azimuth of the antenna in this scan; azimuth = -55° and elevation 19°, it is possible that the ripple structures could be due to antenna 1 picking up radiation from antenna 4.

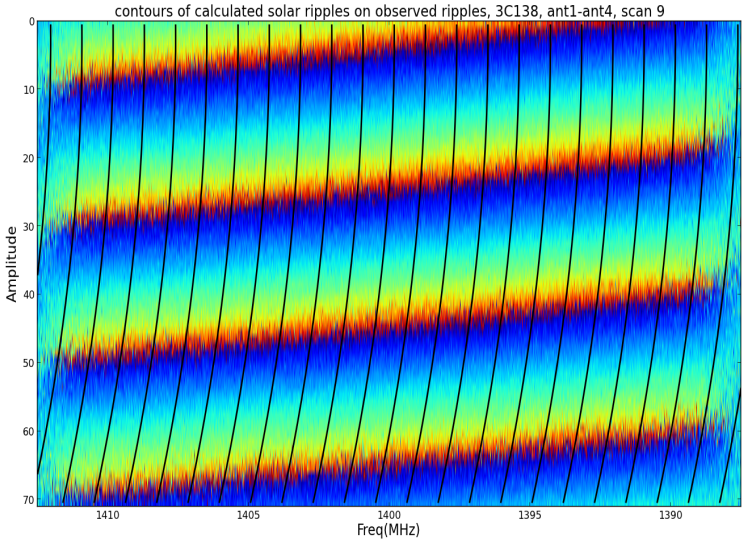

Figure 5.20: A plot of observed ripples and calculated solar ripples for 3C138, baseline antenna 1 and antenna 4, scan 9. The calculated ripples are plotted as contours on the observed ripples. The variation as a function of frequency between the calculated solar ripples and the observed ripples do not show any similarity.

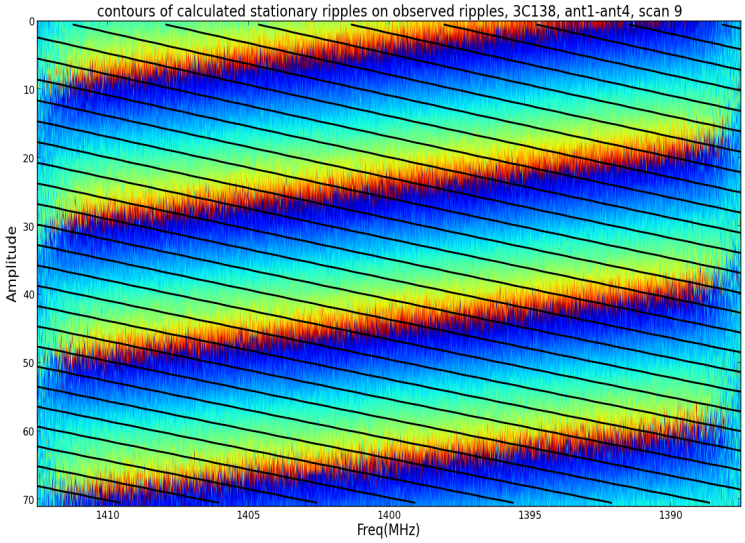

Figure 5.21: A plot of observed ripples and calculated stationary ripples for 3C138,baseline antenna 1 and antenna 4, scan 9. The calculated stationary ripples are plotted as contours on the observed ripples. The variation as a function of frequency between the calculated stationary ripples and the observed ripples do not show any similarity.

For the 3 bandpass calibrators observed using the 25 MHz observing mode, ripples have been identified. The ripples identified have been divided into two categories: ripples that appear at any time of the day and ripples that appear when the sun and source are both up during observations. The presence of ripples in the bandpass calibrators can affect the determination of spectral line features and therefore needs to be addressed. For example, during the calibration and analysis of PKS1717-00, the spectral line in Figure 5.22 was obtained before identifying the ripple structure in the bandpass calibrator PKS1934-638, see Figure 5.23. After identifying and removing the ripple structures, the spectrum in Figure 5.13 was obtained. This clearly shows that ripples could cause effects in the bandpass which could limit the detection of spectral lines. In this section we only covered ripples due to solar interference and ripples due to stationary objects. Other causes of ripples and further analysis on the effects of ripples on the bandpass stability will be addressed in the future work.

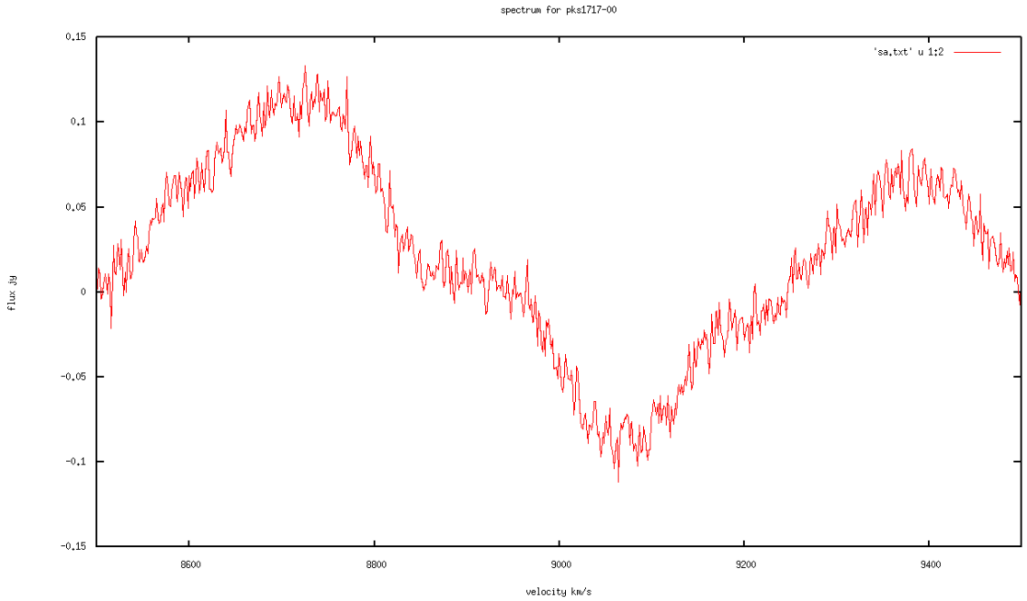

Figure 5.22: Spectral line for PKS1717-00 obtained from the spectral image before identifying the ripple structure in the bandpass. From the figure it shows that ripples can cause errors in the bandpass thereby limiting the detection of spectral features.

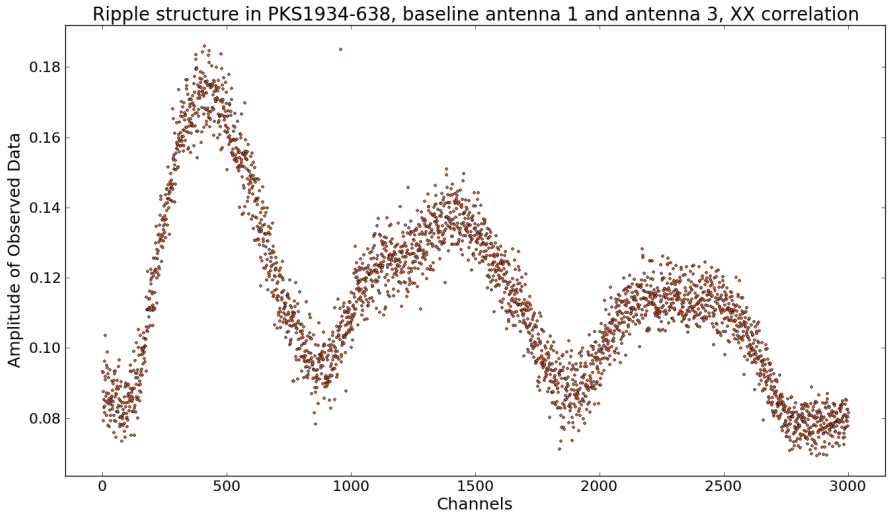

Figure 5.23: Ripple structure observed in the bandpass calibrator PKS1934-638 for the 12-13 May 2014 observations. The ripple structure is seen to have an effect on the bandpass shape as shown in Figure 5.22.

Chapter 6

Conclusion and future work

We have presented the results of the observations of 4 radio sources with KAT-7 within the redshift range 0.01-0.15 and at a velocity resolution of 1.2 kms^{-1} to investigate its capability of carrying out 21-cm absorption line searches using the 25 MHz observing mode. In all four cases, 21-cm absorption line associated with radio sources have been previously detected. The observations from PKS1318-43 and PKS1549-79 were excluded from the study sample due to the presence of solar and satellite interference respectively. Of the 2 remaining sources with sufficient data, 21-cm absorption line was detected in only one source. The 21-cm absorption line was detected in PKS1814-63 at a systematic velocity of 19178 kms^{-1} with a narrow line width of 75.9 kms^{-1}. High optical depth and column density were derived from the absorption profile. The parameters derived from the absorption line profile in PKS1814-63 using KAT-7 data are consistent with results obtained by Morganti et al. (2001) using data observed with ATCA. HI absorption line was not detected in PKS1717-00 due to poor signal derived from the final images. We derived the upper limit optical depth $\tau_{3\sigma}$ of 0.38 by using the core flux from Morganti et al. (2001) and the rms value from the spectral data cube smoothed to the resolution of 30kms^{-1}. Assuming the line width of 100 kms^{-1}, the upper limit HI column density was estimated to be 7 $\times 10^{21}\text{cm}^{-2}$. The higher column density limit is consistent with the non detection in our spectrum.

The derived rms in the images was higher than expected. This affected the spectral dynamic range derived from the observations. Ripples identified in the spectrum of PKS1717-00 could have led to the increased rms (poor signal to noise) thereby limiting the detection of the expected weak absorption line. It was found that interference seemed worse during the day than in the night, indicating that the source of the interference was likely to be solar. Our first observations for PKS1717-00 carried out in November 2013 during the day were found to have severe solar interference. We re-observed the source during the night in May 2014 and the data quality significantly improved. It is therefore recommended to carry out HI observations during the night

to ensure best quality data.

The bandpass shapes studied on 3 bandpass calibrators observed using the 25 MHz observing mode show the presence of ripples in some baselines. The ripples can be separated into two categories: those which appear at any time of the day and ripples that appear when the sun and the target source are both up during observations. Using simulations we were able to confirm the presence of ripples due to solar interference, stationary objects and shadowing.

From this study, the capability of detecting 21 cm absorption using KAT-7 has been verified. The results serve as a forerunner for the larger systematic absorption line study to be carried out on KAT-7 and later MeerKAT. The successful detection of HI absorption in one of our sources is an important first step towards utilizing the KAT-7 25 MHz observing mode for future large absorption line studies. However, the absence of the detection of HI in PKS1717-00 suggests that improvements such as the effects of ripples on the bandpass will need to be made in order to detect such weak spectral features.

Bibliography

Bridle, A. H. and Williamson, C. E. (1989). VLA Imaging of Large Scale Radio Filaments in 3C353. In *Bulletin of the American Astronomical Society*, volume 21 of *Bulletin of the American Astronomical Society*, page 1093.

De Robertis, M. (1999). Book Review: An Introduction to Active Galactic Nuclei / Cambridge U Press, 1997. JRASC, 93:100–100.

Ekers, J. A. (1969). The Parkes catalogue of radio sources, declination zone +20 to -90 . *Australian Journal of Physics Astrophysical Supplement*, 7:3–75.

Emonts, B. H. C., Morganti, R., Struve, C., Oosterloo, T. A., van Moorsel, G., Tadhunter, C. N., van der Hulst, J. M., Brogt, E., Holt, J., and Mirabal, N. (2010). Large-scale HI in nearby radio galaxies - II. The nature of classical low-power radio sources. MNRAS, 406:987–1006.

Fanaroff, B. L. and Riley, J. M. (1974). The morphology of extragalactic radio sources of high and low luminosity. MNRAS, 167:31P–36P.

Feng, S.-W., Shen, Z.-Q., Cai, H.-B., Chen, X., Lu, R.-S., and Huang, L. (2006). Multi-frequency VLBI observations of NRAO 530. A&A, 456:97–104.

Field, G. B. (1958). Excitation of the Hydrogen 21-CM Line. *Proceedings of the IRE*, 46:240–250.

Fomalont, E. B., Frey, S., Paragi, Z., Gurvits, L. I., Scott, W. K., Taylor, A. R., Edwards, P. G., and Hirabayashi, H. (2000). The VSOP 5 GHz Continuum Survey: The Prelaunch VLBA Observations. ApJS, 131:95–183.

Fomalont, E. B. and Perley, R. A. (1999). Calibration and Editing. In Taylor, G. B., Carilli, C. L., and Perley, R. A., editors, *Synthesis Imaging in Radio Astronomy II*, volume 180 of *Astronomical Society of the Pacific Conference Series*, page 79.

Gupta, N., Salter, C. J., Saikia, D. J., Ghosh, T., and Jeyakumar, S. (2006). Probing radio source environments via HI and OH absorption. MNRAS, 373:972–992.

Holt, J., Tadhunter, C. N., and Morganti, R. (2008). Fast outflows in compact radio sources: evidence for AGN-induced feedback in the early stages of radio source evolution. MNRAS, 387:639–659.

Kanekar, N. and Briggs, F. H. (2004). 21-cm absorption studies with the Square Kilometer Array. , 48:1259–1270.

Krawczynski, H. and Treister, E. (2013). Active galactic nuclei the physics of individual sources and the cosmic history of formation and evolution. *Frontiers of Physics*, 8:609–629.

Kulkarni, S. R. and Heiles, C. (1988). *Neutral hydrogen and the diffuse interstellar medium*, pages 95–153.

Lloyd, B. D., Jones, P. A., and Haynes, R. F. (1996). Observations of the radio jets in NGC 5090 (PKS B1318-434). MNRAS, 279:1197–1209.

Lovell, J. E. J. (1997). Southern radio gravitational lens survey and observations. (Thesis abstract). , 14:290–291.

Lucero, D. M., Carignan, C., Hess, K. M., Frank, B. S., Randriamampandry, T. H., Goedhart, S., and Passmoor, S. S. (2014). KAT-7 Science Verification: Using HI Observations of NGC 3109 to Understand its Kinematics and Mass Distribution. In *American Astronomical Society Meeting Abstracts #223*, volume 223 of *American Astronomical Society Meeting Abstracts*, page 138.06.

Marscher, A. P. and Broderick, J. J. (1981). X-ray and VLBI radio observations of the quasars NRAO 140 and NRAO 530. ApJ, 249:406–414.

Morganti, R., Holt, J., Tadhunter, C., Ramos Almeida, C., Dicken, D., Inskip, K., Oosterloo, T., and Tzioumis, T. (2011). PKS 1814-637: a powerful radio-loud AGN in a disk galaxy. A&A, 535:A97.

Morganti, R., Oosterloo, T. A., Emonts, B. H. C., van der Hulst, J. M., and Tadhunter, C. N. (2003). Fast Outflow of Neutral Hydrogen in the Radio Galaxy 3C 293. ApJ, 593:L69–L72.

Morganti, R., Oosterloo, T. A., Tadhunter, C. N., van Moorsel, G., Killeen, N., and Wills, K. A. (2001). Hi absorption in radio galaxies: effect of orientation or interstellar medium? MNRAS, 323:331–342.

Morganti, R., Tadhunter, C. N., and Oosterloo, T. A. (2005). Fast neutral outflows in powerful radio galaxies: a major source of feedback in massive galaxies. A&A, 444:L9–L13.

Netzer, H. (2013). *The Physics and Evolution of Active Galactic Nuclei.*

Osterbrock, D. E. (1981). Seyfert galaxies with weak broad H alpha emission lines. ApJ, 249:462–470.

Osterbrock, D. E., Tran, H. D., and Veilleux, S. (1992). Near-infrared spectra and classification diagnostics of Seyfert galaxies. ApJ, 389:196–207.

Preston, R. A., Jauncey, D. L., Meier, D. L., Tzioumis, A. K., Ables, J., Batchelor, R., Faulkner, J., Gates, J., Greene, B., Hamilton, P. A., Harvey, B. R., Haynes, R. F., Johnson, B., Lambeck, K., Louie, A. P., McCulloch, P., Moorey, G., Morabito, D. D., Nicolson, G. D., Niell, A. E., Robertson, J. G., Royle, G. R., Skjerve, L., Slade, M. A., Slee, O. B., Stolz, A., Watkinson, A., Wehrle, A. E., and Wright, A. E. (1989). The Southern Hemisphere VLBI experiment. AJ, 98:1–26.

Rees, M. J. (1984). Black Hole Models for Active Galactic Nuclei. ARA&A, 22:471–506.

Rohlfs, K. and Wilson, T. L. (2000). *Tools of radio astronomy.*

Rybicki, G. B. and Lightman, A. P. (1986). *Radiative Processes in Astrophysics.*

Saikia, D. J., Jeyakumar, S., Wiita, P. J., Sanghera, H. S., and Spencer, R. E. (1995). Compact steep-spectrum radio sources and unification schemes. MNRAS, 276:1215–1223.

Salpeter, E. E. (1964). Accretion of Interstellar Matter by Massive Objects. ApJ, 140:796–800.

Sault, R. J. (2003). ATCA flux density scale at 12mm. *Australia Telescope National Facility.*

Shields, G. A. (1999). A Brief History of AGN. *ArXiv Astrophysics e-prints.*

Tadhunter, C. (2008). An introduction to active galactic nuclei: Classification and unification. , 52:227–239.

Tadhunter, C., Wills, K., Morganti, R., Oosterloo, T., and Dickson, R. (2001). Emission-line outflows in PKS1549-79: the effects of the early stages of radio-source evolution? MNRAS, 327:227–232.

Tadhunter, C. N., Morganti, R., di Serego-Alighieri, S., Fosbury, R. A. E., and Danziger, I. J. (1993). Optical Spectroscopy of a Complete Sample of Southern 2-JY Radio Sources. MNRAS, 263:999.

Taylor, G. B., Carilli, C. L., and Perley, R. A., editors (1999). *Synthesis Imaging in Radio Astronomy II*, volume 180 of *Astronomical Society of the Pacific Conference Series.*

Thompson, A. R. (1989). The Interferometer in Practice. In Perley, R. A., Schwab, F. R., and Bridle, A. H., editors, *Synthesis Imaging in Radio Astronomy*, volume 6 of *Astronomical Society of the Pacific Conference Series*, page 11.

Tzioumis, A. K., Tingay, S. J., Stansby, B., Reynolds, J. E., Phillips, C. J., Amy, S. W., Edwards, P. G., Bowen, M. A., Leach, M. R., Kesteven, M. J., Chung, Y., Stevens, J., Forsyth, A. R., Gulyaev, S., Natusch, T., Macquart, J.-P., Reynolds, C., Wayth, R. B., Bignall, H. E., Hotan, A., Hotan, C., Godfrey, L., Ellingsen, S., Dickey, J., Blanchard, J., and Lovell, J. E. J. (2010). Evolution of the Parsec-scale Structure of PKS 1934-638 Revisited: First Science with the ASKAP and New Zealand Telescopes. AJ, 140:1506–1510.

Urry, C. M. and Padovani, P. (1995). Unified Schemes for Radio-Loud Active Galactic Nuclei. PASP, 107:803.

van Gorkom, J. H., Knapp, G. R., Ekers, R. D., Ekers, D. D., Laing, R. A., and Polk, K. S. (1989). H I absorption in radio elliptical galaxies - Evidence for infall. AJ, 97:708–719.

Vermeulen, R. C. (2004). The interplay between radio jets and atomic hydrogen gas seen in 21cm h i absorption. In *null*, volume 2004 of *Proceedings of the International Astronomical Union*, pages 439–442.

Veron-Cetty, M. P. and Veron, P. (1998). VizieR Online Data Catalog: Quasars and Active Galactic Nuclei (8th Ed.) (Veron+ 1998). *VizieR Online Data Catalog*, 7207:0.

Véron-Cetty, M.-P., Woltjer, L., Staveley-Smith, L., and Ekers, R. D. (2000). The nature of powerful compact radio galaxies. A&A, 362:426–434.

Walterbos, R. A. M. and Braun, R. (1996). The Cool and Warm Phases of the Interstellar Medium in Spiral Galaxies. In Skillman, E. D., editor, *The Minnesota Lectures on Extragalactic Neutral Hydrogen*, volume 106 of *Astronomical Society of the Pacific Conference Series*, page 1.

Weaver, K. A. (2000). Quasars and Active Galactic Nuclei: An Introduction, by Ajit K. Kambhavi and Jayant V. Narlikar. *Physics Today*, 53(5):60–61.

Wiita, P. J. (2006). Active Galactic Nuclei: Unification, Blazar Variability and the Radio Galaxy/Cosmology Interface. *ArXiv Astrophysics e-prints*.

Wilson, T. L., Rohlfs, K., and Hüttemeister, S. (2013). *Tools of Radio Astronomy*.

Wilson, W. E., Ferris, R. H., Axtens, P., Brown, A., Davis, E., Hampson, G., Leach, M., Roberts, P., Saunders, S., Koribalski, B. S., Caswell, J. L., Lenc, E., Stevens, J., Voronkov, M. A., Wieringa, M. H., Brooks, K., Edwards, P. G., Ekers, R. D., Emonts, B., Hindson, L., Johnston, S., Maddison, S. T., Mahony, E. K., Malu, S. S., Massardi, M., Mao, M. Y., McConnell, D., Norris, R. P., Schnitzeler, D., Subrahmanyan, R., Urquhart, J. S., Thompson, M. A., and Wark, R. M. (2011). The Australia Telescope Compact Array Broad-band Backend: description and first results. MNRAS, 416:832–856.

Wrobel, J. M. and Walker, R. C. (1999). Sensitivity. In Taylor, G. B., Carilli, C. L., and Perley, R. A., editors, *Synthesis Imaging in Radio Astronomy II*, volume 180 of *Astronomical Society of the Pacific Conference Series*, page 171.

Zhang, E.-P. and Wang, J.-M. (2006). The Unified Model of Active Galactic Nuclei. I. Non-Hidden Broad-Line Region Seyfert 2 and Narrow-Line Seyfert 1 Galaxies. ApJ, 653:137–151.